

From oxo-Functionalized Graphene to Porous Graphene and Graphene Quantum Dots

Inaugural-Dissertation
to obtain the academic degree
Doctor rerum naturalium (Dr. rer. nat.)

submitted to the Department of Biology, Chemistry, Pharmacy
of Freie Universität Berlin

by

Yalei Hu

July 2022

The work presented here was conducted from 10/2018 until 05/2022 at the Department of Biology, Chemistry, Pharmacy of the Freie Universität Berlin under the supervision of Prof. Dr. Siegfried Eigler.

1st Reviewer: Prof. Dr. Siegfried Eigler (Freie Universität Berlin)

2nd Reviewer: Prof. Dr. Rainer Haag (Freie Universität Berlin)

Disputation at: 21.10.2022

Table of Contents

1	Summary.....	1
2	Zusammenfassung	2
3	Introduction	4
	3.1 History of Graphene Materials.....	4
	3.2 Porous Graphene	7
	3.2.1 Properties of porous graphene.....	8
	3.2.2 Preparation of porous graphene	10
	3.3 Graphene Quantum Dots	13
	3.3.1 Properties of graphene quantum dots.....	14
	3.3.2 Solvent effects on optical properties	16
	3.4 Purpose and Significance of the Study.....	17
4	Characterization and Testing Techniques	19
	4.1 Morphological Characterization	19
	4.1.1 Atomic force microscopy	19
	4.1.2 Transmission electron microscopy.....	20
	4.2 Compositional and Structural Analysis	21
	4.2.1 Fourier-transform infrared spectroscopy	21
	4.2.2 Raman spectroscopy	23
	4.2.3 X-ray photoelectron spectroscopy.....	24
	4.2.4 Nuclear magnetic resonance spectroscopy	25
	4.2.5 CHNS elemental analysis	26
	4.3 Optical Property Characterization.....	27
	4.3.1 Ultraviolet/Visible absorption.....	27
	4.3.2 Fluorescence.....	28
	4.4 Langmuir-Blodgett Technique	30
5	Main Contributions	31
	5.1 Wet-Chemical Synthesis of Solution-Processible Porous Graphene <i>via</i> Defect-Driven Etching.....	31

5.2 Polarity, Intramolecular Charge Transfer, and Hydrogen Bond Co-Mediated Solvent Effects on the Optical Properties of Graphene Quantum Dots	50
6 Minor Contributions	65
6.1 Influence of SiO ₂ or h-BN Substrate on the Room Temperature Electronic Transport in Chemically Derived Single Layer Graphene	65
6.2 Synthesis of Wet-Chemically Prepared Porous-Graphene Single Layers on Si/SiO ₂ Substrate Increasing the Photoluminescence of MoS ₂ in Heterostructures.....	77
6.3 Interlayer Electron Modulation in van der Waals Heterostructures Assembled by Stacking Monolayer MoS ₂ onto Monolayer Graphene with Different Electron Transfer Ability	100
List of Abbreviations.....	115
List of Publications	118
References.....	119
Acknowledgements.....	124
Statement of the author	125

1 Summary

This cumulative dissertation is divided into two main topics: 1) preparation of porous graphene and revealing the mechanism of pore formation; 2) investigation of solvent effects on the optical properties of graphene quantum dots (GQDs). The research was conducted in collaboration with the groups of 1) Dr. Ute Resch-Genger from the Federal Institute for Materials Research and Testing; 2) Prof. Dr. Andrey Turchanin from the Institute of Physical Chemistry and Abbe Center of Photonics at Friedrich Schiller University Jena; 3) Prof. Dr. Ute Kaiser from the Central Facility of Electron Microscopy at Ulm University. The complete results and experimental details are included in the attached publications in section 5 and section 6.

1) Porous graphene via chemical etching by hydroxyl radicals

Porous graphene is a new class of graphene materials that has received favorable attention from researchers due to its unique properties, such as large specific surface area. However, current synthetic methods like laser lithography and catalyst activation have some problems, such as tedious operation or poor controllability. Therefore, a controlled wet chemical method for preparing porous graphene in large quantities is urgently needed. To achieve scalable preparation with easier manipulation, specific chemical etching would be one of the available choices. Here, a simple and controllable method is developed for producing solution-processable porous graphene derivatives. We identify oxo-functionalized graphene (oxo-G) with its regulated, low density of in-plane vacancy defects as a suitable precursor. Hydroxyl radicals are generated by the photolysis of hydrogen peroxide under ultraviolet (UV)-irradiation, which etch pores on the basal plane of oxo-G, initiating the pore formation preferentially at defect sites. Correspondingly, oxo-G flakes with lateral dimensions of μm -size and pores with tunable sizes between 5 nm and 500 nm are accessible. Based on results from atomic force microscopy (AFM), transmission electron microscopy (TEM), ultraviolet/visible (UV/Vis) spectroscopy, Fourier-transform infrared spectroscopy (FTIR), X-ray photoelectron spectroscopy (XPS), solid-state nuclear magnetic resonance (NMR) spectroscopy, and statistical Raman spectroscopy (SRS), a possible mechanism for pore formation is proposed. The electrophilic addition and oxidation reaction between hydroxyl radicals and oxo-G

close to defect sites is the basis for etching. The porous graphene materials can serve as membranes and provide ideas for the tunability of two-dimensional materials.

2) Solvent effects on the optical properties of GQDs

Due to their special optical features, GQDs have gained a growing amount of interest and have found widespread use, for instance, in the biomedical, chemical, and environmental fields as sensors and markers. However, the structure-related features of GQDs resulting in solvent-dependent optical properties are currently unclear. Using oxo-functionalized graphene and *p*-phenylenediamine as precursors, we synthesized long-wavelength emitting GQDs with a size of approximately 3.6 nm by a solvothermal approach. The structure and surface characteristics of as-synthesized GQDs were analyzed by TEM, AFM, FTIR, Raman, and XPS. Subsequently, the effect of solvent polarity and proticity on the optical characteristics of GQDs containing -OH, -NH₂, -COOH, and pyridine surface groups was studied. A plausible luminescence mechanism is presented based on the absorption and fluorescence (FL) results of GQDs. The observed alterations in FL with respect to the position of the maximum, quantum yield, and decay kinetics in protic and aprotic solvents, are attributed to polarity effects, intramolecular charge transfer processes, and hydrogen bonding. Additionally, the optical sensing potential of GQDs for trace amounts of water was evaluated. Our systematic spectroscopic analysis will facilitate the rational design of GQDs and provide more information on the fluorescence process of carbon-based fluorescent nanomaterials.

2 Zusammenfassung

Diese kumulative Dissertation gliedert sich in zwei Hauptteile: 1) Darstellung von porösem Graphen und Aufklärung des Mechanismus der Porenbildung; 2) Untersuchung der Auswirkungen von verschiedenen Lösungsmitteln auf die optischen Eigenschaften von Graphen-Quantenpunkten (GQDs). Die Experimente wurden teilweise in Zusammenarbeit mit den Gruppen von 1) Dr. Ute Resch-Genger von der Bundesanstalt für Materialforschung und -prüfung, 2) Prof. Dr. Andrey Turchanin vom Institut für Physikalische Chemie und Abbe Center of Photonics der Friedrich-Schiller-Universität Jena und 3) Prof. Dr. Ute Kaiser von der Zentrale Einrichtung Elektronenmikroskopie der Universität Ulm durchgeführt. Die vollständigen

Ergebnisse und experimentellen Details sind in den beigefügten Veröffentlichungen in Abschnitt 5 und Abschnitt 6 enthalten.

1) Poröses Graphen durch chemisches Ätzen mit Hydroxylradikalen

Poröses Graphen stellt eine neue Klasse innerhalb der Graphen-basierten Materialien dar, welche aufgrund ihrer einzigartigen Eigenschaften wie beispielweise einer großen spezifischen Oberfläche, vermehrt auf wissenschaftliches Interesse stoßen. Etablierte synthetische Methoden wie Laser-Lithographie und Katalysatoraktivierung zeigen jedoch einige Schwächen, wie langwierige Operation und schlechte Kontrollierbarkeit. Das chemische Ätzen von Poren in intaktes Graphen ist hier eine vielversprechende Möglichkeit, welche sich unter anderem durch leichte Manipulation und Skalierbarkeit auszeichnet. In dieser Arbeit wird ein einfaches und kontrollierbares Verfahren zur Herstellung von porösen Graphenderivaten in Lösung entwickelt. Als geeignetes Ausgangsmaterial wird oxo-funktionalisiertes Graphen (oxo-G) mit seiner regulierten, geringen Dichte an Defekten in der Ebene ausgewählt. Durch die katalytische Photolyse von Wasserstoffperoxid unter UV-Bestrahlung werden Hydroxylradikale erzeugt, die Poren in der Basalebene von oxo-G ätzen und die Porenbildung bevorzugt an Defektstellen initiieren. Auf diese Weise sind oxo-G-Flocken mit lateralen Abmessungen von mm-Größe und Poren mit kontrolliert variierbaren Größen zwischen 5 nm und 500 nm zugänglich. Auf der Grundlage von Ergebnissen der Rasterkraftmikroskopie (AFM), der Transmissionselektronenmikroskopie (TEM), der UV/Vis-Spektroskopie, der Fourier-Transformations-Infrarotspektroskopie (FTIR), der Röntgen-Photoelektronenspektroskopie (XPS), der Festkörper Kernresonanzspektroskopie (NMR) und der statistischen Raman-Spektroskopie (SRS) wird ein möglicher Mechanismus der Porenbildung vorgeschlagen. Die elektrophile Additions- und Oxidationsreaktion zwischen Hydroxylradikalen und oxo-G in der Nähe von Defektstellen ist die Grundlage für das Ätzen der Poren. Die porösen Graphen-Materialien könnten zukünftig beispielsweise als Membranen zum Einsatz kommen. Ihr Herstellungs- und Anlyaseprozess bietet auch generell Ansatzpunkte zur Optimierung zweidimensionaler Materialien.

2) Auswirkungen von verschiedenen Lösungsmitteln auf die optischen Eigenschaften von GQDs

Aufgrund ihrer besonderen optischen Eigenschaften stoßen GQDs auf wachsendes Interesse und werden beispielsweise in der Biomedizin, der Chemie und im Umweltbereich als Sensoren und Marker eingesetzt. Jedoch sind die strukturbezogenen Merkmale von GQDs, die zu lösungsmittelabhängigen optischen Eigenschaften führen, derzeit noch unklar. Unter Verwendung von oxofunktionalisiertem Graphen und *p*-Phenylendiamin als Startmaterial wurden langwellig-emittierende GQDs mit einer Größe von etwa 3,6 nm durch eine solvothermische Methode synthetisiert. Die Struktur und die Oberflächeneigenschaften der synthetisierten GQDs wurden mittels TEM, AFM, FTIR, Raman und XPS analysiert. Anschließend wurde die Auswirkung der Polarität und Protizität des Lösungsmittels auf die optischen Eigenschaften von GQDs mit -OH-, -NH₂-, -COOH- und Pyridin-Oberflächengruppen untersucht. Auf der Grundlage der Ergebnisse der Absorptionen und Fluoreszenz (FL) der GQDs wird ein plausibler Lumineszenzmechanismus vorgestellt. Die beobachteten Veränderungen der FL in Bezug auf die Position des Maximums, die Quantenausbeute und die Abklingkinetik in protischen und aprotischen Lösungsmitteln werden auf Polaritätseffekte, intramolekulare Ladungstransferprozesse und Wasserstoffbrückenbindungen zurückgeführt. Darüber hinaus wurde das optische Erfassungspotenzial von GQDs für Spuren von Wasser untersucht. Die hier vorgestellte systematische Analyse wird das rationale Design von GQDs erleichtern und weitere Informationen über den Fluoreszenzprozess von fluoreszierenden Nanomaterialien auf Kohlenstoffbasis liefern.

3 Introduction

3.1 History of Graphene Materials

Carbon is the fourth most abundant element in the universe after hydrogen, helium, and oxygen. On Earth, its abundance in the crust is only exceeded by iron, silicon, and titanium. Carbon atoms' capacity to create powerful covalent bonds with other carbon atoms in different hybridization states (sp, sp², and sp³) or with nonmetallic elements enables them to build a wide variety of structures, from small molecules to

macromolecular chains.^[1] This feature demonstrates the great significance of organic chemistry and biochemistry to living organisms as a highly dynamic structural backbone. Two centuries ago, carbon was first proved to be present in all organic molecules, like proteins and carbohydrates, else inorganic molecules like graphite, diamond, *etc.* Graphite is one part of carbon matter, and it is a soft, opaque, black substance with exceptional electrical conductivity. In addition, graphite consists of layers of graphene that are layered and held together through van der Waals interactions.

International Union of Pure and Applied Chemistry (IUPAC) defines graphene as “a single carbon layer of graphite structure, explaining its nature by analogy to a polycyclic aromatic hydrocarbon of essentially limitless size.”^[2] However, this concept has rarely been used accurately in the literature recently. The word graphene has been used informally in the scientific literature to refer to graphene in its purest form and numerous other materials with comparable properties, all of which we classify better as graphene-based materials. These materials can differ from the IUPAC definition of graphene in many ways: 1) the number of layers of some so-called graphene is sometimes more than one;^[3] 2) chemically processed graphene materials commonly contain a large number of heteroatoms, such as oxygen-containing groups;^[4] and 3) some so-called graphene sheets have a large number of sp^3 -hybridized carbon defects and holes/pores on the basal plane.^[5]

Graphene has become a research hotspot since Geim and Novoselov won the Nobel Prize in Physics in 2010 “*for groundbreaking experiments regarding the two-dimensional material graphene.*”^[6] Two-dimensional materials have attracted growing attention due to their remarkable properties, like high strength, carrier mobility, and thermal conductivity compared to the existing materials.^[7] However, the study of graphene-related materials has a long and rich history (>180 years).^[8] As shown in **Figure 3.1**, there are several pivotal moments/periods in the history of graphene materials, including the discovery/preparation of graphite intercalation compounds, graphite oxide, graphene oxide (GO), porous graphene, graphene quantum dots (GQDs), and oxo-functionalized graphene (oxo-G). The story starts in 1840 when Schafhaeutl first described the preparation of graphite intercalation compounds.^[8-9] In 1855, Brodie first reported the formation of graphite oxide in a short note and showed more details for the synthetic information in 1859. In that paper, he tried to use $KClO_3$,

sulfuric acid, and nitric acid as oxidants to react with graphite, which is known as “Brodie’s method” now.^[10] Over the next century, several groups tried to synthesize graphite oxide by following or improving the Brodie method and further characterize it. For instance, in 1865, Gottschalk synthesized graphite oxide using Brodie’s method and named it “Graphitsäure” (graphitic acid).^[11] In 1898, Staudenmaier reviewed the existing techniques and proposed a less dangerous strategy for synthesizing graphite oxide.^[12] In 1928 and the subsequent years, Hofmann and co-workers investigated the structure of graphite oxide and gave the first structural model of graphite oxide.^[13] In 1958, Hummers and co-workers ushered in a new era of graphene materials research by providing a safer and more effective approach for preparing graphite oxide using permanganate as an oxidant in sulfuric acid, known as “Hummers’ method,” and has been widely used in recent decades.^[14] Later, Boehm *et al.* prepared thin, lamellar carbon sheets four years later by chemically reducing the graphite oxide dispersion.^[15] In addition, Boehm *et al.* also coined the term graphene in 1986, deriving it from the combination of the word graphite and the suffix referring to polycyclic aromatic hydrocarbons.^[16] More than a decade later, groundbreaking experiments were carried out by Geim and Novoselov in 2004, where monolayer graphene was obtained using mechanical exfoliation.^[6a] They found that the monolayer graphene film exhibited high room-temperature mobility ($\sim 10,000 \text{ cm}^2/\text{V}\cdot\text{s}$). This work was awarded the 2010 Nobel Prize in Physics and led to numerous fascinating investigations of graphene and other two-dimensional materials. Since the isolation of graphene, its properties and applications have been intensively investigated and exploited. However, researchers have found some limits when treating graphene in specific cases, like its zero bandgap for semiconductor devices, stacking behavior in graphene-reinforced composite formation, *etc.* To overcome the drawbacks, structural modification of graphene was subsequently explored, leading to bandgap opening or activation of the carbon lattice. One possible way to open bandgap is by introducing lattice defects; as shown by Fischbein and Drndić in 2008, graphene was sculpted with nanometer-scale pores, slits, and gaps.^[17] In the same year, Ponomarenko and Geim fabricated graphene quantum dots (GQDs).^[18] The GQDs have several innovative qualities, such as distinctive photoluminescence due to their quantum confinement effect. In addition, Eigler proposed oxo-G, which has oxo-functionalities on the basal plane of graphene and a nearly intact hexagonal carbon framework in contrast to graphene oxide bearing a higher density of disorder traditionally in its carbon lattice.^[19] Low-temperature-

controlled oxidation of graphite is employed to produce oxo-G, which prevents the formation of extensive structural defects compared with Hummers' method. Thus, the low-temperature procedure minimizes carbon loss as CO₂. In another way, overoxidation is suppressed in terms of oxo-G and its derivatives. Furthermore, the defect density can be more precisely quantified, altered, and visualized for oxo-G and its derivatives, making them an ideal precursor for manufacturing surface-functionalized graphene materials.

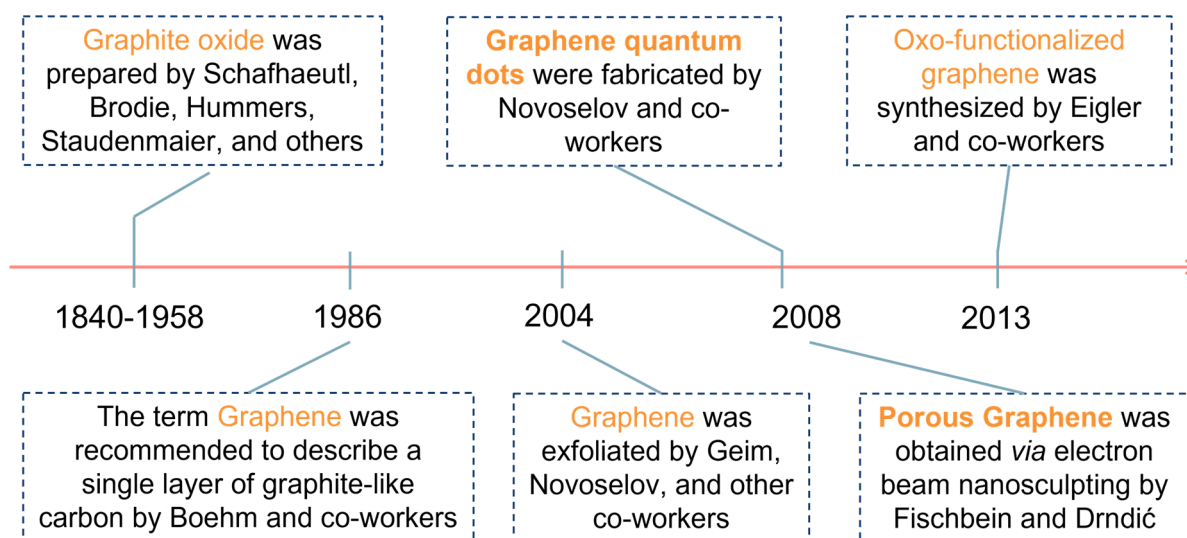


Figure 3.1 History of graphene materials.

3.2 Porous Graphene

Porous graphene, also known as holey graphene, is a form of graphene with pores in the plane.^[20] Compared with other porous carbon materials, porous graphene has several significant features.^[21] First, the high mechanical strength of graphene can promote the stability of porous frameworks and prevent the structures from shrinking or collapsing.^[22] Second, the pores in porous graphene are conducive to the rapid diffusion of electrolytes, which makes porous graphene a perfect current collector for the rapid transit of charge carriers inside the frameworks.^[23] Third, some porous graphene is created from GO or oxo-G containing oxygen functional groups, making them attractive platforms for further functionalization, enabling the development of graphene-based porous structures.^[24] These unique characteristics allow porous graphene to serve as an essential component in many fields, including energy storage and conversion devices. **Figure 3.2** shows the annual histogram of publication items of porous/holey graphene with a rapid increase since 2008.

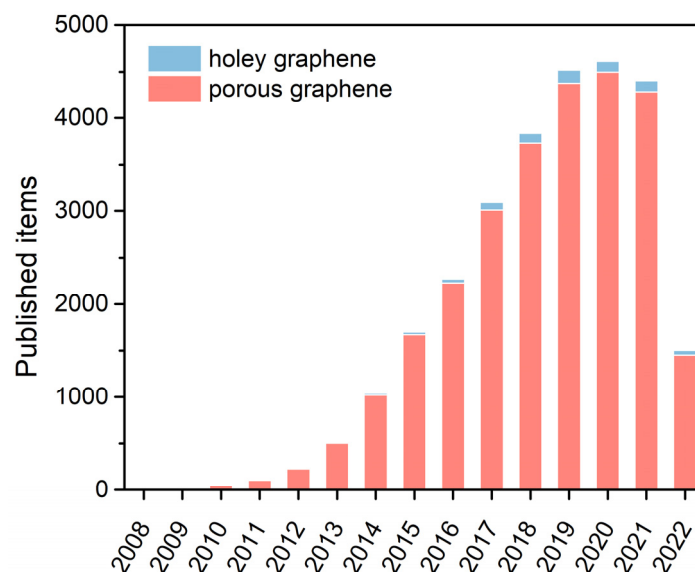


Figure 3.2 Publications item on topic of 'porous graphene' and 'holey graphene' since 2008; search results obtained by Web of Science, May 2022.

3.2.1 Properties of porous graphene

Structure properties: Porous graphene is a modified graphene sheet in which the lack of carbon atoms in the plane results in the formation of some pores/holes.^[25] The structure of porous graphene differs in terms of pore size and distribution based on the fabrication method. For example, as shown in **Figure 3.3A**, Zhou *et al.* prepared porous graphene *via* a carbothermal reaction between the metal oxide and graphene materials.^[26] The as-generated pores are uniform and nearly circular, with a size of 1-10 nm. In another work, Wang and co-workers reported the scalable synthesis of porous graphene *via* refluxing reduced GO in concentrated nitric acid. The porous graphene is not that regular, and the average size of pores is about 50 nm, which is much larger than the pores in Zhou's work (**Figure 3.3B**).^[27]

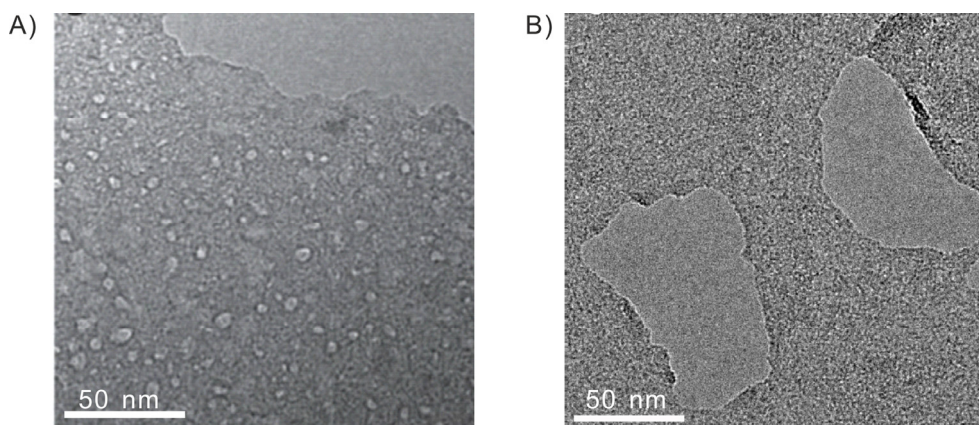


Figure 3.3 Structure of porous graphene. A) TEM images of porous graphene prepared from carbothermal reactions. Reproduced from ref.^[26] with copyright permission of Springer Nature 2014. B) TEM image of porous graphene from acid treatment. Reproduced from ref.^[27] with copyright permission of Springer Nature 2013.

Mechanical properties: The presence of the pores is disruptive to the integrity of the graphene lamellae; however, it was found that these pore structures did not negatively affect the mechanical properties of graphene, and some tests even showed that the mechanical strength of the porous graphene material was comparable to that of graphene.^[27-28] Wang and co-workers reported that the presence of the pores does not damage the lattice structure of other layers of graphene, thus maintaining the mechanical strength and stability of the material.^[27] In addition, the density of porous graphene is generally lower than that of graphene, so the volume ratio of porous graphene is larger at the same mass, resulting in an increase in its strength-to-weight ratio (**Figure 3.4**).^[28]

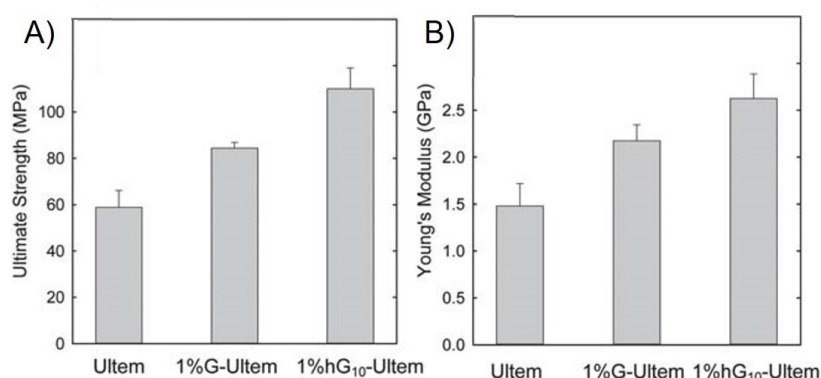


Figure 3.4 Comparisons of the A) ultimate strengths and B) Young's moduli of neat Ultem™ 1000 (Ultem), 1 wt% graphene-filled Ultem composite (1% G-Ultem), and 1 wt% hG10-filled Ultem composite (1% hG10-Ultem), respectively. Reproduced from ref.^[28] with the copyright permission of the Royal Society of Chemistry 2015.

Electronic properties: The bandgap is the defining characteristic of semiconductor materials and is vital for controlling conductivity electronically.^[29] One of the most significant advantages of porous graphene is that it possesses bandgap due to edge effects, which is not present in pure graphene.^[30] However, the theoretical bandgap values vary widely in different computations. For instance, Du and co-workers first demonstrated that the bandgap of porous graphene is 3.2 eV according to density functional calculations.^[31] Pierre and co-workers found that the bandgap of hydrogenated porous graphene was 3.95 eV by using hybrid HF-DFT functionals and all-electron Gaussian-type basis sets.^[32] In 2016, Zhang *et al.* prepared porous graphene with different sizes by using Fenton reaction, and the bandgap of porous graphene after 5 h etching is 3.878 eV, which is very close to the value of the theoretical calculation above.^[33] In addition, various porous graphene with a wide range of pore sizes from 4 nm to 2 μm with electron mobility ranging from 100 to 500 $\text{cm}^2/\text{V}\cdot\text{s}$ at various temperatures were reported by some research groups.^[34]

3.2.2 Preparation of porous graphene

Electron or ion-beam lithography: To create pores in a thin layer of material, mechanical force is an effective route. Lithography refers to using high-energy electron beams, ion beams, or photon beams to etch graphene materials to induce the removal, oxidation, or degradation of carbon atoms on the surface.^[35] The whole process only takes a few seconds to tens of seconds. For instance, Fischbein and Drndić reported the high-resolution manipulation of suspended multilayer graphene sheets by exposing them to the focused electron beam of a transmission electron microscope under specified conditions, thus creating nanometer-scale features that are stable and do not develop over time, including nanometer-scale pores, slits, and gaps.^[17] The advantage of this method is that it is fast, while the disadvantage is that it is cumbersome and costly to operate.

Thermal treatment: Annealing is a relatively simple and clean method for the preparation of porous graphene as no additional reagents are mostly needed.^[36] In this technique, the starting material (graphene, graphite oxide, GO, or reduced GO) is heated to achieve the oxidation, exfoliation, and reduction reactions requisite for porous graphene synthesis. For example, Yang and co-workers obtained porous graphene via annealing treatment of graphite oxide nanosheets with a high heating

rate.^[37] The generation of pores in graphene is shown in **Figure 3.5**. During the thermal decomposition of GO, the generated carbon-containing gases increase the pressure between graphite oxide layers. When the heating rate is high enough, the accumulating gases punch pores in graphite oxide sheets. The graphite oxide synthesized using Staudenmaier's or Hummers' method has many defective regions, which are chemically active and thus preferentially reacted involved in decomposition reactions, resulting in the porous structure.

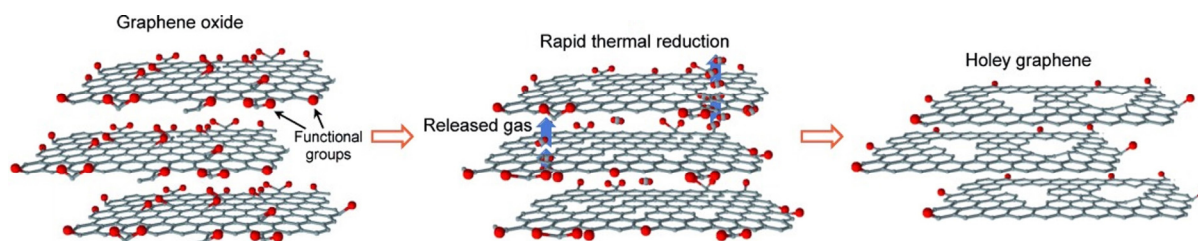


Figure 3.5 Schematic of formation mechanism for porous graphene through annealing treatment. Reproduced from ref.^[37] with copyright permission of Wiley-VCH 2015.

Catalytic oxidation: Due to the periodic arrangement of carbon atoms, the surface of graphene is inert, and it is difficult to react with other compounds under normal conditions. However, at a given temperature and with the assistance of catalysts, carbon atoms at specific places can be removed to generate gas, resulting in pores in the plane of graphene. For instance, Lin *et al.* reported a facile and controllable method to synthesize porous graphene using catalytic oxidation of graphite carbon with the assistance of silver (Ag) nanoparticles.^[28] The entire synthesis steps are shown in **Figure 3.6**. First, Ag nanoparticles were deposited on the surface of graphene to produce graphene-decorated Ag nanoparticles (Ag-graphene). Second, the Ag-graphene was heated in a tube furnace to induce controlled air oxidation. Third, the partially oxidized Ag-graphene was refluxed in nitric acid to remove the Ag nanoparticles.

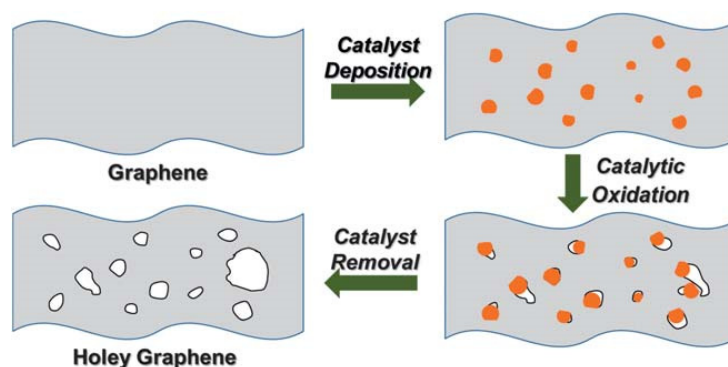


Figure 3.6 The 3-step process to prepare porous graphene. Reprinted from ref.^[28] with the copyright permission of the Royal Society of Chemistry 2013.

Pyrolysis: It refers to the high-temperature decomposition of organic substances in an inert atmosphere (usually almost oxygen-free).^[38] It was utilized decades ago to extract valuable fractions from petroleum. In recent years, this approach has gained increased interest for its application in transforming chemical molecules into carbon nanomaterials. For example, Neumann and co-workers developed a technique for the bottom-up fabrication of atomically thin graphene with controllable crystallinity and porosity utilizing aromatic self-assembled monolayers as precursors.^[39] In addition, the as-prepared porous graphene has high charge carrier mobility, making it desirable for electronic field-effect devices.

Wet etching: There are many kinds of chemicals that can be used for wet chemical etching, including acids, bases, radicals, etc.^[40] For instance, Fan and co-workers designed a simple approach for manufacturing a binder-free and free-standing N-doped porous graphene//polyaniline (PANI) slice that not only has a high packing density but also retains a highly linked pore connection channel for effective ion transport without compromising electrochemical energy storage (**Figure 3.7**).^[41] Furthermore, the N-doped porous graphene/PANI electrode could provide ultrahigh volumetric capacitance, excellent rate performance, and long-term cycle stability.

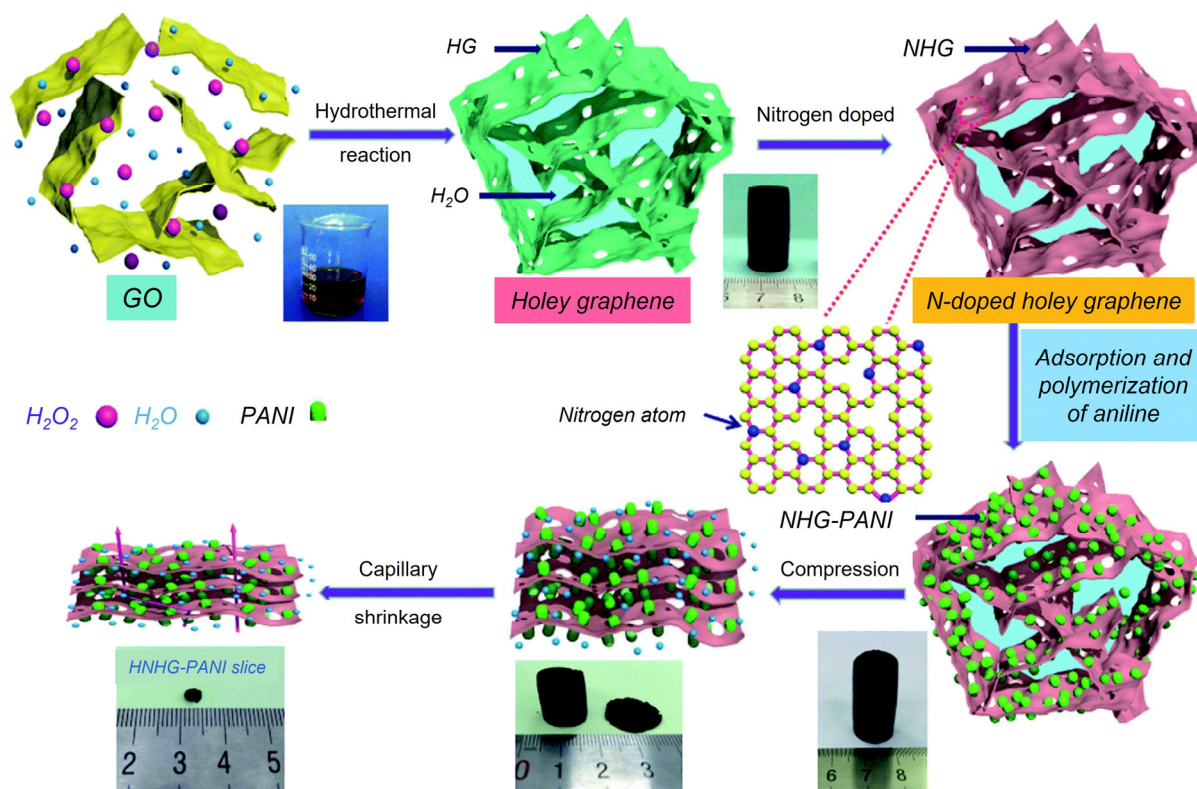


Figure 3.7 Schematic illustration of the high-density freestanding HNHG–PANI slice fabrication technique. Adopted from ref.^[41] with the copyright permission of the Royal Society of Chemistry 2017.

3.3 Graphene Quantum Dots

Graphene quantum dots (GQDs), a new type of carbon nanomaterial, are usually composed of single or few-layer graphene sheets with lateral dimensions of less than 100 nm.^[42] GQDs could be obtained by decreasing the graphene size in two-dimensional directions, which can be regarded as unique small graphene fragments. Compared with pure graphene, GQDs have a smaller size, a larger specific surface area, and exhibit a more obvious edge effect and quantum confinement effect, which makes them different from graphene in terms of photoelectric transmission properties.^[43] In addition, the quantum confinement effect primarily influences the electronic bandgap of GQDs.^[44] GQDs have been widely used in the research of chemistry, biology, physics, environmental science, and other fields because of their simple preparation, good stability, low toxicity, and good biocompatibility.^[45] The popularity of this area and the number of published items have increased at a phenomenal rate (**Figure 3.8**).

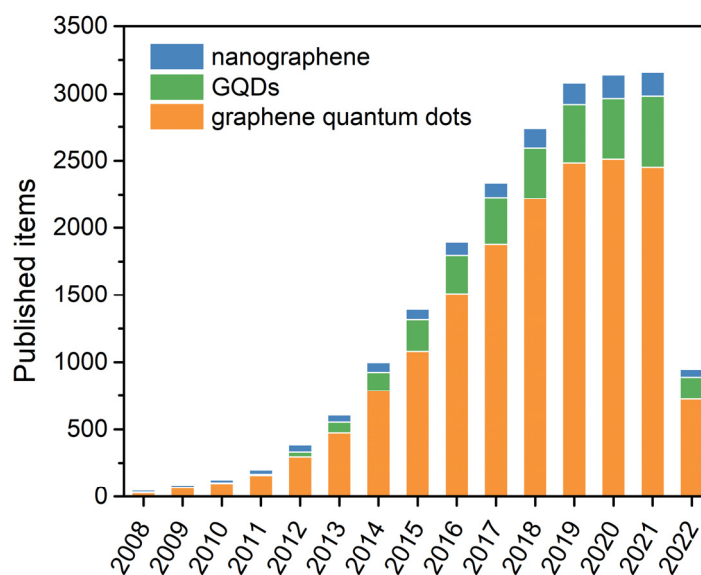


Figure 3.8 Publications item on topic of ‘graphene quantum dots’, ‘GQDs’, and ‘nanographene’ since 2008; search results obtained by Web of Science, May 2022.

3.3.1 Properties of graphene quantum dots

Structures: GQDs are generally composed of carbon, hydrogen, and oxygen elements, and recently, nitrogen atom doping has been commonly used to modulate the photoluminescence behavior of GQDs.^[46] Its lateral size is defined as less than 100 nm, and its thickness is around several nanometers (a few layers of graphene). In addition, unlike pure graphene, which is composed of sp² carbon, most graphene quantum dots have some sp³ carbon atoms. Most synthesized GQDs are nearly spherical or ellipsoidal, although triangular, quadrilateral, and hexagonal GQDs have also been synthesized.^[47] In addition, GQDs possess in-plane graphite lattice spacing of 0.20 - 0.24 nm (corresponding to different diffraction planes) and graphite layer spacing of 0.334 nm (or larger due to the presence of functional groups), as revealed by high-resolution transmission electron microscopy (HRTEM) and XRD characterizations (**Figure 3.9**).^[48]

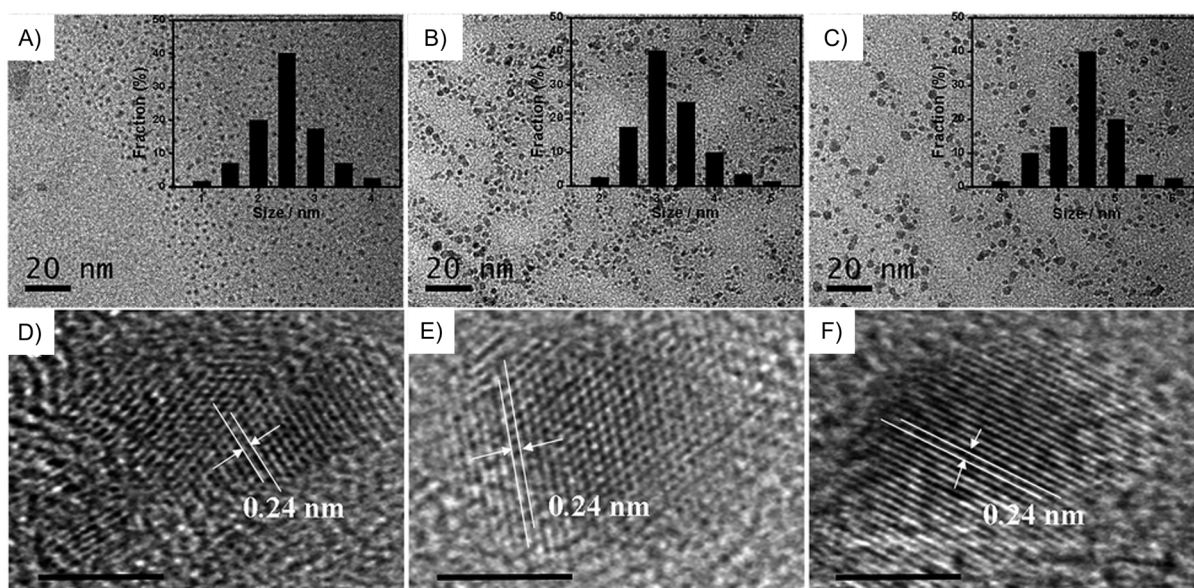


Figure 3.9 TEM and HRTEM images of GQDs_{purple-blue} (a, d), GQDs_{blue} (b, e), and GQDs_{green} (c, f), respectively. Reproduced from ref.^[48] with the copyright permission of the Royal Society of Chemistry 2015.

Optical Properties: GQDs have strong optical absorption in the UV region and a long tail extending up to the absorption edges of 700 nm.^[49] Specifically in the UV region, as shown in **Figure 3.10A**, the π - π^* transition at around 230 - 270 nm originates from C=C in the core, and the n - π^* transition at about 320 - 450 nm originates from C=O, C=N, and other functional groups in the edge.^[50] In addition, the absorption peaks of GQDs obtained by different preparation methods are different due to their varying sizes and various surface functional groups. GQDs differ from graphene in their unique fluorescence properties, as pure graphene is non-fluorescent. The origin of the photoluminescence of GQDs can be attributed to two types: one is the intrinsic state emission related to size, edge type, and local electron-hole pair recombination; the other one is the defect state emission related to defects in GQDs.^[51] So far, numerous kinds of GQDs have been prepared, with emission wavelengths ranging from visible to near-infrared regions. As shown in **Figure 3.10B**, the GQDs exhibit excitation-dependent and nearly white emission.

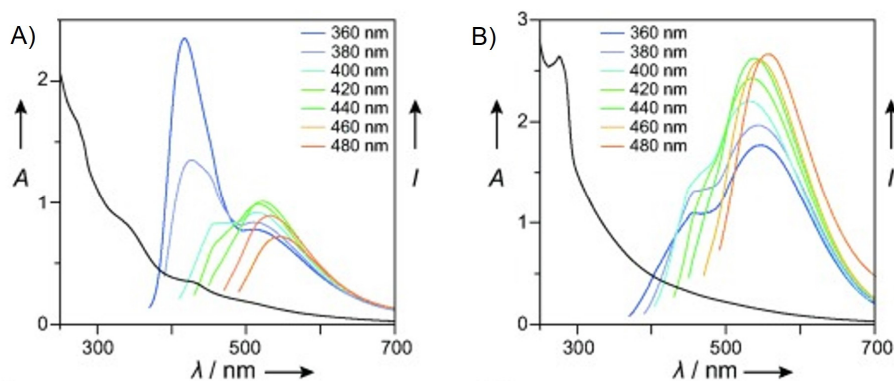


Figure 3.10 UV/Vis absorption and fluorescence spectra of two kinds of GQDs. Reproduced from ref.^[50] with copyright permission of Wiley-VCH 2014.

3.3.2 Solvent effects on optical properties

Solvatochromism: Researchers discovered that the UV/Vis and near-infrared absorption and emission spectra of the fluorophore are largely affected by the surrounding solvent molecules. The position, intensity, and sometimes even the shape of the absorption bands and emission peaks change with the solvent, which is called solvatochromism (**Figure 3.11**).^[52] If the spectral peak shows red-shift (bathochromic shift) with increasing solvent polarity, it is called positive solvatochromism, and conversely, if blue-shift (hypsochromic shift) occurs, it is called negative solvatochromism. The factors that affect solvatochromism are complex, including hydrogen bonding, charge transfer, solvent polarity, proton transfer, probe-probe interactions, conformational changes, *etc.*^[53] It is difficult to determine which effect is dominant in a given system, and in many cases, multiple effects act simultaneously.^[54]

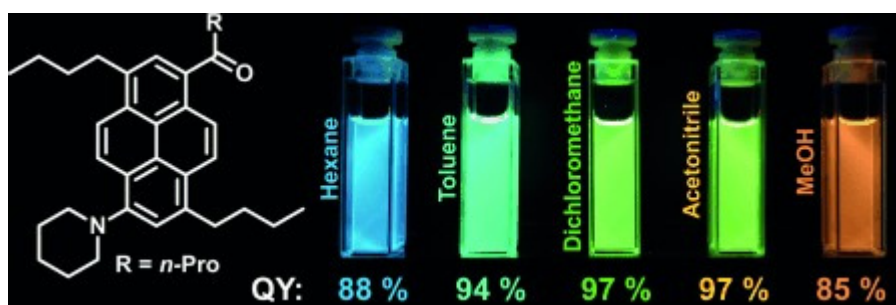


Figure 3.11 Fluorescence images and quantum yields of Prodan among different solvents. Reprinted from ref.^[52] with copyright permission of Wiley-VCH 2013.

Solvent effects on GQDs: In 2011, Zhu and co-workers prepared fluorescent GQDs *via* a one-step solvothermal method, and the GQDs possessed bright fluorescence, low toxicity, and good biocompatibility.^[55] In addition, they found that the GQDs could be dissolved in water and many other polar solvents, and the FL emission peak of GQDs shifts from 475 nm to 515 nm when the solvent changes from THF to water. The authors assigned the solvent effect to different emissive traps or solvent attachments. In 2016, Niu and colleagues demonstrated the solvent-dependent absorption and emission behaviors of GQDs *via* time-dependent density functional theory (**Figure 3.12**).^[56] They found that compared with that in the gas phase, the absorption peak of GQDs shows a red-shift in low polarity solvent (toluene) and even stronger in higher polarity solvent (THF). They proposed that the higher polarity induced a larger surface charge external potential.

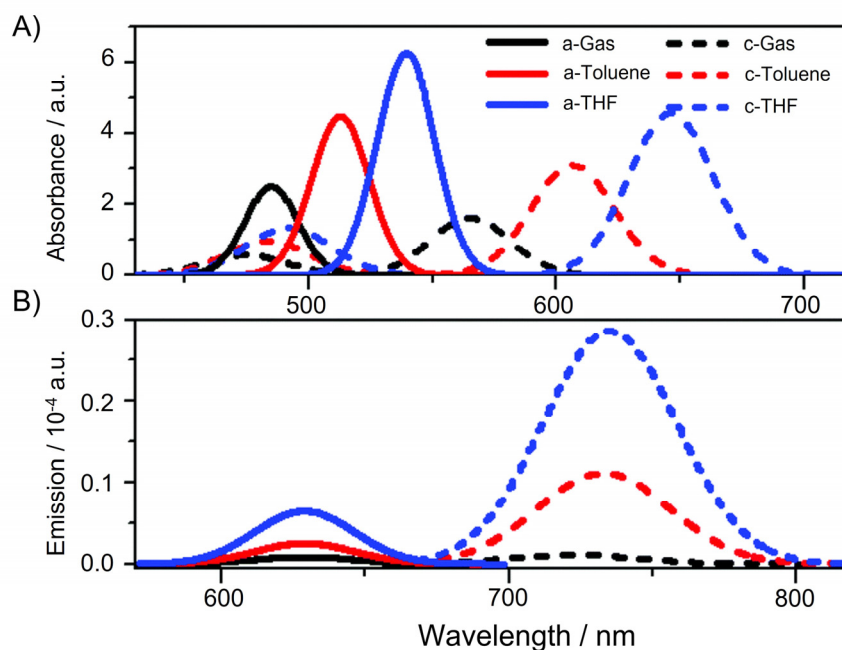


Figure 3.12 Absorption (A) and emission (B) spectra of a: the pristine GQDs and c: the pyridazine N-doped GQDs in gas phase, toluene, and THF, respectively. Reproduced from ref.^[56] with the copyright permission of the Royal Society of Chemistry 2016.

3.4 Purpose and Significance of the Study

By imparting the advantages of pores into graphene, porous graphene has attracted extensive attention from researchers for its high specific surface area with a unique porous structure, and chemical diversity while maintaining excellent electronic conductivity.^[21, 57] These extraordinary properties enable porous graphene materials

to be used in many applications, including energy storage and conversion, gas sensors, water desalination, *etc.*^[20c, 58] In recent years, numerous strategies, such as annealing, activation by metal catalysts, focused electron beam etching, bottom-up synthesis employing aromatic molecules, and chemical etching, have been devised to generate pores in graphene.^[17, 37, 39, 41] Among them, chemical etching provides a low-cost and easily-operated route. Hence, for my first project, a solution-processible method based on chemical etching is proposed to synthesize porous graphene. Compared with previous research, oxo-G with a controlled defect density herein is used as a precursor to prevent the flake disintegration, and hydroxyl radicals generated from ferrous catalyzed H₂O₂ photolyzed under UV light photolysis are used as etching agents to produce pores in oxo-G. Moreover, the chemical composition of oxo-G has been taken into consideration, and the plausible mechanism for how hydroxyl radicals initiate the reactions around the defects is further proposed. We hope this work will open up new strategies for the rational design of porous graphene materials and develop controlled chemistry at the rims of pores.

During the last project of synthesizing porous graphene, we found a kind of side product was generated when we expanded the etching time. The side product was blue-fluorescent, which was confirmed to be graphene quantum dots (GQDs). GQDs are a top-rated new class of graphene-based nanomaterial in recent years, and one of the most valuable properties of GQDs is their photoluminescence.^[50, 59] However, the mechanism of the photoluminescence of GQDs is still under discussion. It has been shown that the photoluminescence of GQDs is mainly controlled by its core structure and the surface or edge groups.^[51c] In addition, the researchers found that the solvent has an important influence on the optical properties of GQDs, but the influencing factors are very complex.^[56] The researchers generally agree that it is related to solvent polarity, but the exact reason remains to be investigated. Hence, for my second project, solvent-sensitive GQDs are prepared, which makes it much easier to study the solvent effect of GQDs on their optical properties. A series of protic or aprotic solvents with varying polarity and proticity have been used to unravel a possible mechanism for fluorescent behavior. Furthermore, their potential to detect the water in organic solvents has been tentatively figured out. We hope the work will pave the way for the rational design and fabrication of GQDs with precise control over their functional properties.

4 Characterization and Testing Techniques

Characterization and testing techniques are fundamental to identifying nanomaterials, recognizing their diverse structures, and evaluating their unique properties.^[60] The main purpose of the characterization of nanomaterials is to determine physicochemical properties such as morphology, size, chemical composition, and optical properties of nanomaterials.^[61] The characterization and testing techniques of graphene-related nanomaterials in my research can be divided into the following parts: 1) morphological characterization; 2) compositional and structural analysis; 3) optical property characterization; 4) Langmuir Blodgett (LB) technique.

4.1 Morphological Characterization

Among the morphological characterizations of graphene-related nanomaterials, atomic force microscopy (AFM) and transmission electron microscopy (TEM) are widely used.^[62]

4.1.1 Atomic force microscopy

The basic setup of the AFM is shown in **Figure 4.1A**, which mainly consists of cantilever, tip, scanner, laser source, photodetector, feedback system, and imaging system.^[63] A feedback reference is pre-set when the scanner drives the probe close to the sample surface. The laser detector collects the changed signal generated by the interaction between the probe and the sample and then transmits it into the feedback system. The difference between the two signals is called the error signal. When the error signal occurs, the feedback system controls the scanner to move or change the voltage to maintain the measured value in agreement with the reference value so that the imaging system can record the surface information of the sample.^[64] Depending on the physical quantities fed back to the feedback system, the operation of AFM can be divided into the following modes: contact mode, non-contact mode, and tapping mode.^[65] **Figure 4.1B** shows the AFM image of porous graphene, which was collected in the tapping mode. From the figure, we can see that there are many pores on the surface of graphene, and these pores are nearly-circular. The advantages of AFM are the simplicity of sample preparation, high resolution, and the ability to image in three dimensions. The disadvantage of AFM is that the scanning

range is small and limited by sample factors, and tiny artifacts generated by background noise can be detected.

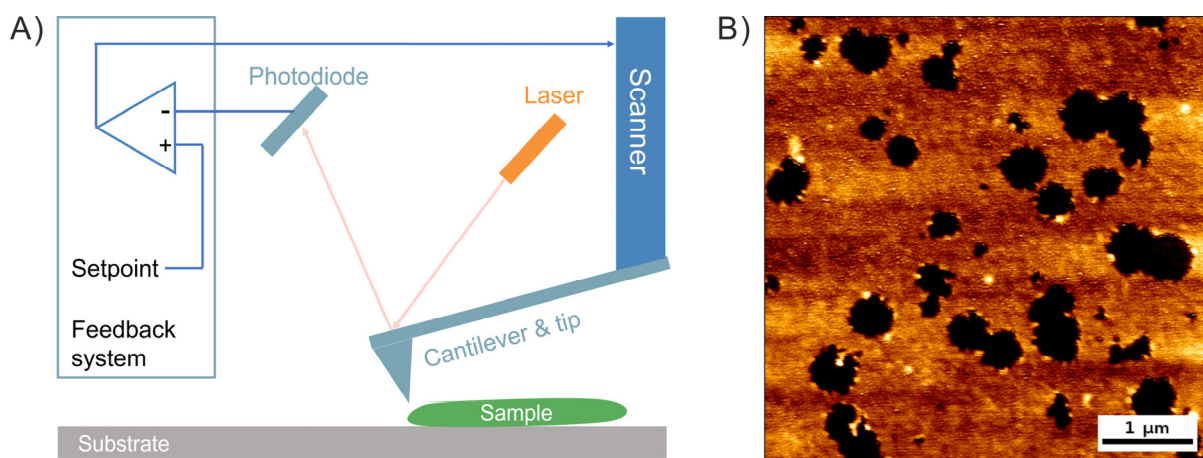


Figure 4.1 A) The basic working principle of AFM. B) AFM image of porous graphene.

4.1.2 Transmission electron microscopy

Transmission electron microscopy (TEM) is often used for the morphological analysis of nanomaterials.^[66] The components and optical path of the TEM are shown in **Figure 4.2 A**. The TEM is composed of the following components: electron source, condenser lenses, condenser aperture, objective aperture, select area aperture, intermediate lenses, project lens, and screen. These components can be classified into two main systems: the condenser system and the objective system. The condenser system is located in front of the sample and serves to obtain the ideal light source; the objective system is located behind the sample and serves to amplify and optimize the imaging. The principle of the imaging system in TEM is the Abbe theory of imaging.^[67] A parallel electron beam is incident on the periodic structure of the sample resulting in diffraction. After the objective lens is focused on the focal plane to reach diffraction extremes, a magnified phase of the sample is produced in the image plane. **Figure 4.2B** shows the TEM image of a flake of porous graphene, from which we can see that even small holes of a few nanometers are apparent, with a level of resolution that cannot be achieved by optical microscopy and AFM.

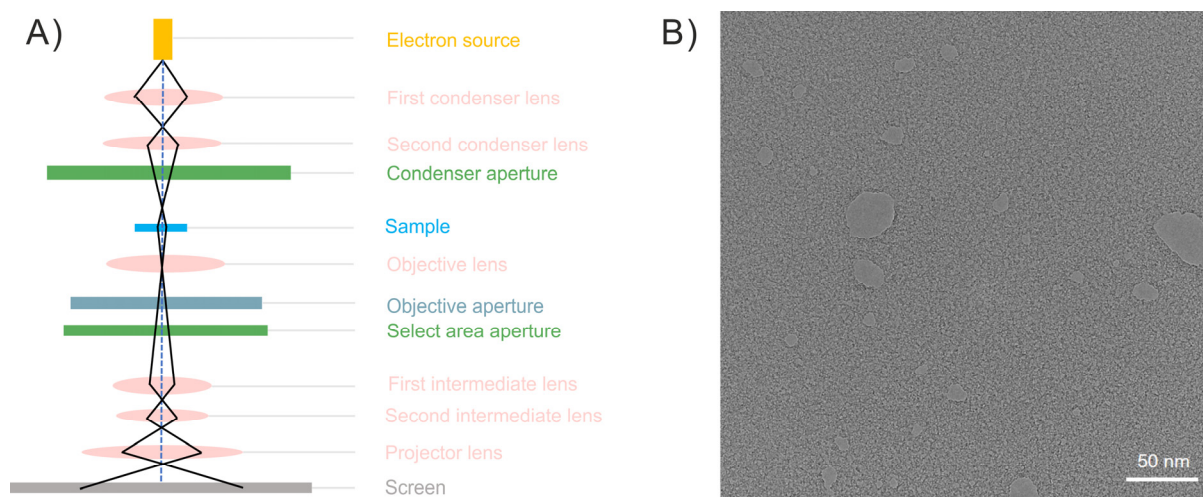


Figure 4.2 A) The components and optical path of the TEM. B) TEM image of porous graphene.

4.2 Compositional and Structural Analysis

The physicochemical properties of nanomaterials are closely related to the chemical composition and structure of the constituent nanomaterials.^[68] Therefore, it is vital to determine the elemental composition and structure of nanomaterials. Relevant characterization and analysis methods include Fourier-transform infrared (FTIR) spectroscopy, Raman spectroscopy, X-ray photoelectron spectroscopy (XPS), nuclear magnetic resonance (NMR) spectroscopy, and CHNS elemental analysis (EA).

4.2.1 Fourier-transform infrared spectroscopy

Infrared (IR) spectroscopy is essentially an analytical method for determining the molecular structure and identifying compounds based on information such as relative vibrations and molecular rotations between atoms within a molecule.^[69] Infrared absorption spectroscopy records the vibration and rotation of molecules, and the atoms of chemical bonds or functional groups are in a state of constant vibration (or rotation), whose vibration frequency is comparable to that of infrared light.^[70] Therefore, when a molecule is irradiated with infrared lights, the chemical bonds or functional groups in the molecule can absorb and vibrate, and chemical bonds or functional groups have their corresponding absorption frequencies and will be in specific positions on the infrared spectrum, so that information about what kind of chemical bonds or functional groups are contained in the molecule can be obtained. The energy difference between rotational levels of molecules is relatively small, the absorbed light frequency is low, and the wavelength is long, so the pure rotational spectrum of

molecules appears in the far-infrared region. The energy difference between vibrational energy levels is much larger than that in rotational energy levels, and the light frequency related to vibrational energy level transition of molecules is higher, so the pure vibrational energy spectrum of molecules generally appears in the mid-infrared region. In the mid-infrared region, there are two main vibrational modes of the groups in the molecule, namely stretching vibration and bending vibration.^[71] The stretching vibration refers to the movement of the atoms in the moiety back and forth along the valence bond direction (both symmetric and asymmetric), while the bending vibration refers to the movement perpendicular to the valence bond direction (for example, rocking, twisting, wagging). The most commonly used infrared spectrometer is Fourier-transform infrared (FTIR) spectroscopy, which has the components shown in **Figure 4.3A** and consists mainly of an infrared light source, laser, movable mirror, fixed mirror, detectors, and Fourier transformation part.^[72] **Figure 4.3B** shows the FTIR spectrum of oxo-functionalized graphene (oxo-G), from which the following functional groups are present: stretching vibrations of O-H and adsorbed water at about 3400 cm^{-1} , stretching vibrations of C-H at around 2900 cm^{-1} , stretching vibrations of C=O at 1730 cm^{-1} , deformation vibrations of the O-H at 1400 cm^{-1} , stretching vibrations of C-O-C at 1225 cm^{-1} , and C-O stretching mode at 1050 cm^{-1} .^[73]

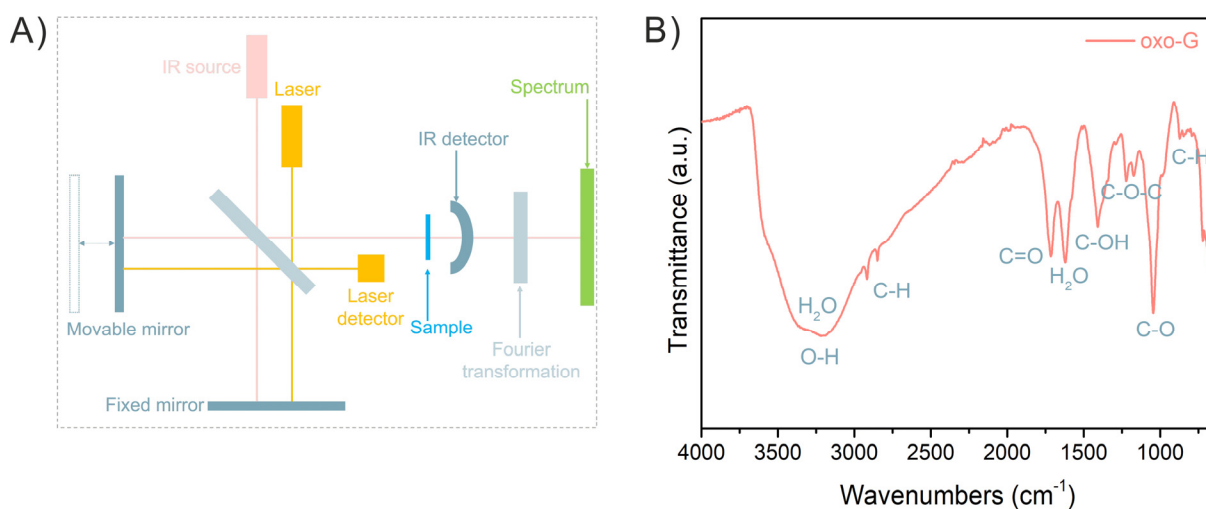


Figure 4.3 A) The components of FTIR spectroscopy. B) FTIR spectrum of oxo-G.

4.2.2 Raman spectroscopy

Raman spectroscopy is a powerful technique for the characterization of graphene-related materials. It's a kind of scattering spectra based on the interaction of light and material.^[74] For light scattering, when high-intensity incident light from a laser source is scattered by molecules, most of the scattered light has the same wavelength as the incident laser, which is called Rayleigh scattering (**Figure 4.4A**).^[75] However, a tiny fraction of the scattered light has a different wavelength (color) than the incident light. The change in wavelength is determined by the chemical structure of the test sample, which is called Raman scattering and was discovered by Indian scientist Chandrasekhara Venkata Raman.^[76] Raman scattering has two different energy differences of transition and thus produces two different spectral, as shown in **Figure 4.4A**. The scattering whose frequency is less than the incident light frequency is called Stokes Raman scattering, and the other one whose frequency is larger than the incident light frequency is called anti-Stokes Raman scattering.^[77] In general, the Stokes Raman scattering is more intense than the anti-Stokes Raman scattering, due to the Boltzmann distribution, where the number of particles in the vibrational ground state is much larger than the number of particles in the vibrational excited state. **Figures 4.4B** and **C** show the Raman spectrum and statistical Raman spectra of reduced oxo-G (r-oxo-G), respectively. In **Figure 4.4B**, the D mode appears at around 1350 cm^{-1} , which is attributed to the breathing mode of six-membered in graphene; The peaks located at around 1580 cm^{-1} and 2700 cm^{-1} are assigned to the G mode and 2D mode of graphene, which originate in a first-order Raman scattering and two-photon process, respectively.^[78] In a simplified model, the D, G, and 2D modes can be correlated in order to extract the density of defects in graphene-based samples.^[79] As shown in **Figure 4.4C**, with the increase in density of defects (decreasing with the average distance between the defects, L_D), the I_D/I_G ratio first reaches a maximum of around 4, then decreases. In **Figure 4.4D**, it can be seen that the I_D/I_G ratio is 3.3, and the full width at half maximum (FWHM, Γ) of the 2D peak of r-oxo-G is about 83 cm^{-1} , indicating that the L_D is around 2.2 nm, and the density of defect is about 0.5%.

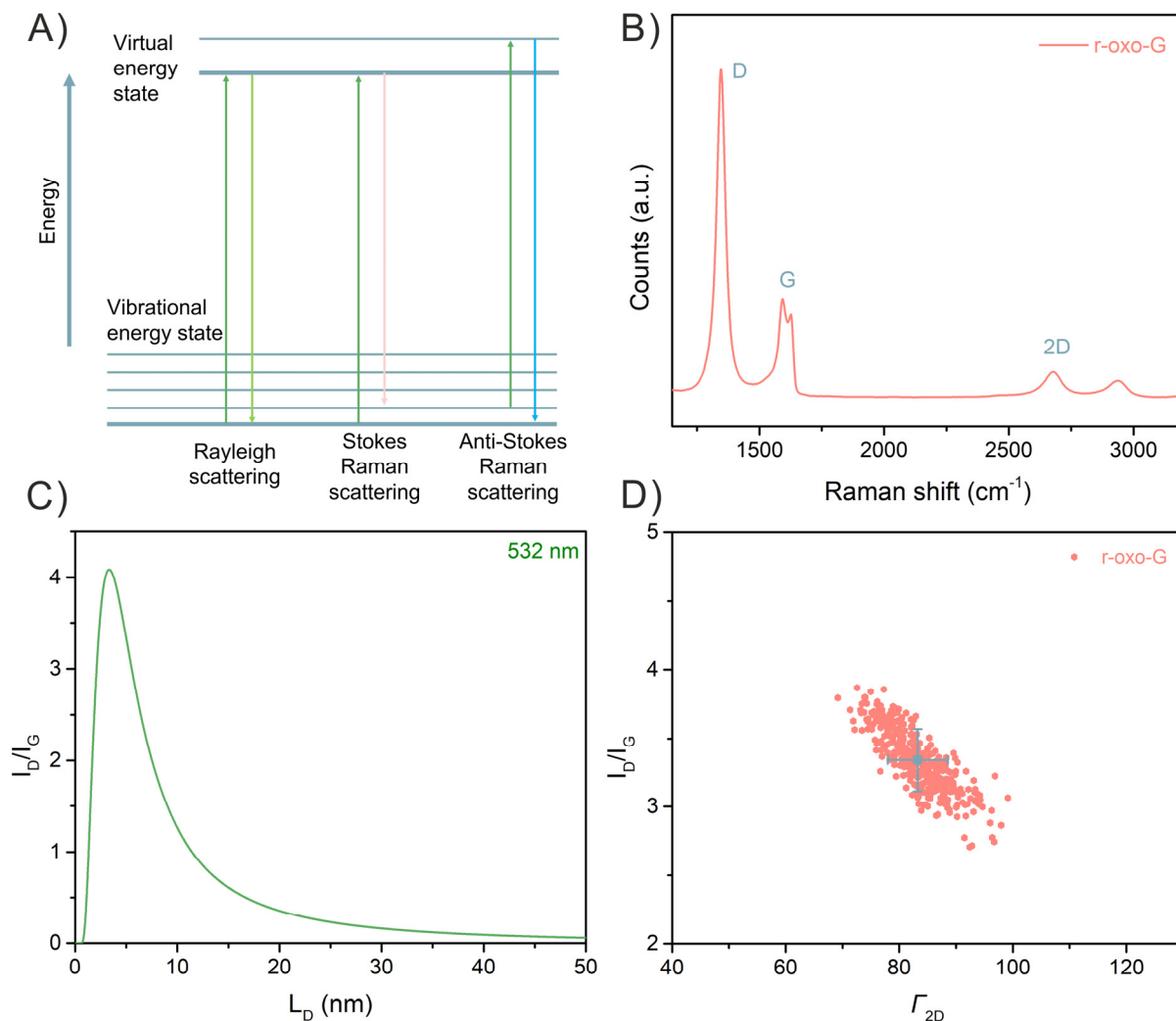


Figure 4.4 A) The energy level diagram shows the different scattering. B) Raman spectrum of r-oxo-G. C) Relation between I_D/I_G and L_D fitted by Cançado and Lucchese's approach.^[79] D) Statistical Raman spectroscopy applied on r-oxo-G. Γ : full-width at half-maximum.

4.2.3 X-ray photoelectron spectroscopy

X-ray photoelectron spectroscopy (XPS) is a method that uses an electron spectrometer to measure the energy distribution of photoelectrons and Auger electrons emitting from the surface of a sample when irradiated with X-ray photons.^[80] XPS can be used for qualitative as well as semi-quantitative analysis. The basic principle of XPS is photoionization: when a photon is radiated on the sample surface, the photon can be absorbed by an electron in the atomic orbit of an element in the sample, causing the electron to release from the nucleus and emit with specific kinetic energy from inside the atom to become a free photoelectron, while the atom itself becomes an excited ion.^[81] For a particular monochromatic excitation source and a specific atomic orbital, the energy of the photoelectron is characteristic. When the

energy of the excitation source is fixed, the energy of its photoelectrons is only related to the type of element and the atomic orbitals ionized for excitation. Therefore, we can qualitatively analyze the elemental species of a substance based on the binding energy of the photoelectrons. In addition, the electron binding energy of the inner shell layer of an atom changes depending on the chemical environment in which it is located, and this change is recorded as a shift of the spectral peak (binding energy) to form the spectrum. This difference in the chemical environment results from the type or number of elements bound to the atom, or it can be regarded that the atom has different chemical valence states. **Figure 4.5A** shows the basic structure of the XPS instrument, including the light source, electron lens, electron energy analyzer, and detector. **Figure 4.5B** shows the high-resolution C 1s XPS spectrum of oxo-G. The C 1s spectrum can be split into three peaks. The one located at 284.6 eV is assigned to the graphitic C-C bonds; another two peaks are contributed to the C-O/C-OH and C=O/COOH, respectively.^[82] The shortcoming of XPS is that it is limited to surface analysis; however, XPS is quite reliable for graphene-related nanomaterials as they have layered structures.

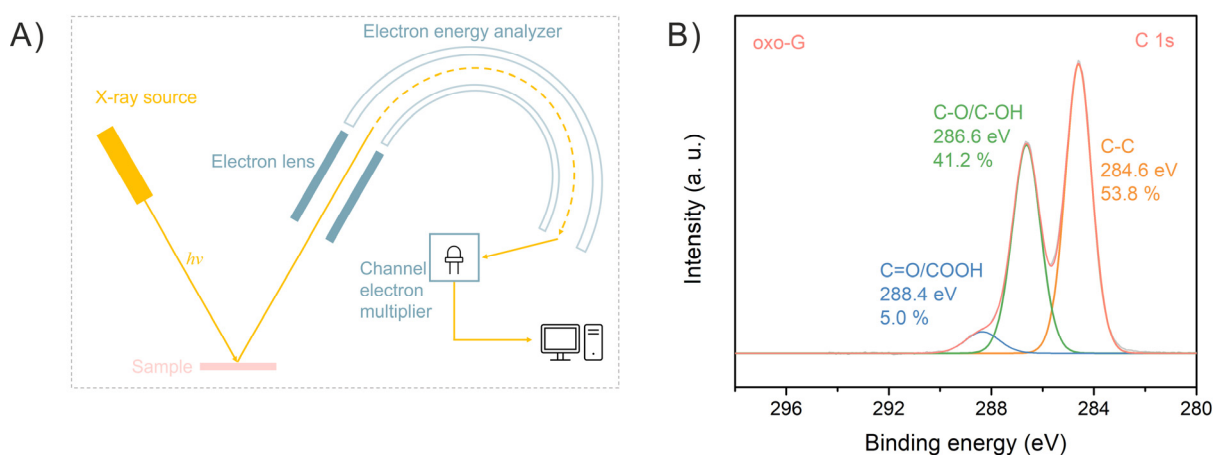


Figure 4.5 A) The components of XPS. B) High-resolution C 1s spectrum of oxo-G.

4.2.4 Nuclear magnetic resonance spectroscopy

Nuclear magnetic resonance (NMR) spectroscopy is a method of determining the molecular structure and chemical composition of a sample.^[83] It works by studying how spinning nuclei interact in a strong magnetic field. A steady external magnetic field causes specific nuclei in a molecule to absorb their corresponding radio frequencies in NMR spectroscopy. Nuclear spins undergo a transition due to the energy absorbed, which may be visualized on an NMR spectrum. For graphene-related materials, they

are materials rather than small molecules. In this situation, solid-state NMR (ssNMR) is developed to collect NMR spectra.^[84] At the same time, new problems appear. One problem is that the natural abundance of ^{13}C is only 1.1%. On the other hand, ^{13}C nucleus has various orientations in the external magnetic field, resulting in broad absorption lines. A new technique named magic angle spinning (MAS) is utilized for ssNMR.^[85] Rotating the probe up to 70 kHz at the magic angle of 54.74° in relation to the external magnetic field can significantly diminish the dipolar interaction and anisotropy of the chemical shift. **Figure 4.6** shows the ^{13}C ssNMR spectrum using the MAS technique. The following are observed in the spectrum, graphitic sp^2 domain at 133 ppm, lactol signal at 100 ppm, tertiary alcohols at about 70 ppm, and epoxides at about 60 ppm.^[86]

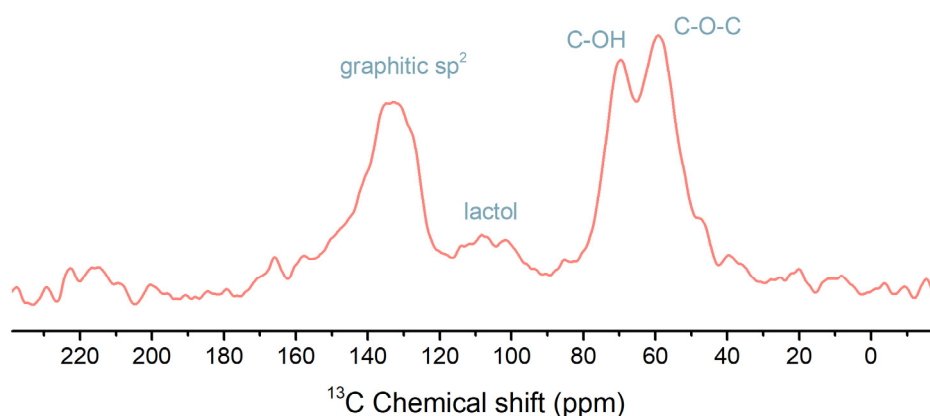


Figure 4.6 MAS ^{13}C ssNMR spectrum of oxo-G.

4.2.5 CHNS elemental analysis

CHNS elemental analysis (EA) is often used to determine the elemental content of carbon, hydrogen, nitrogen, and sulfur in graphene-related samples.^[87] EA is a reliable and efficient technique for assessing the purity and chemical composition of graphene-related materials. It works by the combustion of the sample by high-temperature oxidation in the presence of a composite catalyst to produce N_2 , nitrogen oxides, carbon oxides, sulfur oxides, and water, which are driven by a carrier gas into a separation and detection unit. After the adsorption column retains the compounds of non-nitrogen elements by adsorption, the nitrogen oxides are reduced to nitrogen gas and then determined by the detector. Other oxides are then separated and determined in the order of carbon, hydrogen, and sulfur by the adsorption resolution of the adsorption-desorption column. The advantage of elemental analysis is that it is low-cost and efficient, and it requires only a very small amount (~ 1 mg) of sample.

4.3 Optical Property Characterization

4.3.1 Ultraviolet/Visible absorption

Ultraviolet/Visible (UV/Vis) spectroscopy is a powerful tool for determining the concentration of graphene-related materials and evaluating their functionalization degree.^[88] The transitions of valence electrons of molecules (or ions) need the absorption of UV or visible light (usually 200-800 nm), which can be detected to export UV/Vis absorption spectra. The UV/Visible spectrum shows a broad band because the interelectronic energy transition is always accompanied by a vibrational and rotational energy transition. In compounds, there are σ -electrons forming single bonds, π -electrons forming unsaturated bonds, and lone pairs of n -electrons. When the molecule absorbs UV or visible radiation, these outer electrons will jump from the ground state (bonding orbitals) to the excited state (antibonding orbitals), and there are four main ways of transition, with the order of energy required: $\sigma \rightarrow \sigma^* > n \rightarrow \sigma^* > \pi \rightarrow \pi^* > n \rightarrow \pi^*$. Considering the unique chemical composition of every molecule, it has its own fixed absorption spectrum, giving constant external conditions. The quantitative analysis principle of UV/Vis is the Lambert-Beer law, which describes the relationship between the intensity of light absorption by a substance at a certain wavelength, the concentration of the substance, and optical path length.^[89] The expression is $A = \epsilon bc$, where A is the absorbance, ϵ is the molar absorption coefficient, b is the optical path length, and c is the concentration of the substance. **Figure 4.7A** shows the composition of the UV/Vis instrument, which includes the light source, monochromator, detector, and signal processing system. **Figure 4.7B** shows the UV/Vis spectrum of oxo-G, where the absorption band located at 230 nm is attributed to the $\pi \rightarrow \pi^*$ transition, while the one located at around 300 nm is attributed to the $n \rightarrow \pi^*$ with C=O in oxo-G.^[90]

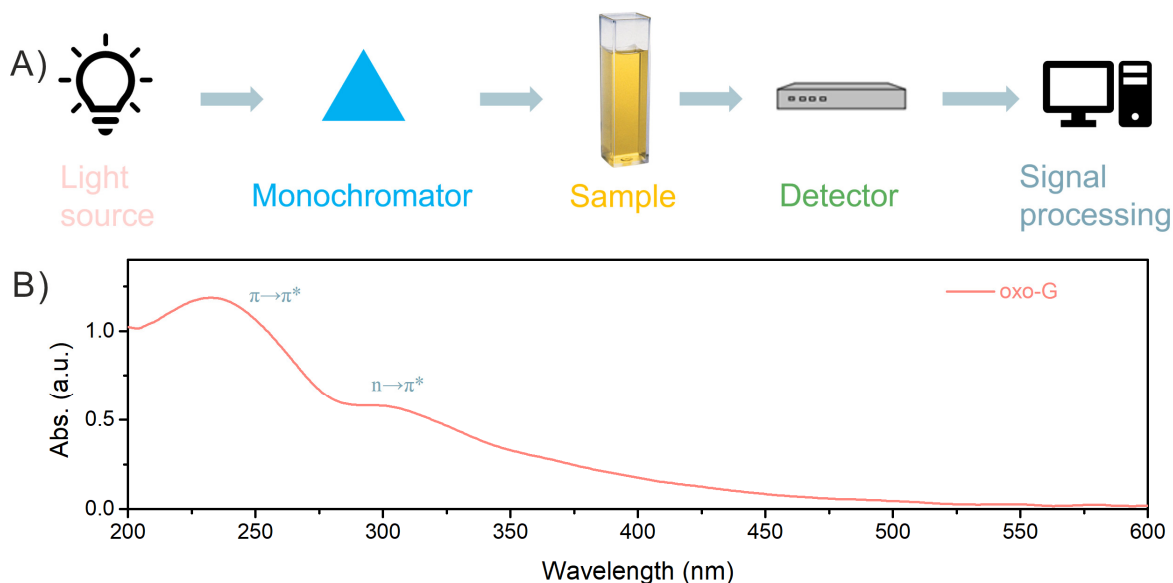


Figure 4.7 A) The components of UV/Vis spectroscopy. B) UV/Vis spectrum of oxo-G aqueous solution.

4.3.2 Fluorescence

Fluorescence (FL) is a form of photoluminescence.^[91] **Figure 4.8A** shows a common type of energy level diagram, Jablonski diagram, in which S_0 , S_1 , and S_2 represent the electronic ground state, the first and second electronic excited states of the molecule, respectively.^[92] Substances may absorb the energy of photons when they are irradiated by light, and then their electrons may jump from the ground state (S_0) to the excited state (S_1 , S_2). While the excited state electrons are unstable, they will move from the S_1 or S_2 state back to the S_0 state and simultaneously emit light, called FL. Besides FL, the excited electrons can also relax *via* generating heat or in other forms of energy loss. If the electron is converted from the S_1 state to the first triplet (T_1) excited state by intersystem crossing and then moves back to the S_0 state, phosphorescence is emitted. This is the fundamental difference between phosphorescence and FL. The difference between the S_1 excited state and the T_1 excited state mainly lies in the orientation of electron spin (singlet and triplet state, respectively).

In terms of measurement, FL spectra could be classified into FL excitation spectra (FL_{ex}) and FL emission (FL_{em}) spectra. Both excitation and emission FL spectra record the variation of FL intensity with wavelength. The FL_{em} spectrum of most substances is red-shifted compared to the excitation spectrum, known as the Stokes shift. As shown in **Figure 4.8A**, electrons in the excited state (S_1 or S_2) normally do not directly radiatively move back to the ground state (S_0) for FL emission, but first undergo such

non-radiative transmissions as vibrational relaxation, internal conversion, *etc.* Similarly, the electrons that are in the ground state also have to undergo a series of vibrational relaxation since there are a series of vibrational levels even in the ground state. All these processes lead to energy loss, which is reflected in the spectra as red-shift.

FL quantum yield (QY) and lifetime are vital criteria for evaluating fluorescent performance.^[93] Quantum yield is the ratio of the number of photons emitted ($N_{photons\ emitted}$) by a fluorescent substance to the number of photons absorbed ($N_{photons\ absorbed}$); the equation is $QY = N_{photons\ emitted}/N_{photons\ absorbed}$. Indeed, there are absolute and relative QY values, which are obtained by two distinguished measurements. The method to obtain absolute quantum yield does not require a standard as a reference, and its error is relatively small. The other method is to calculate the quantum yield of the substance by measuring the integrated FL intensity of the substance and another substance with a known quantum yield under the same excitation conditions, then making the comparison using the other substance as an internal reference. The FL lifetime can be understood as the average residence time of all molecules in a substance in the excited state. For the lifetime measurement, generally, the sample is excited with a laser pulse signal of a specific wavelength. Then the decay of the signal emitted from the sample is observed, and the resulting curve is called the lifetime decay curve. The lifetime could be calculated with the slope of decay.

Pure graphene is a zero-bandgap material and is not expected to show FL. However, the bandgap could be open *via* functionalization or shrinking to nanoscale lateral dimensions. In this regard, oxo-G is fluorescent due to its functionalization with oxygen-related functional groups. GQDs are also fluorescent due to the functionalization and quantum confinement. **Figure 4.8B** shows the FL_{ex} and FL_{em} spectra of GQDs, and the Stokes shift can also be observed.

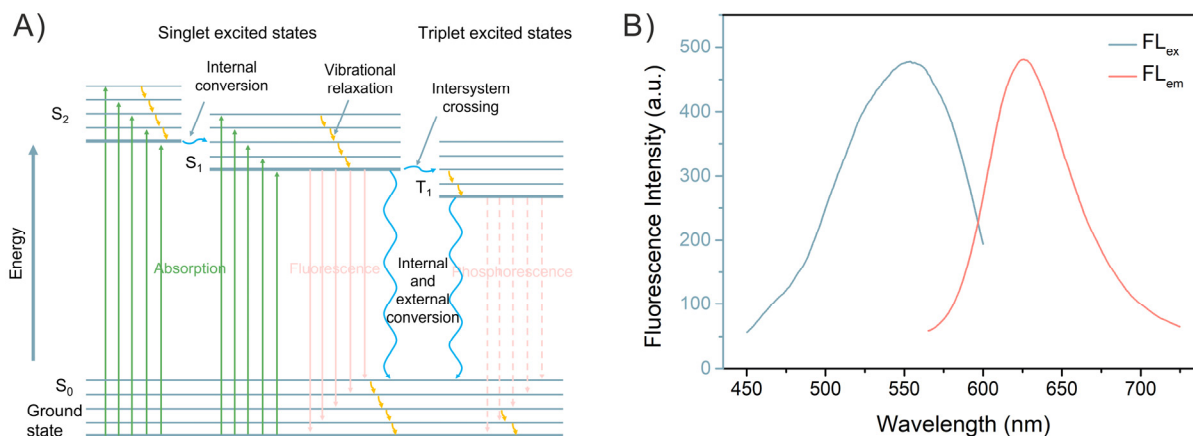


Figure 4.8 A) Jablonski diagram showing the process of absorption and multiple ways of relaxation. B) FL_{ex} and FL_{em} spectra of GQDs.

4.4 Langmuir-Blodgett Technique

Langmuir-Blodgett (LB) technique is a film-forming method that can be designed and controlled from the molecular scale.^[94] The film thickness can be governed by the number of molecule layers, so the molecules in the film have an ordered layer structure and high anisotropy as designed, and the method can be used to obtain large-area single-molecule films with almost no defects. For oxo-G, the LB technique allows simple and fast preparation of monolayer film, which is further used for characterization by Raman spectroscopy, AFM, *etc.* **Figure 4.9A** illustrates the assembly of amphiphilic molecules in the LB device, where the sample is first dissolved in a spreading solvent.^[95] The solute molecules form a neatly oriented monomolecular film at the gas-liquid interface; under compression, a dense monomolecular layer film is gradually formed at the interface; at a constant surface pressure, the monomolecular layer film is transferred to the solid substrate. **Figure 4.9B** shows the oxo-G flakes are successfully deposited onto the wafer.

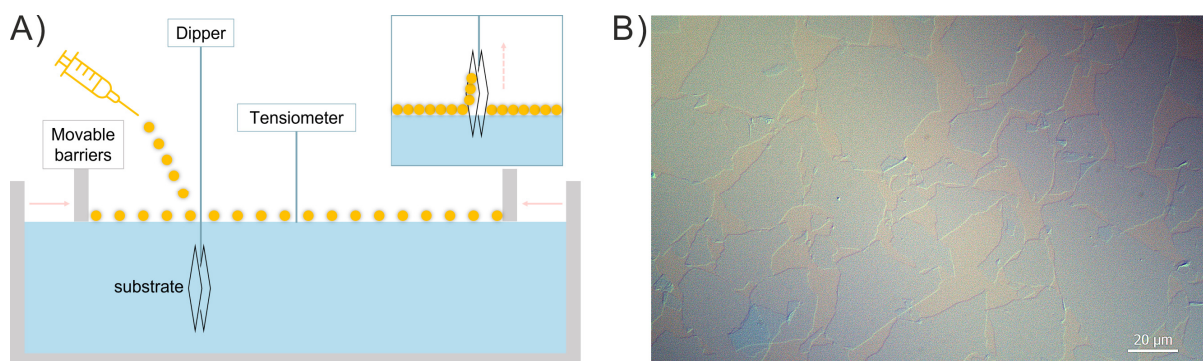


Figure 4.9 A) Schematic illustration of LB device. B) Optical image of oxo-G deposited by LB.

5 Main Contributions

5.1 Wet-Chemical Synthesis of Solution-Processible Porous Graphene *via* Defect-Driven Etching

Authors	Y. Hu, Q. Cao, C. Neumann, T. Lehnert, F. Börrnert, Y. Wang, U. Kaiser, A. Turchanin, S. Eigler
Journal	<i>Carbon</i> 2021 , 185, 568-577
DOI	10.1016/j.carbon.2021.09.027
Links	https://doi.org/10.1016/j.carbon.2021.09.027 https://www.sciencedirect.com/science/article/pii/S0008622321009180
Detailed scientific contribution	<p>The concept of this manuscript was elaborated by Y. Hu and Prof. Dr. S. Eigler.</p> <p>Y. Hu conducted etching experiments, prepared samples for analyses and wrote manuscript. Q. Cao prepared samples for analysis. C. Neumann measured XPS spectra. T. Lehnert made in deep HRTEM measurements. F. Börrnert scanned samples for quality for HRTEM. Y. Wang conducted AFM experiments. U. Kaiser interpreted HRTEM measurements. A. Turchanin analyzed and interpreted XPS spectra. S. Eigler wrote manuscript and supervised overall research.</p> <p>The manuscript was mainly written by Y. Hu with assistance from Prof. Dr. S. Eigler, Prof. Dr. U. Kaiser, Prof. Dr. A. Turchanin, Dr. C. Neumann, and Dr. T. Lehnert.</p>
Estimated own contribution	~65 %

5.2 Polarity, Intramolecular Charge Transfer, and Hydrogen Bond Co-Mediated Solvent Effects on the Optical Properties of Graphene Quantum Dots

Authors	Y. Hu, C. Neumann, L. Scholtz, A. Turchanin, U. Resch-Genger, S. Eigler
Journal	<i>Nano Research</i>
Links	https://www.sciopen.com/article/10.1007/s12274-022-4752-1?issn=1998-0124 https://doi.org/10.1007/s12274-022-4752-1
Detailed scientific contribution	<p>The concept of this manuscript was elaborated by Y. Hu and Prof. Dr. S. Eigler.</p> <p>Y. Hu conducted the synthesis of samples, record of UV/Vis absorption and fluorescence spectra of samples. Y. Hu also measured the fluorescence lifetime and quantum yields of samples and wrote manuscript. C. Neumann measured XPS spectra. A. Turchanin analyzed and interpreted XPS spectra. L. Scholtz and U. Resch-Genger helped recording and analysing the spectroscopic data. S. Eigler wrote manuscript and supervised overall research.</p> <p>The manuscript was mainly written by Y. Hu with assistance from Prof. Dr. S. Eigler, Dr. U. Resch-Genger, Prof. Dr. A. Turchanin, Dr. C. Neumann.</p>
Estimated own contribution	~70 %

6 Minor Contributions

6.1 Influence of SiO₂ or h-BN Substrate on the Room Temperature Electronic Transport in Chemically Derived Single Layer Graphene

Authors	Z. Wang, Q. Yao, Y. Hu, C. Li, M. Hußmann, B. Weintrub, J. N. Kirchhof, K. Bolotin, T. Taniguchi, K. Watanabe, S. Eigler
Journal	<i>RSC Adv.</i> 2019 , <i>9</i> , 38011-38016
DOI	10.1039/C9RA09197A
Links	http://dx.doi.org/10.1039/C9RA09197A https://pubs.rsc.org/en/content/articlepdf/2019/ra/c9ra09197a
	The concept of this manuscript was elaborated by Z. Wang and Prof. Dr. S. Eigler.
Detailed scientific contribution	The h-BN/reduced-oxoG heterostructure was prepared by Y. Hu. The AFM and Raman measurements were done by Y. Hu. The revision of the manuscript was assisted by Y. Hu.
Estimated own contribution	~35 %

Cite this: *RSC Adv.*, 2019, 9, 38011

Influence of SiO₂ or h-BN substrate on the room-temperature electronic transport in chemically derived single layer graphene†

Zhenping Wang,^a Qirong Yao,^b Yalei Hu,^a Chuan Li,^b Marleen Hußmann,^a Ben Weintrub,^c Jan N. Kirchhof,^c Kirill Bolotin,^c Takashi Taniguchi,^d Kenji Watanabe^{id} and Siegfried Eigler^{id}*^a

Received 6th November 2019
Accepted 12th November 2019

DOI: 10.1039/c9ra09197a

rsc.li/rsc-advances

The substrate effect on the electronic transport of graphene with a density of defects of about 0.5% (^{0.5%}G) is studied. Devices composed of monolayer ^{0.5%}G, partially deposited on SiO₂ and h-BN were used for transport measurements. We find that the ^{0.5%}G on h-BN exhibits ambipolar transfer behaviours under ambient conditions, in comparison to unipolar p-type characters on SiO₂ for the same flake. While intrinsic defects in graphene cause scattering, the use of h-BN as a substrate reduces p-doping.

Wet-chemically prepared graphene from graphite can be stabilized in solution by covalently bound oxo-groups using established oxidation protocols.^{1–3} In general, the materials obtained are termed graphene oxide (GO). However, the chemical structure varies and the carbon lattice may even be amorphous due to the evolution of CO₂ during synthesis.⁴ Thus, in this study we use oxo-functionalized graphene (oxo-G), a type of GO with a more defined structure, as proven in our previous work.³ The oxygen-containing groups on the graphene basal plane and rims of flakes and holes make GO a p-type semiconductor with a typical resistance of 10¹⁰–10¹³ Ω sq^{−1}^{5,6} and a band gap of about 2.2 eV.^{7,8} The reductive defunctionalization of GO leads to a certain type of graphene (G), often named reduced GO (r-GO).^{4,9} Removal of oxo-groups from the surface can be achieved by chemical reduction,^{9,10} electrochemical methods,^{11,12} electron beam treatment¹³ and was observed *in situ* by transmission electron microscopy.¹³ Thermal processing of GO instead leads to a disproportionation reaction forming carbon with additional vacancy defects and CO₂.¹⁴ In general, the reduction of GO turns r-GO from a semi-conductive material to a semi-metal. Mobility values were determined in field effect transistor (FET) devices.^{15,16} Generally, the quality of graphene strongly depends on the integrity of the hexagonal carbon lattice. Thus, mobility

values of 10^{−3} and up to 10³ cm² V^{−1} s^{−1} were reported,^{3,17,18} with the resistance fluctuating between 10³ and 10⁶ Ω sq^{−1}.^{19–21} We reported on the highest mobility values of chemically reduced oxo-G (with about 0.02% of lattice defects) of 1000 cm² V^{−1} s^{−1},³ determined by Hall-bar measurements at 1.6 K.

Hexagonal boron nitride (h-BN) has been proved to be an excellent substrate for matching graphene-based materials owing to its atomic flatness, chemical inertness and electronic insulation due to a bandgap of ~5.5 eV.²² Up to now, most studies with graphene deposited on h-BN were restricted to measurements with virtually defect-free graphene.²³ To the best of the authors knowledge, no studies reported transport measurements based on single layers of GO or oxo-G on h-BN substrates. No studies are reported with graphene derived from GO or oxo-G on single-layer level. Recently, we found that chemical reactions can be selectively conducted close to the rims of defects.²⁴ However, before functionalized devices can be studied, the lack of knowledge on the ambient environment device performances of graphene with defects and the influence of substrates must be addressed. Therefore, we fabricated the devices composed of ^{0.5%}G, partially deposited on SiO₂ (SiO₂/^{0.5%}G) and h-BN (h-BN/^{0.5%}G) (Fig. 1). Areas of the same flake on both materials are used to ensure reliable measurements and to prove that the results stem from the influence of the substrate rather than from the difference between devices. Thereby, the ^{0.5%}G exhibits an I_D/I_G ratio of about 3–4, corresponding to 0.5% of defects, according to the model introduced by Lucchese and Cançado.^{25–28} Our results demonstrate that the h-BN layer is responsible for a downshift of the Dirac point and a more narrow hysteresis, resulting in ambipolar transfer behaviours in h-BN/^{0.5%}G.

^aInstitute of Chemistry and Biochemistry, Freie Universität Berlin, Takustraße 3, 14195 Berlin, Germany. E-mail: siegfried.eigler@fu-berlin.de

^bPhysics of Interfaces and Nanomaterials, MESA+ Institute for Nanotechnology, University of Twente, P.O. Box 217, 7500 AE Enschede, The Netherlands

^cInstitute of Physics, Freie Universität Berlin, Arnimallee 14, 14195 Berlin, Germany

^dAdvanced Materials Laboratory, National Institute for Materials Science, 1-1 Namiki, Tsukuba 305-0044, Japan

† Electronic supplementary information (ESI) available. See DOI: 10.1039/c9ra09197a



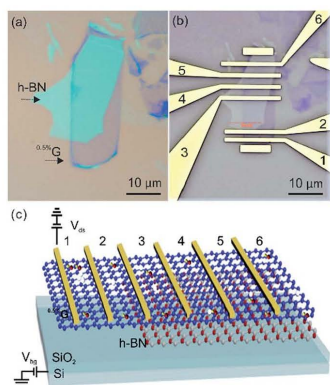


Fig. 1 (a) Optical image of the fabricated h-BN/ $^{0.5\%}$ G heterostructure on SiO₂. (b) The h-BN/ $^{0.5\%}$ G heterostructure device. Electrodes 1 and 2 define the SiO₂/ $^{0.5\%}$ G FET device. Electrodes 1 and 3 define the $^{0.5\%}$ G on overlapped SiO₂/h-BN hetero-substrate device. Electrodes 3 and 4 define the h-BN/ $^{0.5\%}$ G FET device. Distance between the electrodes 1–2 and 3–4 is 1.5 μ m and 3 μ m, respectively. (c) 3D illustration of the h-BN/ $^{0.5\%}$ G transistor device.

Results and discussion

To gain structural information of $^{0.5\%}$ G, flakes of $^{0.5\%}$ G were deposited on HOPG surface and examined by scanning tunnelling microscopy (STM) under an ultra-high vacuum (10^{-10} mbar). The average height of a single $^{0.5\%}$ G flake was determined as 0.9 nm (Fig. 2a). At higher resolution, two different morphologies are detected in the $^{0.5\%}$ G flake, as depicted in Fig. 2b. The atomically resolved structure is assigned for the dark region while the resolution fades away in the bright region. The diffraction spots marked in dashed red indicate the hexagonal lattice of graphene in the dark regions, shown in Fig. 2c. The bright regions are caused by the oxygen-containing groups attached to the carbon lattice, which breaks the lattice periodicity of graphene and subsequently lead to no apparent diffraction feature in the reciprocal space (Fig. 2d).

Atomic scale electronic properties of $^{0.5\%}$ G were explored using scanning tunnelling spectroscopy (STS). Fig. 2e displays the $I(V)$ spectrum of the $^{0.5\%}$ G surface. Compared to the tunnelling current at the dark region, there exists an apparent suppression of current at the bright region owing to a lower conductivity in the distorted graphene lattices. For the averaged $I(V)$ spectra of the whole area, the metallic behaviour of the

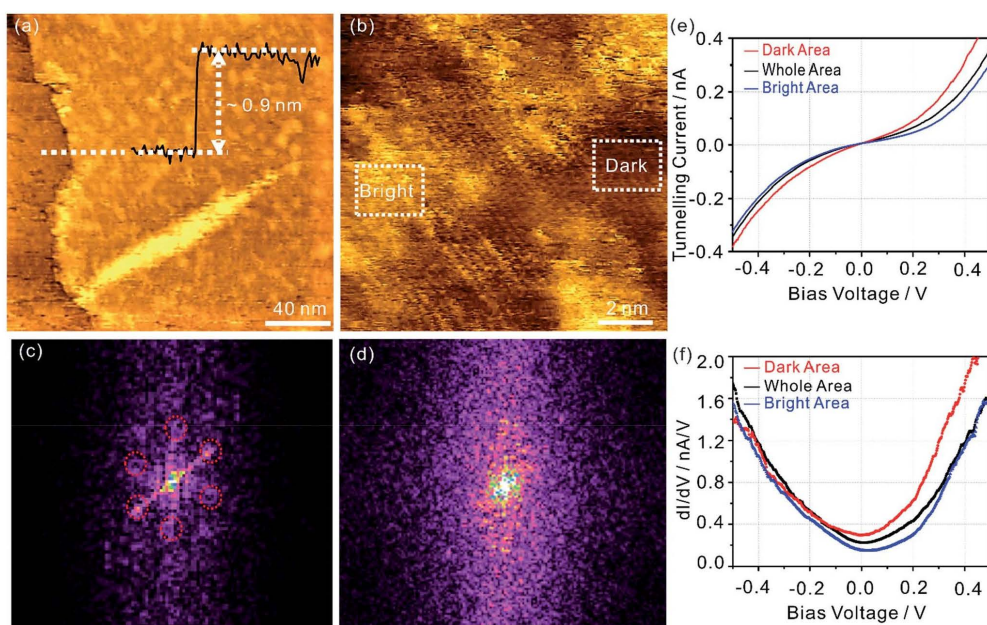


Fig. 2 (a) Overview STM topographic image of the $^{0.5\%}$ G on highly oriented pyrolytic graphite (HOPG) substrate (200 nm \times 200 nm; $I_t = 0.6$ nA, $V_s = -0.5$ V). The inset is the height profile of the $^{0.5\%}$ G flake. (b) STM topographic image of the $^{0.5\%}$ G (12 nm \times 12 nm; $I_t = 0.4$ nA, $V_s = -0.3$ V). (c) and (d) Fast Fourier transform (FFT) images of the dark region and bright region in (b), respectively. (e) and (f) $I(V)$ spectrum (averaged over >100 single spectra) and corresponding dI/dV curves recorded at the dark area (red curve), bright area (blue curve) and whole area (black curve), respectively.



$^{0.5\%}\text{G}$ flake is found. This phenomenon is also confirmed by the differential conductivity (dI/dV) curves in Fig. 2f. The Dirac point is determined from the minimum value in dI/dV curves. The Dirac point in dark region is located at 0.0 V, suggesting low impurity-related doping level. In contrast, the bright regions exhibit a positive shift of the Dirac point of about 50 mV, likely due to the presence of oxygen groups. For the entire scanned areas, the $^{0.5\%}\text{G}$ flake exhibits a p-type electronic doping feature with the average Dirac point at about 20 mV.

For the fabrication of the heterostructure of $\text{h-BN}/^{0.5\%}\text{G}$ or $\text{SiO}_2/^{0.5\%}\text{G}$, flakes of oxo-G were first deposited on SiO_2 substrate by Langmuir–Blodgett technique,²⁹ as shown in Fig. 3a. Then $^{0.5\%}\text{G}$ flakes were prepared by reduction using vapor of HI/TFA (in inset of Fig. 3b).³⁰ The h-BN flakes used in this study were exfoliated from h-BN single crystals.³¹ Next, the heterostructures of $\text{h-BN}/^{0.5\%}\text{G}$ or $\text{SiO}_2/^{0.5\%}\text{G}$ were prepared by a dry transfer technique.³²

Fig. 4a shows an AFM image of a $\text{h-BN}/^{0.5\%}\text{G}$ heterostructure, which consists of SiO_2 substrate with multilayer h-BN flake and a monolayer $^{0.5\%}\text{G}$ flake ($\sim 25 \times 10 \mu\text{m}^2$) partially covering the h-BN. The AFM image in Fig. 4b, obtained within the marked area in Fig. 4a, revealed that the transfer process induced wrinkles and folds in $^{0.5\%}\text{G}$. The height profile of the single $^{0.5\%}\text{G}$ flake on SiO_2 is shown in Fig. 4c (compare Fig. S1†) and depicts a thickness of about 2 nm. This height is much thicker than 0.9 nm measured by STM for similar monolayer $^{0.5\%}\text{G}$ on HOPG.

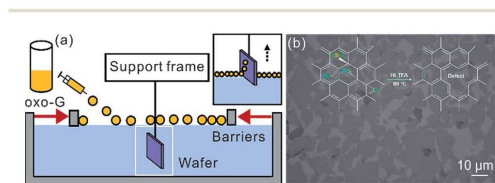


Fig. 3 (a) Schematic illustration of Langmuir–Blodgett assembly of oxo-G single layers. (b) Optical image of collected $^{0.5\%}\text{G}$ flakes on a silicon wafer with 300 nm SiO_2 , obtained after hydroiodic acid (HI) and trifluoroacetic acid (TFA) reduction as shown in the inset.

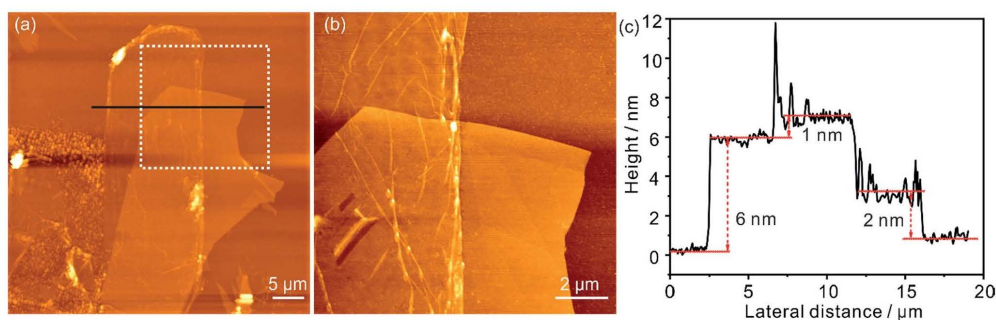


Fig. 4 (a) AFM image of a $\text{h-BN}/^{0.5\%}\text{G}$ heterostructure on a Si/SiO_2 substrate. (b) AFM image obtained from the area within the white square in (a). (c) Height profiles of $^{0.5\%}\text{G}$ on SiO_2 , $^{0.5\%}\text{G}$ on h-BN and h-BN layer, which are corresponding to the black lines in (b).

A major plausible reason is that *e.g.* water molecules are inevitably adsorbed on the hydrophilic SiO_2 surface (treated by O_2 plasma) leading to an approximately nanometer-thick hydrogen-bonded water layer and cleaved oxo-groups captured between SiO_2 and $^{0.5\%}\text{G}$.³³ In contrast, although small amounts of polymer residues are likely trapped between h-BN and $^{0.5\%}\text{G}$, the measured thickness of the same $^{0.5\%}\text{G}$ flake on h-BN is

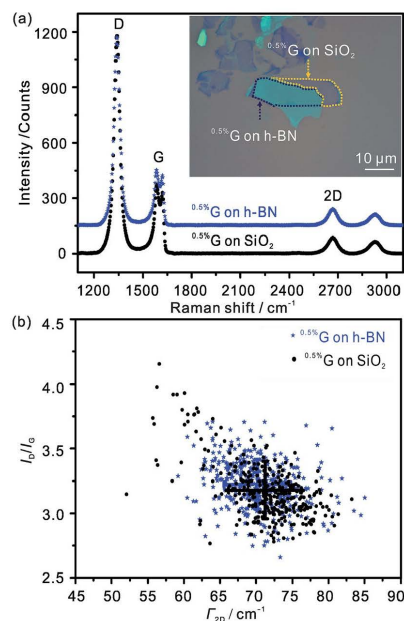


Fig. 5 Statistical Raman microscopy measured with each pixel corresponding to an area of $\sim 0.7 \times 0.7 \mu\text{m}^2$ at 532 nm laser excitation wavelength. The laser power is below 1 mW to avoid heating induced by laser. (a) Average Raman spectra of $^{0.5\%}\text{G}$ on SiO_2 and h-BN. (b) I_D/I_G ratio vs. I_{2D} .



Table 1 Summary of electrical performances for the ^{0.5%}G on h-BN, overlapped SiO₂-h-BN hetero-substrate and SiO₂

	Resistance/kΩ	Mobility/cm ² V ⁻¹ s ⁻¹	Dirac point voltage/V	Channel length/μm
h-BN/ ^{0.5%} G	34.4	5.6	~20	3
SiO ₂ / ^{0.5%} G	15.6	11.6	>43	1.5
SiO ₂ / ^{0.5%} G ^a	5.0	14.2	>50	3
SiO ₂ / ^{0.5%} G ^b	5.7	14.5	>50	3
SiO ₂ / ^{0.5%} G ^c	6.8	7.4	>60	2
h-BN/ ^{0.5%} G ^d	18.7	5.3	~37	2
h-BN/ ^{0.5%} G ^e	32.5	8.5	~22	1.5

^a Reference device of ^{0.5%}G on SiO₂, see Fig. S3 (channel: 1–2). ^b Reference device of ^{0.5%}G on SiO₂, see Fig. S3 (channel: 2–3). ^c Reference device of ^{0.5%}G on SiO₂, see Fig. S4 (channel: 1–2). ^d Reference device of ^{0.5%}G on h-BN, see Fig. S4 (channel: 3–4). ^e Reference device of ^{0.5%}G on h-BN, see Fig. S5 (channel: 1–2).

~1 nm as shown in Fig. 4c, which is almost the same result as the thickness determined by STM. The ^{0.5%}G flake on ~6 nm thick h-BN (Fig. 4c) possesses a lower roughness (~0.5 nm) than on SiO₂ (~1 nm). Therefore, h-BN, as a passivation layer, can not only negate the influence of trapped water on graphene, but also improves accuracy in the AFM thickness measurements of monolayer 2D flakes.

Average Raman spectra of the ^{0.5%}G supported by SiO₂ and h-BN, respectively, are shown in Fig. 5a. The primary peaks are the D peak near 1340 cm⁻¹, the G peak near 1555–1557 cm⁻¹ and the 2D peak near 2667 cm⁻¹. The D peak of ^{0.5%}G on each interface is mainly activated by defects in the carbon skeletons. The G and 2D peaks closely relate to the quality of graphene. The almost unchanged positions of the three peaks indicate that wrinkles and residual polymers induced during the transfer processes do not produce obvious doping effect on the single layer ^{0.5%}G. We use scatter plots of I_D/I_G versus I_{2D} to further confirm the quality of the ^{0.5%}G in Fig. 5b. For the ^{0.5%}G on h-BN, the I_D/I_G ratio is about 3.3, within the standard deviation of the I_D/I_G ratio of 3.1 determined on SiO₂. Based on the model introduced by Lucchese and Cançado *et al.*,^{25,26} the density of lattice defects is related to 0.5% for the devices on h-BN and SiO₂. This density of defects relates to the average distance between defects of around 3 nm. The related defect density (n_D) is 4.0×10^{12} cm⁻² on h-BN and SiO₂, respectively, calculated from the equation n_D (cm⁻²) = $10^{14}/(\pi L_D^2)$.²⁵ The I_{2D} of the Raman 2D band is sensitive to the presence of defects. For the monolayer ^{0.5%}G on h-BN, only a slightly smaller I_{2D} of ~70 cm⁻¹ is observed than on SiO₂ (~72 cm⁻¹). The same monolayer ^{0.5%}G, partially deposited on SiO₂ and h-BN, presents almost the same I_{2D} . Therefore, the quality of the investigated flake is the same on SiO₂ and h-BN, respectively.

Reference experiments to determine the contact resistance were conducted using four-probe measurements. The surface resistance is determined to roughly 21 kΩ in four-probe configuration and 23.5 kΩ in two-probe configuration (Fig. S2†). Thus, further investigations were conducted in two-probe configuration under ambient conditions. For our transport measurements, we prepared one device with monolayer ^{0.5%}G on SiO₂ substrate (Fig. S3†), two devices with the same monolayer ^{0.5%}G flake that are in part on SiO₂ and on h-BN

(Fig. 1 and S4†) and one device with monolayer ^{0.5%}G on h-BN substrate (Fig. S5†). The patterning of the electrodes was achieved by standard electron beam lithography processing and subsequent deposition of 5 nm Cr/70 nm Au by thermal evaporation. The electrical performance of the ^{0.5%}G flake on h-BN and SiO₂, respectively, is summarised in Table 1. The resistance of ^{0.5%}G on h-BN and SiO₂ measured at $V_{bg} = 0$ V ranges

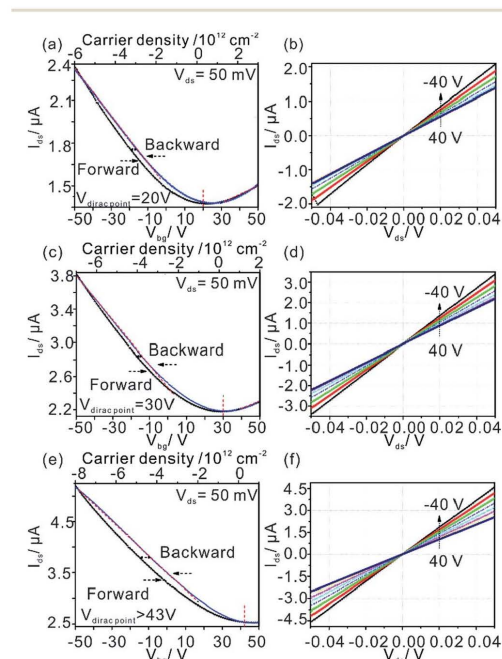


Fig. 6 (a), (c) and (e) Transfer characteristics under ambient conditions for ^{0.5%}G on h-BN, overlapped SiO₂/hBN hetero-substrate and SiO₂ with $V_{ds} = 50$ mV. The gate voltage is swept continuously from -50 to 50 V and back to -50 V. (b), (d) and (f) Related I_{ds} - V_{ds} curves acquired for V_{bg} values from -40 V to 40 V in steps of 10 V.



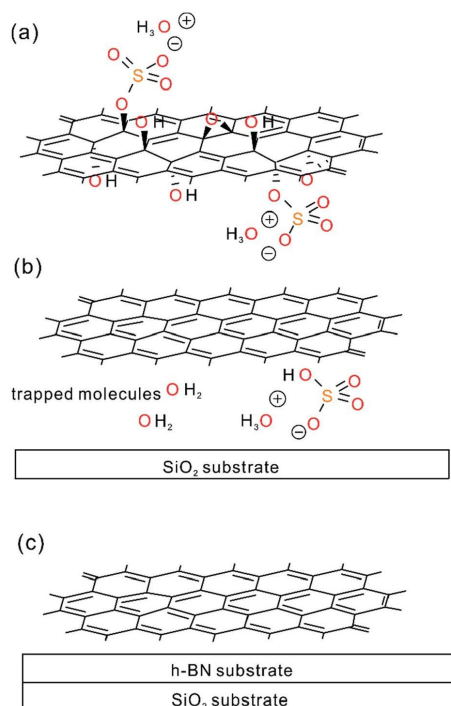


Fig. 7 Proposed model of trapped species upon cleavage of oxo-groups upon reduction and influence of substrate. (a) Chemical sketch of the structure of oxo-G with the graphene lattice decorated by hydroxyl-, epoxy- and organosulfate groups. (b) $^{0.5\%}\text{G}$ prepared by chemical reduction of oxo-G; covalently bound oxo-groups are cleaved and at least partially trapped between $^{0.5\%}\text{G}$ and the SiO_2 substrate. (c) $^{0.5\%}\text{G}$ on h-BN; cleaved oxo-groups may not be trapped between h-BN and $^{0.5\%}\text{G}$ because they are squeezed out.

widely, from 5.0 k Ω to 34.4 k Ω . But the resistances are significant lower compared to $>10^6 \Omega$ reported for similar devices.¹⁷

Transfer curves ($I_{\text{ds}}-V_{\text{ds}}$) of $^{0.5\%}\text{G}$ on h-BN is shown in Fig. 6a. The Dirac points are located at around +20 V. The hysteresis effect of the $^{0.5\%}\text{G}$ on h-BN is observed in ambient environment for sweeping continuously from -50 to 50 V in forward direction and then back to -50 V (backward direction). From the red dashed lines presented in Fig. 6a, a room-temperature hole mobility (μ_{h}) of 5.6 $\text{cm}^2 \text{V}^{-1} \text{s}^{-1}$ is extracted using the equation $\mu = (L/W) \times (1/(C_{\text{ox}}V_{\text{ds}})) \times (dI_{\text{ds}}/dV_{\text{bg}})$,³⁴ where $C_{\text{ox}} = 1.15 \times 10^{-8} \text{ F cm}^{-2}$. As the output curves ($I_{\text{ds}}-V_{\text{ds}}$) exhibit ohmic behaviour (Fig. 6b) we conclude that there is no Schottky contact between $^{0.5\%}\text{G}$ and metal electrodes. For the $^{0.5\%}\text{G}$ deposited on the overlapped SiO_2 -h-BN hetero-substrate (transport measurements performed between electrodes 2 and 4, shown in Fig. 1c), we observe only p-type character of the $I_{\text{ds}}-V_{\text{ds}}$ curves with the Dirac point shifted to about +30 V (Fig. 6c).

In contrast to $^{0.5\%}\text{G}$ on h-BN and overlapped SiO_2 -h-BN hetero-structure, the $^{0.5\%}\text{G}$ on SiO_2 exhibits unipolar p-type character (Fig. 6e). The point of the minimum conductivity in the $I_{\text{ds}}-V_{\text{bg}}$ curve is not observed and the Dirac point moves to higher positive voltage ($>43 \text{ V}$). Obviously, electrical transport of the $^{0.5\%}\text{G}$ on SiO_2 is completely governed by holes with hole mobility μ_{h} estimated to about 11.6 $\text{cm}^2 \text{V}^{-1} \text{s}^{-1}$. In addition, the $I_{\text{ds}}-V_{\text{bg}}$ curves exhibit an increase of hysteresis in $\text{SiO}_2/^{0.5\%}\text{G}$ device with a shift of V_{bg} ($\Delta V_{\text{bg}} \approx 7.3 \text{ V}$) between the forward and reverse sweeps, compared to the h-BN/ $^{0.5\%}\text{G}$ device with $\Delta V_{\text{bg}} \approx 2.6 \text{ V}$. Substrate change from h-BN to SiO_2 induces trapped holes with density higher than $1.6 \times 10^{12} \text{ cm}^{-2}$ using $\Delta n_{\text{t}} = \Delta V_{\text{Dirac point}} (C_{\text{ox}}/q)$,² where q is the elementary charge, $\Delta V_{\text{Dirac point}} > 43-20 = 23 \text{ V}$. In general, a high density of charge traps can cause hysteresis and lead to reduced mobility of graphene samples.³⁵ However, as summarized in Table 1, mobility values on SiO_2 are higher and the resistance is lower than on h-BN. The main reason for that contradictory finding is that for $^{0.5\%}\text{G}$ defects are the dominant scatterers reducing the carrier mobility. This is consistent with Raman results of Fig. 5b. As further reference experiments we conducted transport measurements of defective graphene, here $^{0.8\%}\text{G}$ on SiO_2 . As shown in Fig. S6,† due to the higher density of defects the hole mobility values are 0.6 $\text{cm}^2 \text{V}^{-1} \text{s}^{-1}$ in ambient and 0.9 $\text{cm}^2 \text{V}^{-1} \text{s}^{-1}$ in vacuum. However, the Dirac point shifts only from 60 V in ambient to 30 V in vacuum. Those results are in agreement with the STS measurements, which indicate p-doping of $^{0.5\%}\text{G}$ in vacuum. It could however be expected that oxo-groups with -I and -M effects,^{2,3} decorating the rims of vacancy defects, may be responsible for trapping hole carriers. However, the experimental results, such as transport and AFM measurements, give evidence that p-doping is strongly induced by the SiO_2 substrate and cleaved oxo-species, such as water or organosulfate, which are trapped between SiO_2 and $^{0.5\%}\text{G}$. Therefore, based on the AFM height determination on SiO_2 , the knowledge about the chemical structure and the reduction mechanism of oxo-G to $^{0.5\%}\text{G}$ we propose that molecules, such as water or hydrogensulfate stemming from oxo-G (Fig. 7a) are trapped between the SiO_2 substrate surface and $^{0.5\%}\text{G}$ (Fig. 7b). In comparison, h-BN is affected by the local polarity of h-BN/ $^{0.5\%}\text{G}$. As a result, spurious dopant molecules may get squeezed out (Fig. 7c), as is also supported by the measured height and roughness results determined by AFM.

Conclusions

$^{0.5\%}\text{G}$ is a p-doped material and defects determine the scattering of charge carriers. Using h-BN as substrate leads to less trapped molecules, which are responsible for p-doping. In this regard, most likely hydrogen-bonded water and other cleaved oxo-species are captured between SiO_2 and $^{0.5\%}\text{G}$ causing p-doping, as a consequence of chemical reduction of oxo-G. The ambipolar behaviour with $V_{\text{Dirac point}}$ of +20 V was therefore observed for the h-BN/ $^{0.5\%}\text{G}$ structure while unipolar p-type response was shown for the same $^{0.5\%}\text{G}$ flake on SiO_2 . Transfer characteristics show a reduction of hysteresis in the h-BN/ $^{0.5\%}\text{G}$. The mobility of the $\text{SiO}_2/^{0.5\%}\text{G}$ is determined to 7.4-



14.5 cm² V⁻¹ s⁻¹ and for h-BN/^{0.5%}G to 5.6–8.5 cm² V⁻¹ s⁻¹ at ambient conditions.

Conflicts of interest

There are no conflicts to declare.

Acknowledgements

This research is supported by the China Scholarship Council (CSC), the Deutsche Forschungsgemeinschaft (DFG, German Research Foundation), project number 392444269 and 249559513, and ERC Grant No. 639739.

References

- 1 D. C. Marcano, D. V. Kosynkin, J. M. Berlin, A. Sinitskii, Z. Sun, A. Slesarev, L. B. Alemany, W. Lu and J. M. Tour, *ACS Nano*, 2010, **4**, 4806–4814.
- 2 Y. Zhu, S. Murali, W. Cai, X. Li, J. W. Suk, J. R. Potts and R. S. Ruoff, *Adv. Mater.*, 2010, **22**, 3906–3924.
- 3 S. Eigler, M. Enzelberger-Heim, S. Grimm, P. Hofmann, W. Kroener, A. Geworski, C. Dotzer, M. Rockert, J. Xiao, C. Papp, O. Lytken, H. P. Steinrück, P. Müller and A. Hirsch, *Adv. Mater.*, 2013, **25**, 3583–3587.
- 4 D. R. Dreyer, S. Park, C. W. Bielawski and R. S. Ruoff, *Chem. Soc. Rev.*, 2010, **39**, 228–240.
- 5 H.-J. Shin, K. K. Kim, A. Benayad, S.-M. Yoon, H. K. Park, I.-S. Jung, M. H. Jin, H.-K. Jeong, J. M. Kim, J.-Y. Choi and Y. H. Lee, *Adv. Funct. Mater.*, 2009, **19**, 1987–1992.
- 6 O. M. Slobodian, P. M. Lytvyn, A. S. Nikolenko, V. M. Naseka, O. Y. Khyzhun, A. V. Vasin, S. V. Sevostianov and A. N. Nazarov, *Nanoscale Res. Lett.*, 2018, **13**, 139.
- 7 H. F. Liang, C. T. G. Smith, C. A. Mills and S. R. P. Silva, *J. Mater. Chem. C*, 2015, **3**, 12484–12491.
- 8 M. A. Velasco-Soto, S. A. Pérez-García, J. Alvarez-Quintana, Y. Cao, L. Nyborg and L. Licea-Jiménez, *Carbon*, 2015, **93**, 967–973.
- 9 S. Pei and H.-M. Cheng, *Carbon*, 2012, **50**, 3210–3228.
- 10 H. L. Guo, X. F. Wang, Q. Y. Qian, F. B. Wang and X. H. Xia, *ACS Nano*, 2009, **3**, 2653–2659.
- 11 K. W. Silverstein, C. E. Halbig, J. S. Mehta, A. Sharma, S. Eigler and J. M. Mativetsky, *Nanoscale*, 2019, **11**, 3112–3116.
- 12 S. Yang, M. R. Lohe, K. Müllen and X. L. Feng, *Adv. Mater.*, 2016, **28**, 6213–6221.
- 13 B. Butz, C. Dolle, C. E. Halbig, E. Spiecker and S. Eigler, *Angew. Chem., Int. Ed.*, 2016, **55**, 15771–15774.
- 14 F. Grote, C. Gruber, F. Börrnert, U. Kaiser and S. Eigler, *Angew. Chem., Int. Ed.*, 2017, **56**, 9222–9225.
- 15 B. Radisavljevic, A. Radenovic, J. Brivio, V. Giacometti and A. Kis, *Nat. Nanotechnol.*, 2011, **6**, 147–150.
- 16 K. Kim, J. Y. Choi, T. Kim, S. H. Cho and H. J. Chung, *Nature*, 2011, **479**, 338–344.
- 17 C. Gómez-Navarro, R. T. Weitz, A. M. Bittner, M. Scolari, A. Mews, M. Burghard and K. Kern, *Nano Lett.*, 2007, **7**, 3499–3503.
- 18 C. Y. Su, Y. P. Xu, W. J. Zhang, J. W. Zhao, A. P. Liu, X. H. Tang, C. H. Tsai, Y. Z. Huang and L. J. Li, *ACS Nano*, 2010, **4**, 5285–5292.
- 19 J. K. Wassei and R. B. Kaner, *Mater. Today*, 2010, **13**, 52–59.
- 20 Y. L. Wang, Y. A. Chen, S. D. Lacey, L. S. Xu, H. Xie, T. Li, V. A. Danner and L. B. Hu, *Mater. Today*, 2018, **21**, 186–192.
- 21 R. Negishi, M. Akabori, T. Ito, Y. Watanabe and Y. Kobayashi, *Sci. Rep.*, 2016, **6**, 28936.
- 22 G. Cassabois, P. Valvin and B. Gil, *Nat. Photonics*, 2016, **10**, 262.
- 23 C. R. Dean, A. F. Young, I. Meric, C. Lee, L. Wang, S. Sorgenfrei, K. Watanabe, T. Taniguchi, P. Kim, K. L. Shepard and J. Hone, *Nat. Nanotechnol.*, 2010, **5**, 722–726.
- 24 C. E. Halbig, R. Lasch, J. Krull, A. S. Pirzer, Z. P. Wang, J. N. Kirchhof, K. I. Bolotin, M. R. Heinrich and S. Eigler, *Angew. Chem., Int. Ed.*, 2019, **58**, 3599–3603.
- 25 L. G. Cançado, A. Jorio, E. H. Ferreira, F. Stavale, C. A. Achete, R. B. Capaz, M. V. Moutinho, A. Lombardo, T. S. Kulmala and A. C. Ferrari, *Nano Lett.*, 2011, **11**, 3190–3196.
- 26 M. M. Lucchese, F. Stavale, E. H. M. Ferreira, C. Vilani, M. V. O. Moutinho, R. B. Capaz, C. A. Achete and A. Jorio, *Carbon*, 2010, **48**, 1592–1597.
- 27 P. Vecera, S. Eigler, M. Kolesnik-Gray, V. Krstic, A. Vierck, J. Maultzsch, R. A. Schäfer, F. Hauke and A. Hirsch, *Sci. Rep.*, 2017, **7**, 45165.
- 28 A. Naumov, F. Grote, M. Overgaard, A. Roth, C. E. Halbig, K. Nørgaard, D. M. Guldi and S. Eigler, *J. Am. Chem. Soc.*, 2016, **138**, 11445–11448.
- 29 L. J. Cote, F. Kim and J. Huang, *J. Am. Chem. Soc.*, 2009, **131**, 1043–1049.
- 30 S. Eigler, S. Grimm, M. Enzelberger-Heim, P. Müller and A. Hirsch, *Chem. Commun.*, 2013, **49**, 7391–7393.
- 31 R. V. Noorden, *Nature*, 2012, **483**, S32–S33.
- 32 X. Ma, Q. Liu, D. Xu, Y. Zhu, S. Kim, Y. Cui, L. Zhong and M. Liu, *Nano Lett.*, 2017, **17**, 6961–6967.
- 33 M. J. Lee, J. S. Choi, J. S. Kim, I. S. Byun, D. H. Lee, S. Ryu, C. Lee and B. H. Park, *Nano Res.*, 2012, **5**, 710–717.
- 34 F. Schwierz, *Nat. Nanotechnol.*, 2010, **5**, 487–496.
- 35 A. D. Bartolomeo, F. Giubileo, F. Romeo, P. Sabatino, G. Carapella, L. Lemmo, T. Schroeder and G. Lupina, *Nanotechnology*, 2015, **26**, 475202–475210.



Supporting Information

Influence of SiO₂ or h-BN substrate on the room-temperature electronic transport in chemically derived single layer graphene

Zhenping Wang,^a Qirong Yao,^b Yalei Hu,^a Chuan Li,^b Marleen Hußmann,^a Ben Weintrub,^c Jan Kirchhof,^c Kirill Bolotin,^c Takashi Taniguchi^d, Kenji Watanabe^d and Siegfried Eigler^{a*}

- a. Institute of Chemistry and Biochemistry, Freie Universität Berlin, Takustraße 3, 14195 Berlin, Germany
- b. Physics of Interfaces and Nanomaterials, MESA+ Institute for Nanotechnology, University of Twente, P.O. Box 217, 7500 AE Enschede, The Netherlands.
- c. Institute of Physics, Freie Universität Berlin, Arnimallee 14, 14195 Berlin, Germany.
- d. Advanced Materials Laboratory, National Institute for Materials Science, 1-1 Namiki, Tsukuba 305-0044, Japan.
E-mail: siegfried.eigler@fu-berlin.de.

Experimental Section

1. Synthesis of oxo-G

Oxo-G was prepared by the optimized oxidation of graphite at low temperature (< 4 °C), using potassium permanganate as oxidant in sulfuric acid, as reported before by our group.¹

2. Langmuir-Blodgett films of oxo-G

Flakes of oxo-G were deposited onto the Si/SiO₂ substrate by Langmuir–Blodgett technique² (LB, Kibron μ trough, 3 mN m⁻¹ with the surface tension of water as reference value of 72.8 mN m⁻¹). Reduction was performed by vapor of hydriodic acid and trifluoroacetic acid (1/1 mixture by volume) at 80 °C (10 min). Subsequently, the surface of graphene was cleaned with doubly distilled water (Carl Roth) to remove iodine species, which are adsorbed on ^{0.5%}G flakes.

3. Fabrication of h-BN/^{0.5%}G heterostructures device

In order to make h-BN/^{0.5%}G heterostructures, a h-BN flake (obtained from Taniguchi group, Japan) was mechanically exfoliated onto the Si/SiO₂ substrate by scotch tape method.³ The ^{0.5%}G flake was transferred onto Si/SiO₂/h-BN surfaces with Polydimethylsiloxane (PDMS, Gel-pack) as a carrier.⁴ Then, the h-BN/^{0.5%}G heterostructure with the same monolayer ^{0.5%}G flake partially covered on SiO₂ and h-BN surfaces was

finished. Patterning of the electrode structure was achieved by standard electron beam lithography processing (Raith PIONEER TWO). The 5/70 nm Cr/Au electrodes were deposited by thermal evaporation (Kurt J. Lesker NANO 36).

4. Measurements

Optical imaging was performed using a Nikon LV100ND. Scanning tunnelling microscopy (STM) and Scanning tunnelling spectroscopy (STS) were performed with an ultra-high vacuum ($< 10^{-10}$ mbar) STM (Omicron-STM1). AFM characterization was performed using a JPK Nanowizard 4 atomic force microscope in tapping mode at room temperature. Statistical Raman spectroscopy was recorded using a confocal Raman microscope (Horiba Explorer, 532 nm excitation wavelength). Electrical measurements were carried out at ambient conditions using a probe station with micromanipulated probes and two source-measurement units (Keithley 2450). In addition, comparing experiments were carried out at vacuum (HI-CUBE) using Lakeshore probe station.

Results

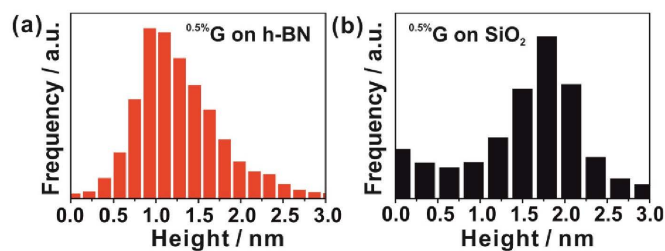


Fig. S1. (a) and (b) Histogram of the height distribution measured by AFM for the $^{0.5\%}\text{G}$ on h-BN and SiO_2 .

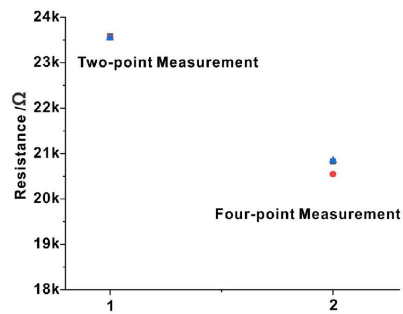


Fig. S2. Measurements of resistance of monolayer $^{0.5\%}\text{G}$ in two-point and four-point configuration, respectively.

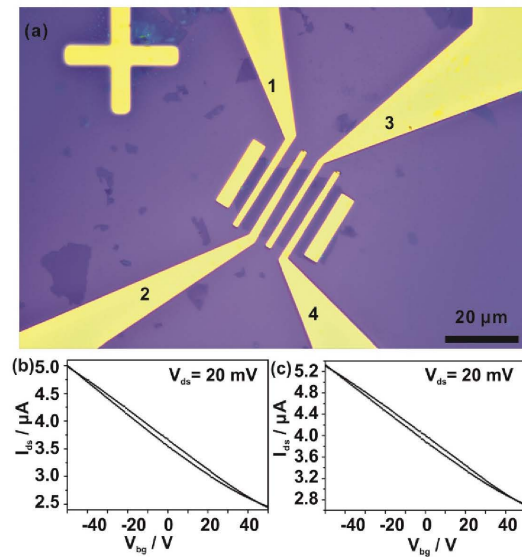


Fig. S3. (a) Optical image of the fabricated monolayer $^{0.5\%}\text{G}$ device with back-gate. (b) Electrodes 1 and 2 were measured for transfer characteristics for the $^{0.5\%}\text{G}$ on SiO_2 . Channel length and width between 1 and 2 is $3\ \mu\text{m}$ and $24\ \mu\text{m}$, respectively. (c) Electrodes 2 and 3 were measured for transfer characteristics for the $^{0.5\%}\text{G}$ on SiO_2 . Channel length and width between 2 and 3 is $3\ \mu\text{m}$ and $24\ \mu\text{m}$, respectively.

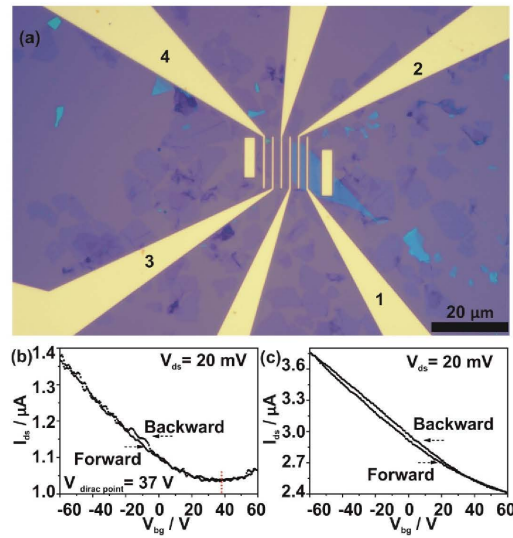


Fig. S4. (a) Optical image of the fabricated h-BN/^{0.5%}G and SiO₂/^{0.5%}G heterostructures device with back-gate. (b) Electrodes 1 and 2 were measured for the ^{0.5%}G on h-BN. Channel length and width between 1 and 2 is 2 μm and 15 μm, respectively. Electrodes 3 and 4 are measured for the ^{0.5%}G on SiO₂. Channel length and width between 3 and 4 is 2 μm and 15 μm, respectively.

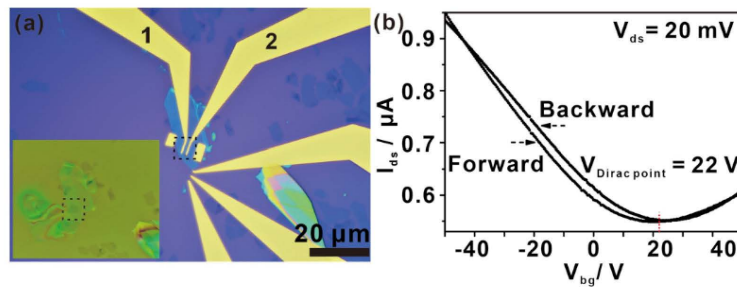


Fig. S5. (a) Optical image of the fabricated h-BN/^{0.5%}G (the ^{0.5%}G is completely deposited onto the h-BN) heterostructures device. Channel length and width is 1.5 μm and 5 μm, respectively. The inset shows that the ^{0.5%}G flake is completely deposited on h-BN, which can fully avoid the effect of SiO₂ substrate on the electrical transport properties of the ^{0.5%}G. (b) Transfer characteristics for the ^{0.5%}G on h-BN.

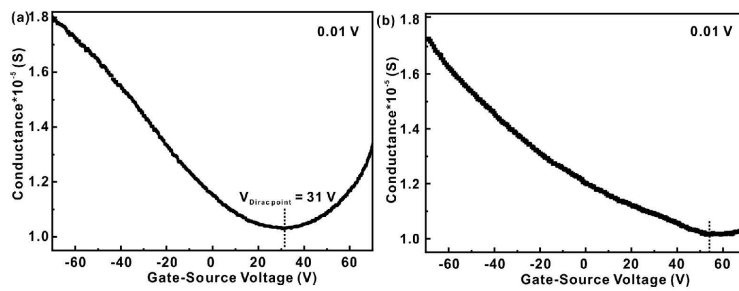


Fig. S6. Transfer curves of the reduced oxo-G with 0.8% defects in vacuum and air by two-probe configuration.

Reference

1. S. Eigler, M. Enzelberger-Heim, S. Grimm, P. Hofmann, W. Kroener, A. Geworski, C. Dotzer, M. Rockert, J. Xiao, C. Papp, O. Lytken, H. P. Steinrück, P. Müller and A. Hirsch, *Adv. Mater.*, 2013, **25**, 3583-3587.
2. L. J. Cote, F. Kim and J. Huang, *J. Am. Chem. Soc.*, 2009, **131**, 1043-1049.
3. R. V. Noorden, *Nature*, 2012, **483**, S32-S33.
4. X. Ma, Q. Liu, D. Xu, Y. Zhu, S. Kim, Y. Cui, L. Zhong and M. Liu, *Nano Lett.*, 2017, **17**, 6961-6967.

6.2 Synthesis of Wet-Chemically Prepared Porous-Graphene Single Layers on Si/SiO₂ Substrate Increasing the Photoluminescence of MoS₂ in Heterostructures

Authors	Y. Wang, C. Neumann, M. Hußmann, Q. Cao, Y. Hu, O. Garrity, P. Kusch, A. Turchanin, S. Eigler
Journal	Adv. Mater. Interfaces 2021 , 8, 2100783
DOI	10.1002/admi.202100783
Links	https://doi.org/10.1002/admi.202100783 https://onlinelibrary.wiley.com/doi/abs/10.1002/admi.202100783
	The concept of this manuscript was elaborated by Y. Wang and Prof. Dr. S. Eigler.
Detailed scientific contribution	Some photoluminescence and Raman measurements were done by Y. Hu. The revision of the manuscript was assisted by Y. Hu.
Estimated own contribution	~10 %

Synthesis of Wet-Chemically Prepared Porous-Graphene Single Layers on Si/SiO₂ Substrate Increasing the Photoluminescence of MoS₂ in Heterostructures

Yiqing Wang, Christof Neumann, Marleen Hußmann, Qing Cao, Yalei Hu, Oisín Garrity, Patryk Kusch, Andrey Turchanin, and Siegfried Eigler*

Wet-chemical generation of pores in graphene is a challenging synthetic task. Although graphene oxide is available in large quantities and chemically diverse, extended lattice defects already present from synthesis hamper the controlled growth of pores. However, membrane, energy, or nanoelectronic applications essentially require uniform pores in applications. Here, oxo-functionalized graphene (oxoG), a type of graphene oxide with a controlled density of vacancy defects, is used as starting material. Pores in graphene are generated from potassium permanganate treated oxoG and heating from room temperature to 400 °C. With etching time, the size of pores increases and pore-diameters of, for example, 100–200 nm in majority become accessible. The experiments are conducted on the single-layer level on Si/SiO₂ wafers. Flakes remain stable on the μm scale and do not fold. The process leads to rims of pores, which are functionalized by carbonyl groups in addition to hydroxyl and carboxyl groups. In addition, it is found that heterostructures with intrinsically n-doped MoS₂ can be fabricated and photoluminescence (PL) measurements reveal a 10-fold increased PL. Thus, graphene with pores is a novel highly temperature-stable electron-accepting 2D material to be integrated into van der Waals heterostructures.

1. Introduction

Graphene with defects, such as pores in the lattice of graphene^[1–3] finds emerging applications for water separation, gas separation and purification, or sensing.^[4–10] The chemical functionalization of graphene can either be accomplished with graphene dispersed in solvents,^[11] or with graphene deposited on surfaces.^[12] Applications based on bulk functionalization target, for example, composite formation, exploiting the mechanical properties of graphene, or electronic properties for energy applications and energy conversion or storage.^[13–19] In particular sensing applications are targeted using graphene, which is deposited on surfaces. Thereby, functionalization of deposited graphene can in principle occur on the surface or at the rim of flakes. However, since investigated sensing devices typically have μm dimensions, functionalization at rims of flakes is supposed to have only little influence on the device performance. With drilling


pores into the graphene lattice, the proportion of rims can be increased. In principle, pores can be etched using focused ion beam and the approach allows for regular patterning, shape, and size control.^[16,20–22] Thereby, the successful patterning is a technological challenge. Since the focused ion beam also interacts with the substrate the dielectric layer, such as SiO₂ may become damaged. Thus, although that approach is appealing, it bears some drawbacks, since high-end technology is required.^[16,23]

The growth of pores in graphene on the single-layer level is described by numerous methods in the literature in particular etching methods.^[24] Nanometer-sized pores were created in graphene by oxygen plasma or other plasmas.^[25,26] Moreover, pores on the nanoscale were created in few-layered graphene using oxygen, ozone, or liquid phase etching using HNO₃ solution as etching reagents.^[26–28] In addition, it is reported that a single Ni atom can be used to cut graphene to a nanomesh with a pore size of about 10–50 nm.^[29] Sub-nanometer diameter pores in single-layer graphene membranes were also fabricated, accordingly, defects were introduced into the graphene lattice through ion bombardment and oxidative etching enlarged defects into pores with sizes of 0.40 ± 0.24 nm.^[30,31] Moreover, also graphene oxide

Y. Wang, M. Hußmann, Q. Cao, Y. Hu, Prof. S. Eigler
Institute of Chemistry and Biochemistry
Freie Universität Berlin
Takustraße 3, 14195 Berlin, Germany
E-mail: siegfried.eigler@fu-berlin.de

Dr. C. Neumann, Prof. A. Turchanin
Institute of Physical Chemistry
Center for Energy and Environmental Chemistry (CEEC) Jena
Friedrich Schiller University Jena
Lessingstraße 10, 07743 Jena, Germany

O. Garrity, Dr. P. Kusch
Department of Physics
Freie Universität Berlin
Arnimallee 14, 14195 Berlin, Germany

 The ORCID identification number(s) for the author(s) of this article can be found under <https://doi.org/10.1002/admi.202100783>.

© 2021 The Authors. Advanced Materials Interfaces published by Wiley-VCH GmbH. This is an open access article under the terms of the Creative Commons Attribution License, which permits use, distribution and reproduction in any medium, provided the original work is properly cited.

DOI: 10.1002/admi.202100783

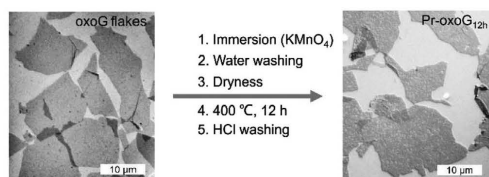


Figure 1. Scheme describing the fabrication of pores starting from oxoG. Flakes of oxoG are deposited on a Si/SiO₂ substrate. Pr-oxoG_{12h} is fabricated from oxoG, immersed in KMnO₄ solution, followed by washing, drying, and annealing in argon atmosphere at 400 °C for 12 h. The white scale bar relates to 10 μm in optical microscopy images.

was used as precursor for etching pores, however, no uniform size was reported and the size of pores is limited to few nm, assumedly due to too many lattice defect sites already present in common graphene oxide, which act as origins for etching. Thus, the formation of larger pores is not possible, since flakes start to disintegrate.^[28,32–35] Accordingly, graphene oxide with extended lattice defects conceptionally can't be considered as a precursor for generating graphene with pores of reasonable lateral dimensions, of tens to hundreds of nm (Table S1, Supporting Information). Here we describe the formation of pores of circular shape by a Mn-species assisted etching procedure at 400 °C in argon atmosphere. The approach starts from oxo-functionalized graphene (oxoG) with a low density of initial vacancy defects (0.8%, as determined by Raman spectroscopy), which is a subclass of the graphene oxide family. By controlling the reaction conditions, it is possible to gain a certain control over the formation of pores with diameters between 100–200 nm in majority. Those pore-graphene materials are highly temperature stable since they are synthesized at 400 °C. Moreover, integration into heterostructures is possible. We report that the amplitude of the photoluminescence (PL) signal of MoS₂ enhances 10-times.

2. Results and Discussion

The formation of pores in monolayers of oxoG was elaborated in a five-step procedure (Figure 1). Accordingly, oxoG flakes are deposited on Si/300 nm SiO₂ wafer by Langmuir–Blodgett technique.^[36–38] The lateral dimensions of monolayer oxoG flakes are roughly 20 μm (Figure 1 left and Figure S2A–C, Supporting Information). Figure S1A,B, Supporting Information, show the results of the statistical Raman analysis of flakes of reduced oxoG revealing an I_D/I_G ratio of the defect induced D band and the G band of 2.7 ± 0.14 and a full-width at half-maximum (Γ) of the 2D band $\Gamma_{2D} = 93 \pm 9 \text{ cm}^{-1}$. Thus, the average distance of defects L_D is about 2 nm, following the relation introduced by Lucchese and Cançado.^[39,40] The distance of defects can be related to a density of defects of about 0.8%.

Then the wafer was immersed into a solution of potassium permanganate (KMnO₄) overnight (for details see experimental part). Metal ions are bound to the surface of the single-layers of oxoG on Si/SiO₂ substrates. A study based on the roughness analysis performed by atomic force microscopy (AFM) was conducted focusing on one specific flake of oxoG before and after KMnO₄ immersion (step 1 in Figure 1) and finally after washing the surface with water (step 2 in Figure 1, see also Figure S2,

Supporting Information). Line height scans indicate that the root mean square roughness of the surface increases from about 0.14 nm to about 0.39 and 0.32 nm, respectively. As we showed before, organosulfate groups with hydronium counter ions explain the thickness of flakes of oxoG.^[41] Here, we propose that hydronium ions are exchanged by Mn-species. Although we realized that step 2, washing the wafer with water to remove possible excess or loosely bound Mn-species is essential for the controlled growth of pores, the AFM height profile remains similar (Figure S2F, Supporting Information) with a roughness of 0.32 nm. After drying the sample at room temperature, the annealing process was carried out in a tube furnace in argon at 400 °C for 12 h. Afterward, the annealed material on the wafer was washed with 1 M hydrochloric acid (HCl) to remove metal or metal oxide particles.^[33] The annealing process induces the disproportionation reaction of oxoG, and we identified in an earlier study that pores can grow by the release of CO₂, while intact graphene patches with diameters of around 3 nm in diameter are generated, as a consequence of mobile oxo-groups on the lattice of graphene.^[42] However, by the here described procedure, graphene with pores (Pr-oxoG_{12h}; index indicated the annealing time) is generated with much larger pores.

By varying the annealing time, graphene materials with pores of different sizes are generated. The formed pores can be visualized by AFM and optical microscopy, respectively. Here, through comparative experiments, we can confirm that manganese plays a very important role in the formation process of pores. For single layers, we suggest that there are small nanoparticles at the edges of pores. Because of the little amount, the content is below the detection limit of, for example, X-ray photoelectron spectroscopy (XPS) or Raman (Mn–O vibrations, Figure S6A, Supporting Information). We further assume that the metal particles move along the edge of the pore to continuously catalyze the pore formation leading to increased diameters of pores. Accordingly, based on this assumption it can be explained why round pores are formed, and thus, the size of the pores can be controlled by etching-time. Figure S3A, Supporting Information, shows an AFM image of single-layer oxoG with no visible pores in the zoomed area depicted in Figure S3B, Supporting Information. As we visualized before by transmission electron microscopy at atomic resolution, oxoG bears only one or few atom vacancies.^[42,43] Figure S3C,D, Supporting Information, show AFM images of Pr-oxoG_{6h}. The presence of small pores is visible in Figure S3D, Supporting Information. To make the comparison reliable, we analyzed the same flake and same area of the flake before and after annealing. Therefore, we conclude that there are small pores of $45 \pm 24 \text{ nm}$ formed in Pr-oxoG_{6h}, as can be observed from Figure S3D and Table S2, Supporting Information.^[30]

Extending the annealing time from 6 to 12 h results in the formation of larger pores (Pr-oxoG_{12h}). Pores in Pr-oxoG_{12h} on Si/SiO₂ substrates are visible under the optical microscope (Figure 2A). As shown in the AFM image of Figure 2B, (the stacked square is visible in the center with higher resolution) there are many pores distributed over the entire flake. An AFM image with a further enlarged area of the flake of Pr-oxoG_{12h} is depicted in Figure 2C. The circular shape of pores with an apparently uniform size of $147 \pm 73 \text{ nm}$ is clearly visible (Table S2, Supporting Information). The height of Pr-oxoG_{12h} is about 1.4 nm, as measured by the AFM tip hitting the underneath surface

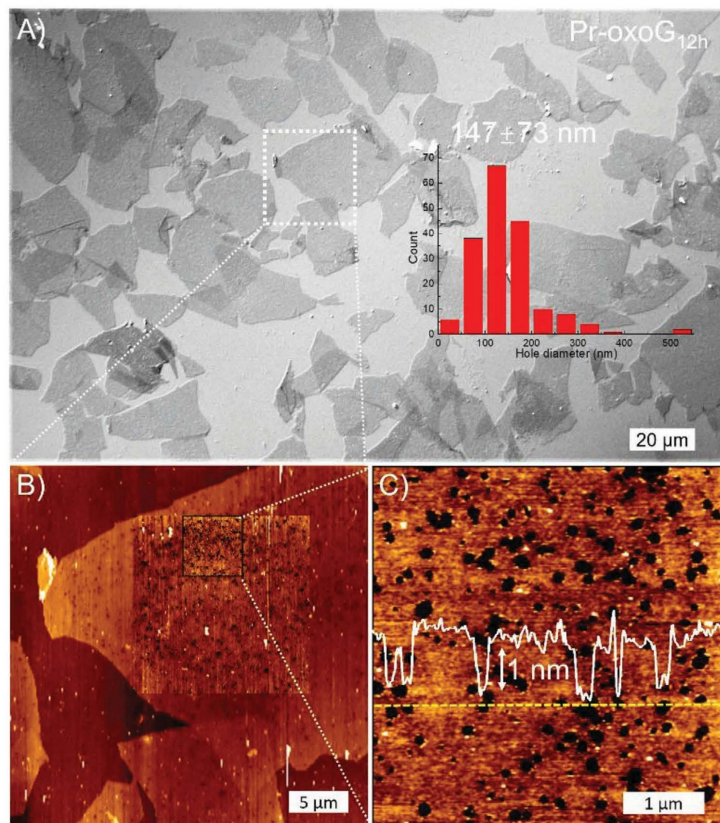


Figure 2. A) Optical microscopy image (differential interference contrast, DIC) of flakes of Pr-oxoG_{12h} on Si/SiO₂ substrates. Inset: histogram shows the size distribution of pores shown in B and C, smaller than 50 nm are not counted. B) AFM topography image of Pr-oxoG_{12h} with overlay of detailed scanned area; C) zoomed AFM topography image of (B) showing pores. White line: height profile, arrow indicates 1 nm.

through the pores. The results of the quantitative analysis of the lateral dimensions of pores in graphene are illustrated in the histogram shown in the inset of Figure 2A. The analysis reveals that the pores diameters are roughly 150 ± 70 nm.

Skipping the final step of HCl washing results in an increased height when measuring through a hole from the SiO₂ surface to the surface of graphene (Figure 3). We assume that a uniform hydration layer may be present between the substrate and graphene. We note that Mn-species, such as nanoparticles, supposed to be located at the rims of pores are not detected by AFM.^[29,33] An analysis of the pore size before and after HCl washing indicates a little increase from 129 ± 75 to 147 ± 72 nm in Figure 3D. Those data are also listed in Table S2, Supporting Information. Next, a reference experiment was performed to eliminate the possibility that similar pores are formed using oxoG without the influence of Mn-species. Thus, flakes of oxoG were annealed for 12 h. As shown in Figure S4, Supporting Information, by optical microscopy and AFM, no

obvious large pores are observed. Therefore, we conclude that annealing alone is not leading to the formation of large pores, starting from oxoG.

To further investigate the effect of annealing time on the pore diameter, we further extended the processing time to 16 h. As shown in Figure S5, Supporting Information, large and merged pores are visible for Pr-oxoG_{16h}, both in the optical microscopy image of Figure S5A, Supporting Information, and AFM images of Figure S5B,C, Supporting Information. As shown in Figure S5B, Supporting Information, there are many pores in the flakes (enlargement in Figure S5C, Supporting Information) and the mean diameter is 168 ± 94 nm. To gain more insights into the mechanism of pore formation process was conducted on few-layers of oxo-G. The AFM images in Figure S6, Supporting Information, reveal some dots in the center of the pore. The thickness of the dots is basically the same as the material height. We suggest that those dots are either trapped etched carbon dots or manganese nanoparticles.

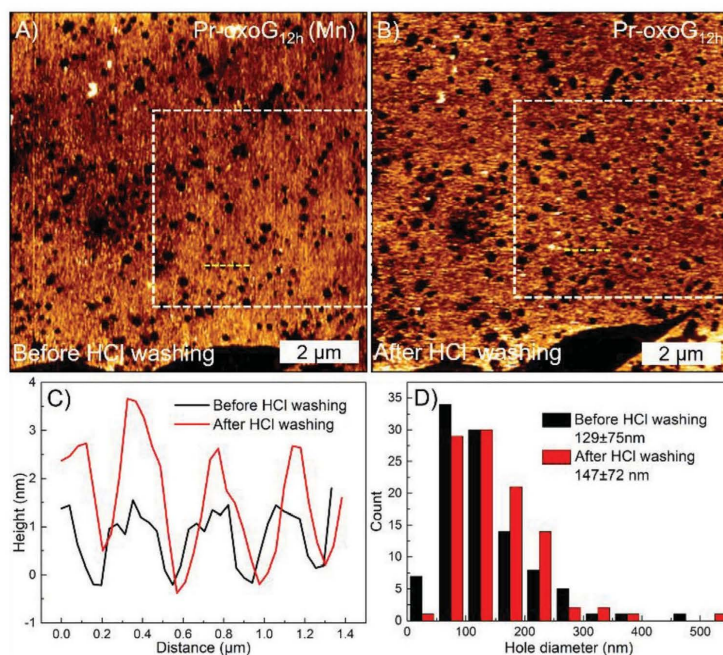


Figure 3. AFM topography images in (A); before (Pr-oxoG_{12h} (Mn)), and B) after (Pr-oxoG_{12h}) HCl washing. C) Height profiles of AFM images along yellow dashed lines. The black and red lines represent the pores height profiles of Pr-oxoG_{12h} (Mn) and Pr-oxoG_{12h}, respectively. D) Distribution of pores in the white box. The black and red bars represent the pores quantity profiles of Pr-oxoG_{12h} (Mn) and Pr-oxoG_{12h}.

Although, evidence is found supporting the hypothesis of the catalytic role of Mn-species such as Mn-atoms or nanoparticles, the final proof is a matter of further research.

A comparison between the different mean diameters and mean pore areas after different annealing time are shown in Figure S7, Supporting Information (data listed in the Table S2, Supporting Information). As the pyrolysis time increases, the average diameter and area of the pores increase according. In the process of growing pores, as shown in Figure 1, we pointed out that skipping washing step 2 with water results in a highly uncontrolled etching process. Compared with Figure 2A, the same annealing time of 12 h was chosen and the AFM image in Figure S8, Supporting Information, shows small pores, very large and also merged pores distributed all over the flakes. We suggest that Mn-species are unevenly distributed on the surface of oxoG if the water washing step is skipped. We note that we observed also partly destroyed and crumpled/folded layers. Therefore, we conclude that washing step 2 is essential to control the generation of pores, and to get some control over the uniformity of grown pores.

Next, an XPS study was conducted to analyze changes in the chemical composition of oxoG and Pr-oxoG_{12h} (Figure 4). All XPS data are listed in Table S3. The high-resolution C 1s spectrum of oxoG in Figure 4A displays a typical saddle-like pattern, which stems from significant oxidation in oxoG.

The content of sp²-C is about 47.8% (due to oxo-groups) and the content of C–O/C–OH/C=O is up to 46.3%. It can be seen from the high-resolution Mn 2p that there is no obvious peak in Figure 4E. Thus, few-layer oxoG contains less than 0.1 at% Mn. Before HCl washing, the high-resolution Mn 2p of Pr-oxoG_{12h} (Mn) reveals also less than 0.1 at% Mn, as shown in Figure 4F. This finding further support that little quantities of Mn-species are catalytically active in the etching process. After annealing, the oxygen content of Pr-oxoG_{12h} is significantly reduced compared to oxoG. As expected, the content of sp²-C increased, here to 50.8%. The high-resolution O 1s spectrum of Pr-oxoG_{12h} displays the peaks of C–O, C=O, O–C=O (Figure 4D). We note that the O 1s peak in Figure 4B is only for reference, since Pr-oxoG_{12h} is not completely covering the Si/SiO₂ substrate and since large pores exist in Pr-oxoG_{12h}. Thus, the influence of the surface O-signal from SiO₂ is affecting the quantitative analysis. The oxygen content is significantly reduced in comparison to oxoG and close to zero if we consider its influence on SiO₂.^[2,44,45] We note, for analyzing the C–O species the C 1s analysis is representative. The analyses of C 1s peaks reveal the formation of C=O and C–O/C–OH groups as a consequence of annealing and the accompanied growth of pores (Figure 4B). Thus, we conclude that the rims of pores are functionalized by carbonyl groups in addition to hydroxyl and carboxyl groups.

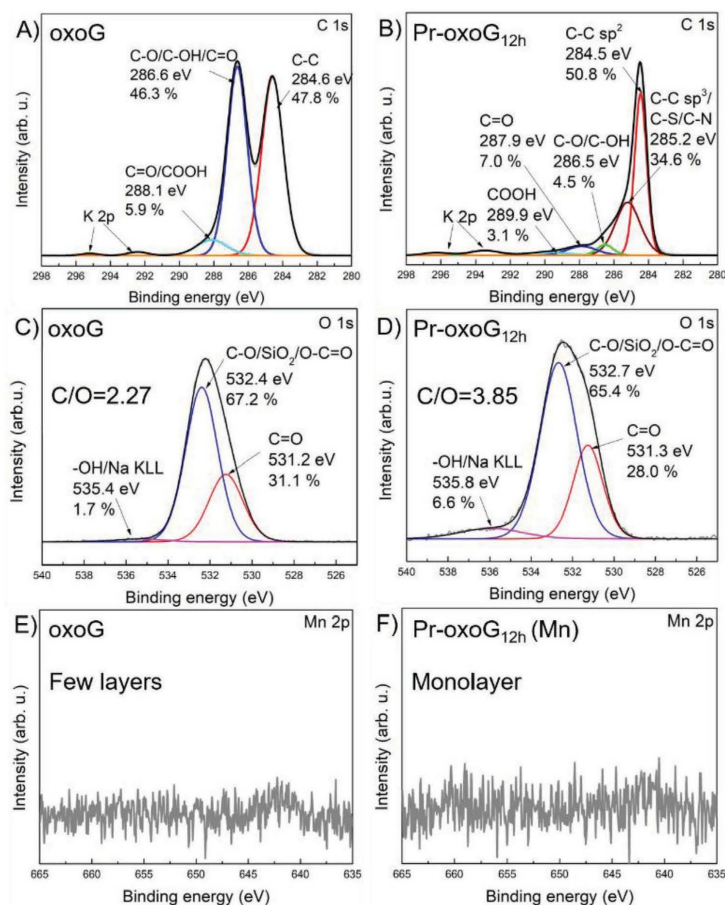


Figure 4. High-resolution C 1s (top) and O 1s (middle) spectra of (A), C) oxo-G, and B,D) Pr-oxoG_{12h}. High-resolution Mn 2p spectra (bottom) of E) oxo-G and F) Pr-oxoG_{12h} (Mn).

Moreover, with growing pores into graphene the sp^2 -patches become smaller and consequently, the Raman spectra in Figure S9, Supporting Information, shows, as expected, a broadened D peak with $\Gamma_D = 106 \text{ cm}^{-1}$ for Pr-oxoG_{12h}, compared to $\Gamma_D = 84 \text{ cm}^{-1}$ for oxoG.

In the following, oxoG and Pr-oxoG_{12h}, respectively, are used to fabricate van-der-Waals heterostructures with a single-layer flake of MoS₂ deposited on top (illustrated in Figure 5). Raman spectra (Figure S10, Supporting Information) confirm that the transferred flake of MoS₂ is a monolayer by the measured difference between the out-of-plane A_{1g} mode and the E_{2g} mode of about 19.0 cm^{-1} , as typical for a monolayer.^[46] For the fabrication of the heterostructures, we used a previously described procedure.^[47] Figures 5B,D show optical microscopy images of the realized oxoG/MoS₂ and Pr-oxoG_{12h}/MoS₂ heterostructures,

respectively. The AFM images of the Pr-oxoG_{12h}/MoS₂ heterostructure is depicted in Figure S11A,B, Supporting Information, and proved the expected morphology.

The PL of MoS₂ on SiO₂, on oxoG, on Pr-oxoG_{6h}, and on Pr-oxoG_{12h} are studied next. Figure 5E shows the respective PL of heterostructures. Obviously, the amplitude of the PL is increased for oxoG/MoS₂ and Pr-oxoG_{12h}/MoS₂, using pure MoS₂ on Si/SiO₂ substrate as internal reference, respectively, compared to the PL of the MoS₂ monolayer. The most intense PL is detected for Pr-oxoG_{12h}/MoS₂ with a 10-times increased amplitude. In contrast, the PL of Pr-oxoG_{6h}/MoS₂ is increased 3-times (Figure S12, Supporting Information) and for oxoG/MoS₂ a fourfold increased PL. As depicted in Figure 6 there is a constant PL intensity over the complete flake, without any modulation. A related investigation demonstrated that

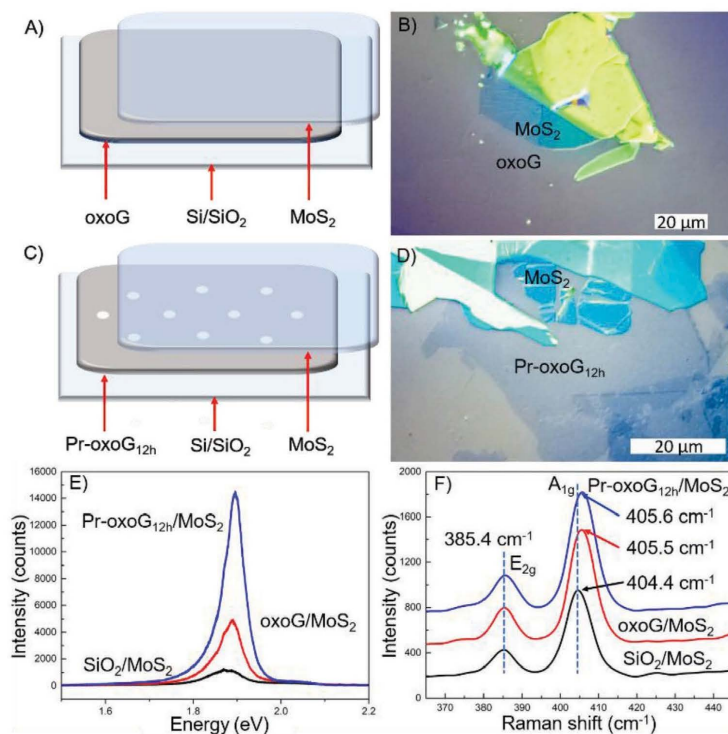


Figure 5. A) Illustration of the heterostructure of oxoG/MoS₂ and B) optical microscopy image of the realized oxoG/MoS₂ heterostructure. C) Illustration of the heterostructure of Pr-oxoG_{12h}/MoS₂ and D) optical microscopy image of the realized Pr-oxoG_{12h}/MoS₂ heterostructure. E) PL spectra of monolayer MoS₂ on SiO₂ (black), oxoG/MoS₂ (red), and Pr-oxoG_{12h}/MoS₂ (blue). F) Raman spectra of the same samples as in (E).

graphene oxide forms a p-type contact with monolayer MoS₂ and this is plausible due to electron-accepting groups detected by XPS, such as carbonyl groups.^[48] Overall, the highest PL enhancement is achieved by using Pr-oxoG_{12h}. Figure 5F shows the Raman spectra of heterostructures detecting the A_{1g} mode of MoS₂ in the heterostructures at around 404.4 cm⁻¹, which is blue-shifted to 405.5 and 405.6 cm⁻¹ for MoS₂ on oxoG and Pr-oxoG_{12h}, respectively, while the position of E_{2g} mode is not shifted. Those observations indicate the p-doping of MoS₂ in the heterostructures by oxoG and Pr-oxoG_{12h}, respectively.^[49,50] Moreover, Pr-oxoG_{12h} reflects a p-doped graphene type material, as indicated by the analysis of the shifts of the G and 2D peak, respectively (Figure S15, Supporting Information). The p-doping effect of Pr-oxoG_{12h} was further investigated by fabricating a heterostructure with a trilayer of MoS₂. Consistent with the expectations, the PL investigation (Figure S13, Supporting Information) indicates less enhancement (trilayer MoS₂ possesses an indirect band-gap), however, a fourfold increased PL is measured, compared to that of a monolayer MoS₂ with a direct band-gap on SiO₂. Thus, the highest, here 10-times increased PL is detected for assembled heterostructure of monolayer Pr-oxoG_{12h}/MoS₂.

In order to exclude the influence of remaining Mn-species on the PL, the PL enhancement of Pr-oxoG_{12h} (Mn) (without HCl washing) was studied by forming the heterostructure of Pr-oxoG_{12h} (Mn)/MoS₂. As shown in Figure S14, Supporting Information, the PL increases, however, only twice, indicating that full enhancement of PL is only achieved after HCl washing and the accompanied removal of particles. Thus, we speculate that Mn-species may form complexes with, for example, carbonyl groups at the rims of pores inhibiting the dramatic PL enhancement, although Raman spectra show the E_{2g} shift to 405.6 cm⁻¹ for Pr-oxoG_{12h} (Mn)/MoS₂. We note that the experimental observations give evidence for a p-doping effect by pore-graphene.

3. Conclusion

Here, we demonstrated the fabrication of graphene with circular pores on the 100 nm scale deposited on Si/SiO₂ surface by annealing of oxo-functionalized and potassium permanganate treated graphene flakes at 400 °C. While excess of Mn-species leads to heterogeneously formed pores and

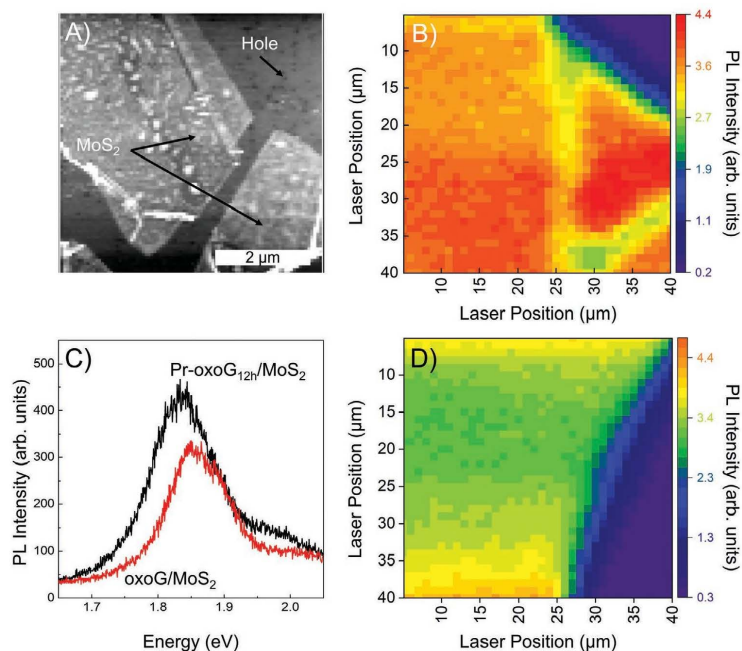


Figure 6. A) Features an AFM map of MoS₂ on top of Pr-oxoG_{12h}. Holes of sizes ranging from 50 nm to 200 nm are visible in the top right of the image and are well separated from one another. The Pr-oxoG_{12h}/MoS₂ PL intensity map (B) shows a constant PL intensity over the MoS₂ flake, exhibiting no sign of a spatial PL modulation that may arise from free-standing MoS₂. C) shows PL spectra from oxo-G/MoS₂ (red) and Pr-oxoG_{12h}/MoS₂ (black), the PL on the Pr-oxoG_{12h} sample exhibiting higher intensity than that seen in the oxo-G/MoS₂ sample. A PL Intensity map of oxo-G/MoS₂ (D) taken with the same parameters as (B) shows a similar constant PL intensity in addition to having slightly lower intensity to that of Pr-oxoG_{12h}/MoS₂.

destroyed flakes, removal of excess potassium permanganate leads to the growth of circular pores with diameters of 50 to 250 nm, depending on the annealing time. Thereby, for example, uniform pores have mean diameters of 147 ± 73 nm after annealing for 12 h. From XPS analysis we conclude that carbonyl, hydroxyl, and carboxyl groups decorate the rims of pores. Since carbonyl groups have electron-accepting properties, it is plausible that the 2D material pore-graphene, can p-dope other 2D materials, such as MoS₂. However, further research, such as correlating field-effect measurements with PL mapping is necessary to further elucidate the mechanism behind PL enhancement by 10-times. Moreover, we showed that Mn-impurities limit the increase of the PL of MoS₂ in the heterostructure with pore-graphene and thus, we propose that the interaction of Mn-species with carbonyl groups may be responsible. Moreover, we conclude that not all defects detected by Raman spectroscopy lead to the growth of pores, taking into account that the initial distance of defects is 2 nm and the final pore-size increased to several hundreds of nm. Finally, we propose that pore-graphene is a 2D material with functional groups at the rims of pores and thus an attractive novel material for sensing applications in the future.

Supporting Information

Supporting Information is available from the Wiley Online Library or from the author.

Acknowledgements

This research is supported by the China Scholarship Council (CSC). C.N. and A.T. acknowledge DFG financial support via the research infrastructure grant INST 275/257-1 FUGG (project no. 313713174), funding through ESF Research Group 2019 FGR 0080 "ESTI" and BMWi project ZF4817401VS9 "TDraCon". P.K. acknowledges DFG for financial support within project no. PP2244.

Open access funding enabled and organized by Projekt DEAL.

Conflict of Interest

The authors declare no conflict of interest.

Data Availability Statement

The data that support the findings of this study are available from the corresponding author upon reasonable request.

Keywords

graphene, graphene oxide, membranes, photoluminescence, porous graphene

Received: May 14, 2021
Revised: June 15, 2021
Published online: August 3, 2021

- [1] C. Neumann, D. Kaiser, M. J. Mohn, M. Fuser, N.-E. Weber, O. Reimer, A. Gölzhäuser, T. Weimann, A. Terfort, U. Kaiser, A. Turchanin, *ACS Nano* **2019**, *13*, 7310.
- [2] Z. Wang, Q. Yao, C. Neumann, F. Borrrnert, J. Renner, U. Kaiser, A. Turchanin, H. J. W. Zandvliet, S. Eigler, *Angew. Chem., Int. Ed.* **2020**, *59*, 13657.
- [3] F. Hao, D. Fang, Z. Xu, *Appl. Phys. Lett.* **2011**, *99*, 041901.
- [4] B. Zhan, C. Li, J. Yang, G. Jenkins, W. Huang, X. Dong, *Small* **2014**, *10*, 399.
- [5] D. Akinwande, C. J. Brennan, J. S. Bunch, P. Egberts, J. R. Felts, H. Gao, R. Huang, J.-S. Kim, T. Li, Y. Li, K. M. Liechti, N. Lu, H. S. Park, E. J. Reed, P. Wang, B. I. Yakobson, T. Zhang, Y.-W. Zhang, Y. Zhou, Y. Zhu, *Extreme Mech. Lett.* **2017**, *13*, 42.
- [6] J. Xie, Q. Chen, H. Shen, G. Li, *J. Electrochem. Soc.* **2020**, *167*, 037541.
- [7] K. G. Zhou, K. S. Vasu, C. T. Cherian, M. Neek-Amal, J. C. Zhang, H. Ghorbanfekr-Kalashami, K. Huang, O. P. Marshall, V. G. Kravets, J. Abraham, Y. Su, A. N. Grigorenko, A. Pratt, A. K. Geim, F. M. Peeters, K. S. Novoselov, R. R. Nair, *Nature* **2018**, *559*, 236.
- [8] W. Wu, Y. Shi, G. Liu, X. Fan, Y. Yu, *Desalination* **2020**, *491*, 114452.
- [9] H. Liu, H. Wang, X. Zhang, *Adv. Mater.* **2015**, *27*, 249.
- [10] Q. Xu, H. Xu, J. Chen, Y. Lv, C. Dong, T. S. Sreeprasad, *Inorg. Chem. Front.* **2015**, *2*, 417.
- [11] C. E. Halbig, R. Lasch, J. Krull, A. S. Pirzer, Z. Wang, J. N. Kirchof, K. I. Bolotin, M. R. Heinrich, S. Eigler, *Angew. Chem., Int. Ed.* **2019**, *58*, 3599.
- [12] A. Criado, M. Melchionna, S. Marchesan, M. Prato, *Angew. Chem., Int. Ed.* **2015**, *54*, 10734.
- [13] S. Chen, J. Duan, M. Jaroniec, S. Z. Qiao, *J. Mater. Chem. A* **2013**, *1*, 9409.
- [14] A. C. Lokhande, I. A. Qattan, C. D. Lokhande, S. P. Patole, *J. Mater. Chem. A* **2020**, *8*, 918.
- [15] Y. Zhang, Q. Wan, N. Yang, *Small* **2019**, *15*, 1903780.
- [16] A. Guirguis, J. W. Maina, L. Kong, L. C. Henderson, A. Rana, L. H. Li, M. Majumder, L. F. Dumée, *Carbon* **2019**, *155*, 660.
- [17] X. Yang, C. Cheng, Y. Wang, L. Qiu, D. Li, *Science* **2013**, *341*, 534.
- [18] S. Han, D. Wu, S. Li, F. Zhang, X. Feng, *Adv. Mater.* **2014**, *26*, 849.
- [19] H. Yang, Q. He, Y. Liu, H. Li, H. Zhang, T. Zhai, *Chem. Soc. Rev.* **2020**, *49*, 2916.
- [20] C. J. Russo, J. A. Golovchenko, *Proc. Natl. Acad. Sci. USA* **2012**, *109*, 5953.
- [21] S. Standop, O. Lehtinen, C. Herbig, G. Lewes-Malandrakis, F. Craes, J. Kotakoski, T. Michely, A. V. Krashenninnikov, C. Busse, *Nano Lett.* **2013**, *13*, 1948.
- [22] A. Guirguis, J. W. Maina, X. Zhang, L. C. Henderson, L. Kong, H. Shon, L. F. Dumée, *Mater. Horiz.* **2020**, *7*, 1218.
- [23] N. I. Kato, *J. Electron Microscop.* **2004**, *53*, 451.
- [24] Y. Lin, Y. Liao, Z. Chen, J. W. Connell, *Mater. Res. Lett.* **2017**, *5*, 209.
- [25] S. P. Surwade, S. N. Smirnov, I. V. Vlasiouk, R. R. Unocic, G. M. Veith, S. Dai, S. M. Mahurin, *Nat. Nanotechnol.* **2015**, *10*, 459.
- [26] T. He, Z. Wang, F. Zhong, H. Fang, P. Wang, W. Hu, *Adv. Mater. Technol.* **2019**, *4*, 1900064.
- [27] A. Kaplan, Z. Yuan, J. D. Benck, A. Govind Rajan, X. S. Chu, Q. H. Wang, M. S. Strano, *Chem. Soc. Rev.* **2017**, *46*, 4530.
- [28] X. Wang, L. Jiao, K. Sheng, C. Li, L. Dai, G. Shi, *Sci. Rep.* **2013**, *3*, 1996.
- [29] H. Zhang, W. Liu, Z. Zhang, M. Li, B. Xu, J. Guo, *Phys. Chem. Chem. Phys.* **2018**, *20*, 26814.
- [30] S. C. O'Hern, M. S. Boutilier, J. C. Idrobo, Y. Song, J. Kong, T. Laoui, M. Atieh, R. Karnik, *Nano Lett.* **2014**, *14*, 1234.
- [31] L. Huang, M. Zhang, C. Li, G. Shi, *J. Phys. Chem. Lett.* **2015**, *6*, 2806.
- [32] H.-K. Kim, S.-M. Bak, S. W. Lee, M.-S. Kim, B. Park, S. C. Lee, Y. J. Choi, S. C. Jun, J. T. Han, K.-W. Nam, K. Y. Chung, J. Wang, J. Zhou, X.-Q. Yang, K. C. Roh, K.-B. Kim, *Energy Environ. Sci.* **2016**, *9*, 1270.
- [33] D. Zhou, Y. Cui, P. W. Xiao, M. Y. Jiang, B. H. Han, *Nat. Commun.* **2014**, *5*, 4716.
- [34] Z. Fan, Q. Zhao, T. Li, J. Yan, Y. Ren, J. Feng, T. Wei, *Carbon* **2012**, *50*, 1699.
- [35] Y. Xu, C.-Y. Chen, Z. Zhao, Z. Lin, C. Lee, X. Xu, C. Wang, Y. Huang, M. I. Shaker, X. Duan, *Nano Lett.* **2015**, *15*, 4605.
- [36] S. Eigler, *Phys. Chem. Chem. Phys.* **2014**, *16*, 19832.
- [37] S. Eigler, M. Enzelberger-Heim, S. Grimm, P. Hofmann, W. Kroener, A. Geworski, C. Dotzer, M. Rockert, J. Xiao, C. Papp, O. Lytken, H. P. Steinruck, P. Müller, A. Hirsch, *Adv. Mater.* **2013**, *25*, 3583.
- [38] S. Eigler, F. Hof, M. Enzelberger-Heim, S. Grimm, P. Müller, A. Hirsch, *J. Phys. Chem. C* **2014**, *118*, 7698.
- [39] M. M. Lucchese, F. Stavale, E. H. M. Ferreira, C. Vilani, M. V. O. Moutinho, R. B. Capaz, C. A. Achete, A. Jorio, *Carbon* **2010**, *48*, 1592.
- [40] L. G. Cancado, A. Jorio, E. H. Ferreira, F. Stavale, C. A. Achete, R. B. Capaz, M. V. Moutinho, A. Lombardo, T. S. Kulmala, A. C. Ferrari, *Nano Lett.* **2011**, *11*, 3190.
- [41] S. Eigler, C. Dotzer, F. Hof, W. Bauer, A. Hirsch, *Chem. - Eur. J.* **2013**, *19*, 9490.
- [42] F. Grote, C. Gruber, F. Börrnert, U. Kaiser, S. Eigler, *Angew. Chem., Int. Ed.* **2017**, *56*, 9222.
- [43] P. Feicht, J. Biskupek, T. E. Gorelik, J. Renner, C. E. Halbig, M. Maranska, F. Puchtl, U. Kaiser, S. Eigler, *Chem. - Eur. J.* **2019**, *25*, 8955.
- [44] M. González, J. Baselga, J. Pozuelo, *J. Mater. Chem. C* **2016**, *4*, 8575.
- [45] K. Garg, R. Shanmugam, P. C. Ramamurthy, *Opt. Mater.* **2018**, *76*, 42.
- [46] C. Lee, H. Yan, L. E. Brus, T. F. Heinz, J. Hone, S. Ryu, *ACS Nano* **2010**, *4*, 2695.
- [47] Z. Wang, Q. Yao, Y. Hu, C. Li, M. Hußmann, B. Weintrub, J. N. Kirchof, K. Bolotin, T. Taniguchi, K. Watanabe, S. Eigler, *RSC Adv.* **2019**, *9*, 38011.
- [48] T. Musso, P. V. Kumar, A. S. Foster, J. C. Grossman, *ACS Nano* **2014**, *8*, 11432.
- [49] X. Wei, Z. Yu, F. Hu, Y. Cheng, L. Yu, X. Wang, M. Xiao, J. Wang, X. Wang, Y. Shi, *AIP Adv.* **2014**, *4*, 123004.
- [50] W. Zhang, J.-K. Huang, C.-H. Chen, Y.-H. Chang, Y.-J. Cheng, L.-J. Li, *Adv. Mater.* **2013**, *25*, 3456.

**ADVANCED
MATERIALS**
INTERFACES

Supporting Information

for *Adv. Mater. Interfaces*, DOI: 10.1002/admi.202100783

Synthesis of Wet-Chemically Prepared Porous-
Graphene Single Layers on Si/SiO₂ Substrate Increasing
the Photoluminescence of MoS₂ in Heterostructures

*Yiqing Wang, Christof Neumann, Marleen Hußmann,
Qing Cao, Yalei Hu, Oisín Garrity, Patryk Kusch, Andrey
Turchanin, and Siegfried Eigler**

Supporting Information

Synthesis of p-doped porous-graphene single layers on Si/SiO₂ substrate increasing the photoluminescence of MoS₂ in heterostructures

Yiqing Wang, Christof Neumann Marleen Hußmann, Qing Cao, Yalei Hu, Oisín Garrity, Patryk Kusch, Andrey Turchanin, Siegfried Eigler

Experimental Section

Materials and Methods

Double-distilled water from Carl Roth GmbH. Graphite (3061) was obtained from Asbury Carbon. Si wafers with a 300 nm thick SiO₂ layer were purchased from Fraunhofer Institut für Integrierte Systeme und Bauelementetechnologie IISB in Erlangen. Chemicals were purchased from Sigma-Aldrich. A Nikon Eclipse LV150-NL with differential interference contrast was used to visualize materials. Statistical Raman spectroscopy (SRS) was recorded using a Horiba Explora spectrometer with a 532 nm laser for excitation combined with 100x magnification objective. Increment of Raman spectra measurements is 0.7 µm. PL map parameters for Figure 6: The steps between two recorded spectra was 250 nm, with a laser spot size of around 400 nm. As excitation we use a 532 nm laser and kept the laser power below 0.5 mW to avoid sample heating. As a reference, we record a PL map with the same experimental parameters for a sample without holes.

For preparation of Langmuir-Blodgett films, we used a Kibron µThrough system with water as subphase. The surface tension of water = 72.8 mN m⁻¹ was set to zero. The films were formed at a surface tension value of 3 mN m⁻¹. AFM images were recorded on an JPK Nanowizard 4 equipped with NSG10/Au probes and intermittent contact mode was chosen. Using Tap300-G AFM Probe. X-ray photoelectron spectroscopy (XPS) was performed using a multiprobe system (Scienta Omicron) with a monochromatic X-ray source (Al K_α) and an electron analyzer (Argus CU) with 0.6 eV spectral energy resolution. The spectra were fitted using Voigt functions (30:70) after Shirley background subtraction. The Si 2p peak (SiO₂, 103.5 eV) was used for binding energy calibration. Putting the entire substrate with monolayer flakes in the XPS instrument.

Synthesis of Oxo-Functionalized Graphene (oxoG)

OxoG was prepared by low-temperature oxidation of graphite according to our previously developed method^[1,2]. Accordingly, 2 g of graphite (type 3061, Asbury Carbon Mills) were mixed with 50 mL of sulfuric acid (97.5%) in a Teflon reactor under mechanical stirring at a temperature below 10 °C. After that, 4 g of KMnO₄ were slowly added within 4 h and further stirred for 16 h. Then, 40 mL of cold diluted sulfuric acid (20 wt%) and followed by 100 mL of cold double distilled water were slowly continuously added through a programmed pump within 4 h and 16 h, respectively. Then, 40 mL of H₂O₂ (5 wt%) were added into the reaction mixture to solubilize manganese species. Then, the dispersion was washed with cold double

distilled water by repeated centrifugation and redispersion in double distilled water for six times.

Formation of films of flakes of oxoG on Si/SiO₂ wafer:

Flakes of oxoG were deposited on a Si/300 nm SiO₂ wafer by Langmuir Blodgett technique. First, a light yellowish oxoG dispersion was prepared by dilution of water/methanol, 1/2 by volume (the exact concentration was found to have only little influence on the quality of the formed film of flakes). The dispersion was dropped on the water-interface of the Langmuir-Blodgett trough and the barriers were compressed until a surface tension of 3 mN/m was reached.

Reduction of flakes of oxoG on Si/SiO₂ wafer (Preparation of red-oxoG).

Wafers with deposited flakes of oxoG were placed in a 20 mL glass vial filled with glass wool and were reduced by the vapor of HI and TFA for 10 min at 80 °C. Subsequently, the wafers were extensively washed with pure water and dried.

Preparation of Pr-oxoG.

Pr-oxoG was prepared by using potassium permanganate (KMnO₄) as the etching agents. Flakes of oxoG on a Si/SiO₂ wafer were immersed in aqueous KMnO₄ solution (0.2 mmol). The oxoG flakes on Si/SiO₂ the wafer was washed with water and dried in the air. Then, the wafer was heated in argon atmosphere at a rate of 10 °C min⁻¹ to 400 °C for 6 h, 12 h and 16 h, respectively and cooled down to room temperature.

Preparation of tp-oxoG.

The oxoG flakes on Si/SiO₂ mixture were dried in the air and then heated at a rate of 10 °C min⁻¹ to 400 °C for 12 h in an atmosphere of Argon and cooled down to room temperature.

Removal of metal containing species.

Annealed wafers were immersed in aqueous HCl solution (1 M) for two days to remove the metal-containing species. Then, wafers were shaken gently in double distilled water to wash off acids. Finally, Pr-oxoG on Si/300 nm SiO₂ wafers is obtained. As reference tp-oxoG was obtained the same way, however without KMnO₄ treatment.

Pore diameter and area analysis

Pore diameters were estimated manually by using the straight line tool in ImageJ. After counting the pores, export the results of the pore diameter and area.^[3]

Table S1. Survey of perforation techniques, with indicated starting material, layer thickness, etching process, realized pore size and targeted application.

Raw material	Thickness	Perforation technique	Pore size (nm)	application	Ref.
Graphene	Few layers	Oxygen plasma, ozone	<5	permeance membranes	[4]
Graphene	Few layers	Focused ions beam (SEM)	<50	-	[5]
Graphene	Monolayer	Bottom-up synthesis	0-250	Charge Transport	[6]
GO	-	Chemical-oxidative etching (KMnO ₄), microwave irradiation.	2-4	supercapacitor	[7]
GO	-	Chemical-oxidative etching (HNO ₃)	60-90	Catalyst (Bulk)	[8]
GO	-	Chemical-oxidative etching (H ₂ O ₂)	2-70	supercapacitor	[9]
Graphene	Few layers	Liquid arc discharge, Ni atoms	10-50	-	[10]
Graphene	Monolayer	Strain-assisted treatment, Pt nanoparticles etching	<50	Charge Transport	[11]
RGO	Few layers	Annealing treatment, Pt nanoparticles etching	<50	-	[11]
GO	Bulk	Annealing treatment, Fe ₂ O ₃ etching	-	electrocatalyst	[12]
RGO	Bulk	Carbothermal reaction by using the metal oxide nanoparticles (Oxometalates)	5-10, 20-50	-	[13]
Oxo-functionalized graphene	Monolayer	Disproportionation functionalization of 4%	1-3	-	[2]
Oxo-functionalized graphene	Monolayer	Disproportionation, functionalization of 60%	5	Charge Transport	[14]

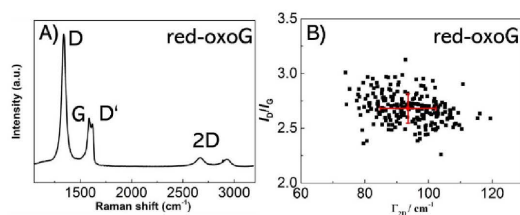


Figure S1. Statistical Raman analysis of chemically reduced oxoG (Statistical Raman microscopy measured at 532 nm laser excitation wavelength. The laser power is below 0.1 mW to avoid heating induced by laser). A) Average spectrum of reduced oxoG with I_D/I_G ratio of 2.7 ± 0.14 and $\Gamma_{2D} = 93 \pm 9 \text{ cm}^{-1}$. B) Scatter plot of I_D/I_G vs FWHM of the 2D peak.

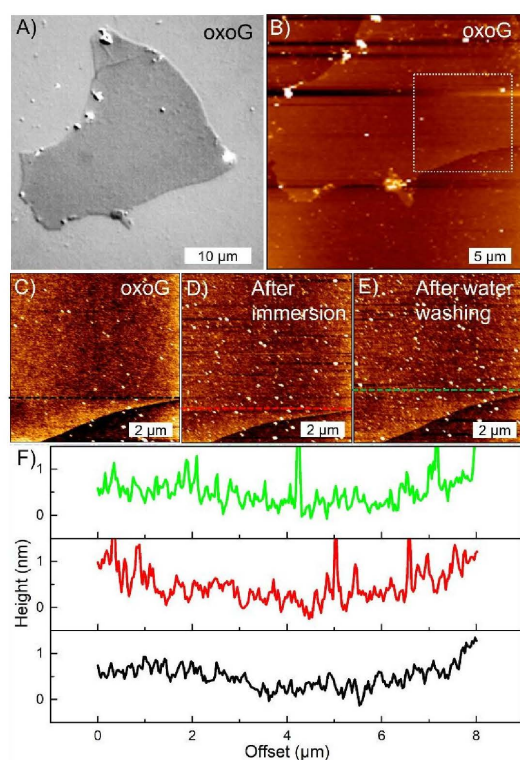


Figure S2. A) Optical microscope images of flakes of oxoG on Si/300 nm SiO₂ wafer and AFM topography images in B and C; before, D) after immersion in KMnO₄ solution and E) after washing in water. F) Height profiles of AFM images along black, red and green lines. The black, red and green line represent the height profiles of oxoG, oxoG after immersion and oxoG after washing with water, respectively.

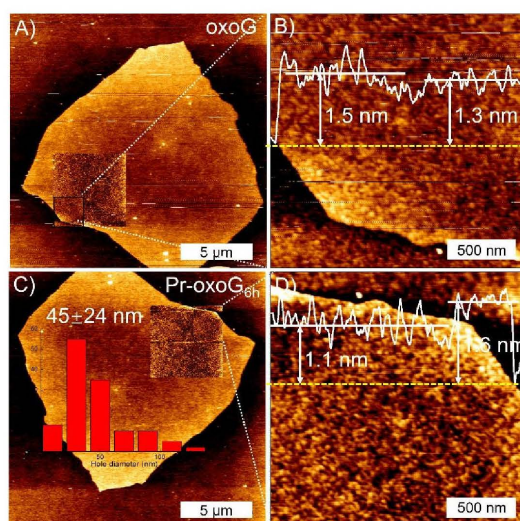


Figure S3. A and B) AFM topography images of single layer oxoG, showing no big pores. C and D) AFM images of Pr-oxoG_{6h}. The yellow lines represent the height profiles of oxoG and Pr-oxoG_{6h}, respectively.

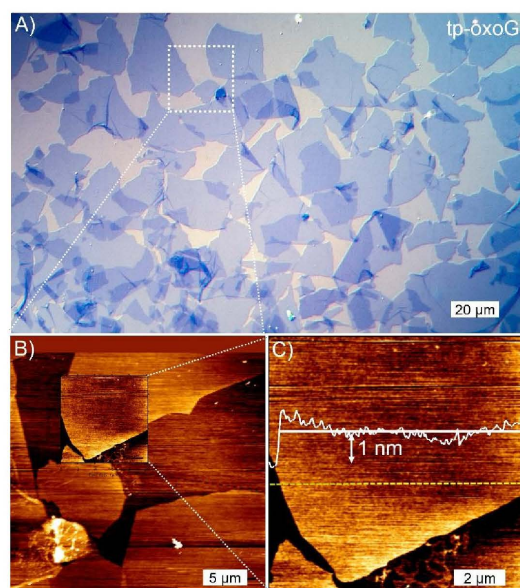


Figure S4. A) Optical microscope image of flakes of tp-oxoG on Si/300 nm SiO₂ substrate. B) AFM topography image of tp-oxoG (12 h annealing time). C) Figure S3B shows no big pores after annealing single layer oxoG for 12 h without Mn-species. The yellow line represents the height profile of tp-oxoG.

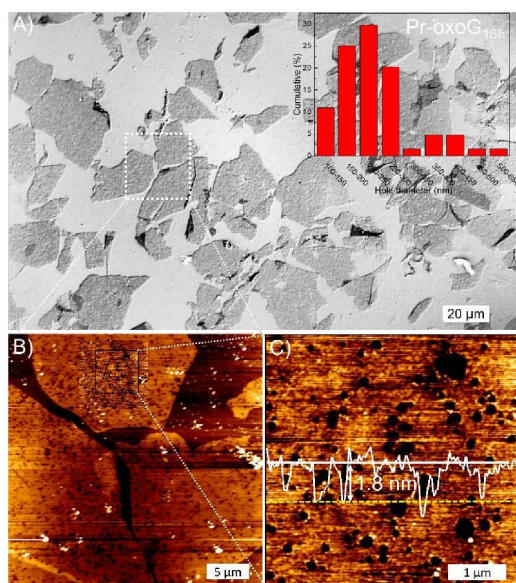


Figure S5. A) Optical microscope image of flakes of Pr-oxoG_{16h} on Si/300 nm SiO₂ substrate; B) AFM topography image of Pr-oxoG_{16h}. C) AFM image showing pores. The yellow line represents the height profile of Pr-oxoG_{16h}.

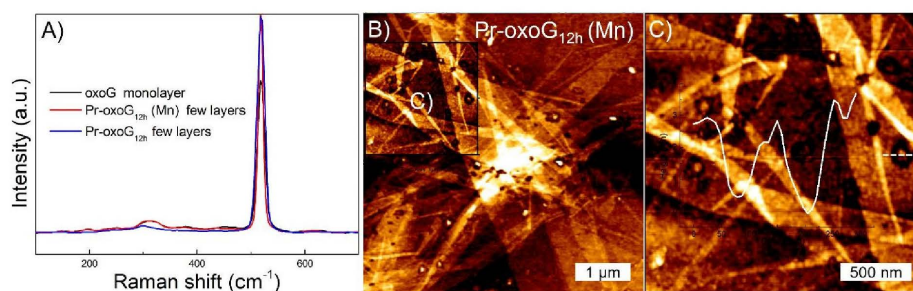
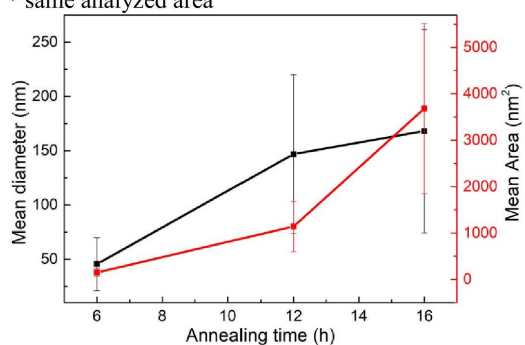


Figure S6. A) Raman spectrum of monolayer oxoG, few-layer Pr-oxoG_{12h} (Mn) and few-layer Pr-oxoG_{12h} on Si/300 nm SiO₂ substrate; B, C) AFM topography image of few-layer Pr-oxoG_{12h} (Mn). The white line represents the height profile of few-layer Pr-oxoG_{12h} (Mn).

Table S2. Number total of pores, mean (average), standard deviation, minimum, Median and maximum of diameter of pores.

	Number total	Mean (diameter)	Standard Deviation	Sum	Minimum	Median	Maximum
Pr-oxoG _{6h}	126	45.45256	24.35966	5727.022	9.298	37.749	127.104
Pr-oxoG _{12h}	181	146.74168	73.25105	26560.244	37.771	133.539	503.704
Pr-oxoG _{16h}	104	167.95725	93.74814	17635.511	40.323	153.438	620.968
Pr-oxoG _{12h} (Mn)*	101	128.59717	74.66974	12988.314	26.845	108.216	457.154
Pr-oxoG _{12h} *	101	146.98062	72.06714	14845.043	48.65	138.462	523.981
	Number total	Mean (Area)	Standard Deviation	Sum	Minimum	Median	Maximum
Pr-oxoG _{6h}	126	149.94286	75.35488	18892.8	38.42	124.863	403.405
Pr-oxoG _{12h}	181	1138.8772	542.72571	206136.774	329.218	1042.524	3786.008
Pr-oxoG _{16h}	105	3680.27461	1830.97899	386428.834	1144.409	3433.228	12588.501
Pr-oxoG _{12h} (Mn)*	101	1903.31623	1003.89167	192234.939	540.492	1621.476	6305.738
Pr-oxoG _{12h} *	101	2502.78283	1099.68609	252781.066	1183.432	2366.864	8284.024

* same analyzed area

**Figure S7.** A comparison between the different mean diameters and mean pores areas after different annealing time.

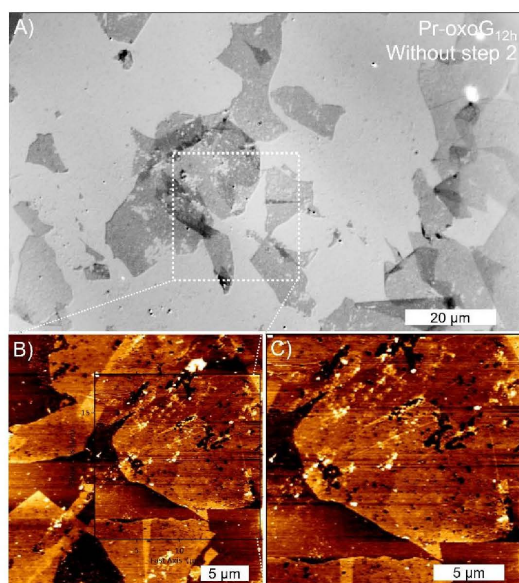


Figure S8. A) Optical microscope image of flakes of Pr-oxoG_{12h} on Si/SiO₂ substrate without water washing step 2; B) AFM topography image of flakes of Pr-oxoG_{12h} on Si/SiO₂ substrate without water washing step 2.

Table S3. Quantitative analysis of the high resolution XP C 1s and O 1s spectra presented in Figure 3A and B of the main text including peak assignment, binding energies and areas obtained from the spectra deconvolution.

sample	Peak assignment	Binding energy, eV	Area, %	
oxoG	C-C /C-H	284.6	47.8	
	C-O/C-OH/C=O	286.6	46.3	
	C=O/COOH	288.1	5.9	
	O 1s	C=O	531.2	31.1
	O 1s	C-O/SiO ₂ /O-C=O	532.4	67.2
Pr-oxoG _{12h}	-OH/Na KLL	535.4	1.7	
	C-C sp ²	284.5	50.8	
	C-C sp ³ / C-S/C-N	285.2	34.6	
	C-O/C-OH	286.5	4.5	
	C=O	287.9	7.0	
	COOH	289.9	3.1	
	O 1s	C=O	531.3	28.0
	O 1s	C-O/SiO ₂ /O-C=O	532.7	65.4
	O 1s	-OH/Na KLL	535.8	6.6

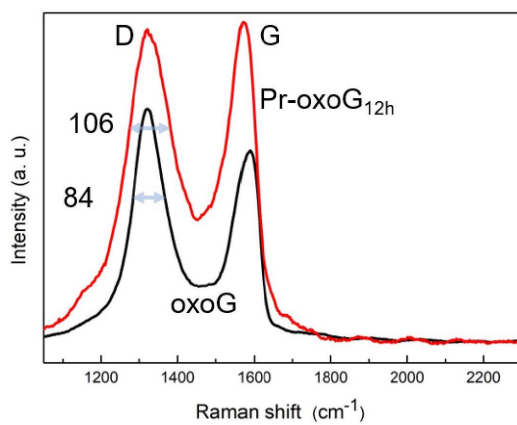


Figure S9. Raman spectrum of oxoG, and Pr-oxoG_{12h}. Numbers indicate the full-width at half-maximum of the D band.

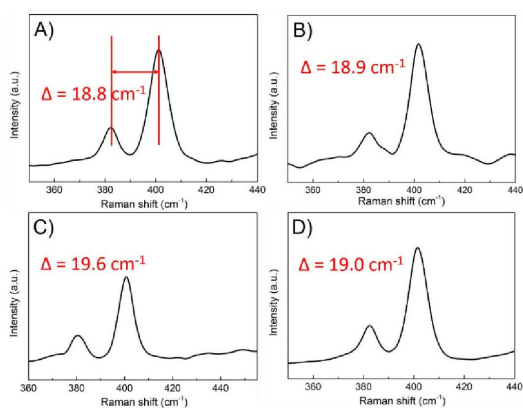


Figure S10. Raman spectrum of monolayer MoS₂ for A) MoS₂ on SiO₂, B) Pr-oxoG_{6h}/MoS₂, C) Pr-oxoG_{12h}/MoS₂ and D) Pr-oxoG_{12h}/MoS₂ (Mn) heterostructure.

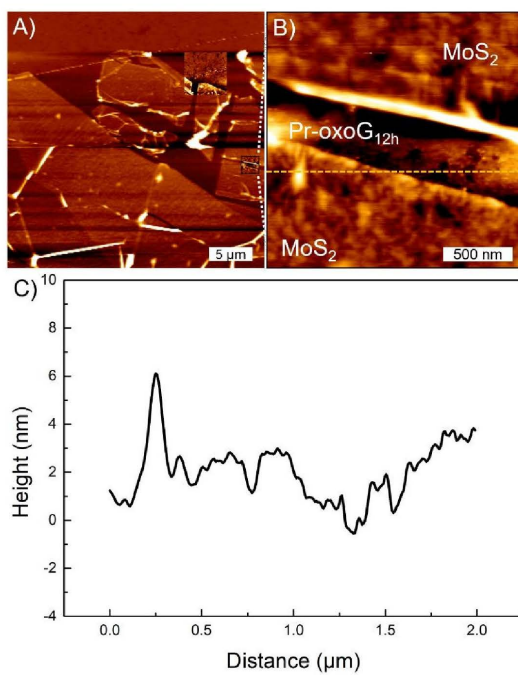


Figure S11. A and B) AFM topography images of monolayer Pr-oxoG_{12h}/MoS₂ heterostructure. C) The white line represents the height of Pr-oxoG_{12h}/MoS₂ heterostructure. MoS₂ and Pr-oxoG_{12h} almost have same thickness.

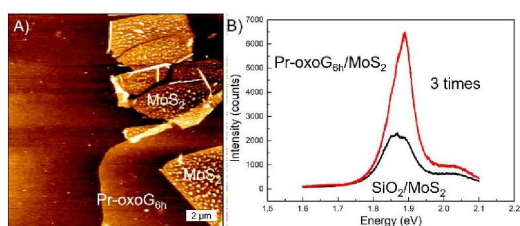


Figure S12. A) AFM topography images of monolayer Pr-oxoG_{6h}/MoS₂ heterostructure; B) PL spectra of monolayer MoS₂ on SiO₂ (black) and monolayer Pr-oxoG_{6h}/MoS₂ heterostructure (red), respectively.

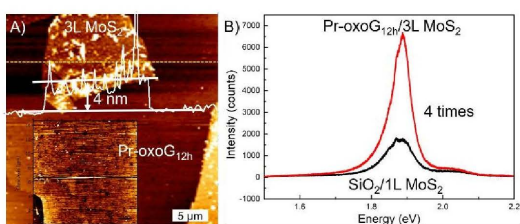


Figure S13. A) AFM topography images of trilayer Pr-oxoG_{12h}/MoS₂ heterostructure. The height of 3L MoS₂ is almost 4 nm. B) PL spectra of monolayer MoS₂ on SiO₂ and trilayer Pr-oxoG_{12h}/MoS₂ heterostructure.

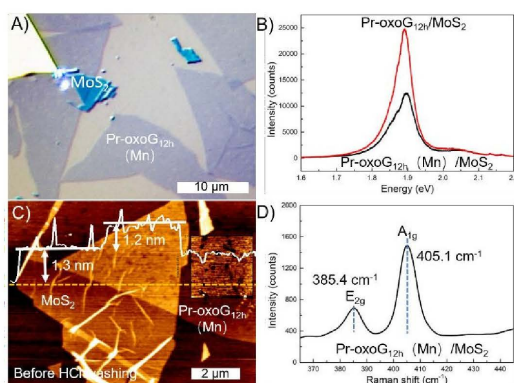


Figure S14. A) Optical microscope image of a monolayer Pr-oxoG_{12h}(Mn)/MoS₂ heterostructure; B) PL spectra of a monolayer Pr-oxoG_{12h}(Mn)/MoS₂ heterostructure and a monolayer Pr-oxoG_{12h}(Mn)/MoS₂ heterostructure. C) AFM topography image of Pr-oxoG_{12h}(Mn)/MoS₂ heterostructure. The white line represents the height profile along yellow line. D) Raman spectra of Pr-oxoG_{12h}(Mn)/MoS₂.

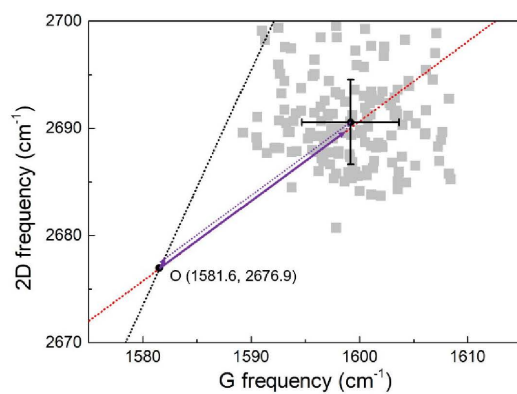


Figure S15. The grey dots were obtained from Raman mapping of Pr-oxoG_{12h}. The black dot (1581.6, 2676.9 cm⁻¹) stems from reference [15] and the position relates to graphene, which is not affected by charge or strain doping. The red dashed line represent doped graphene with varying density of holes with a slope is 0.75. The black dashed line represents charge-neutral graphene under randomly oriented uniaxial stress with a slope of 2.20. The purple solid line is the effects corresponding to the hole doping and strain decomposed by the vector model.

References

- [1] S. Eigler, M. Enzelberger-Heim, S. Grimm, P. Hofmann, W. Kroener, A. Geworski, C. Dotzer, M. Rockert, J. Xiao, C. Papp, O. Lytken, H. P. Steinruck, P. Müller, A. Hirsch, *Adv. Mater.* **2013**, *25*, 3583.
- [2] F. Grote, C. Gruber, F. Börrnert, U. Kaiser, S. Eigler, *Angew. Chem. Int. Ed.* **2017**, *56*, 9222.
- [3] S. C. O'Hern, M. S. Boutilier, J. C. Idrobo, Y. Song, J. Kong, T. Laoui, M. Atieh, R. Karnik, *Nano Lett.* **2014**, *14*, 1234.
- [4] G. He, S. Huang, L. F. Villalobos, J. Zhao, M. Mensi, E. Oveisi, M. Rezaei, K. V. Agrawal, *Energy Environ. Sci.* **2019**, *12*, 3305.
- [5] S. Standop, O. Lehtinen, C. Herbig, G. Lewes-Malandrakis, F. Craes, J. Kotakoski, T. Michely, A. V. Krasheninnikov, C. Busse, *Nano Lett.* **2013**, *13*, 1948.
- [6] C. Neumann, D. Kaiser, M. J. Mohn, M. Füsler, N.-E. Weber, O. Reimer, A. Götzhäuser, T. Weimann, A. Terfort, U. Kaiser, A. Turchanin, *ACS Nano* **2019**, *13*, 7310.
- [7] Z. Fan, Q. Zhao, T. Li, J. Yan, Y. Ren, J. Feng, T. Wei, *Carbon* **2012**, *50*, 1699.
- [8] X. Wang, L. Jiao, K. Sheng, C. Li, L. Dai, G. Shi, *Sci. Rep.* **2013**, *3*, 1996.
- [9] Y. Xu, C.-Y. Chen, Z. Zhao, Z. Lin, C. Lee, X. Xu, C. Wang, Y. Huang, M. I. Shakir, X. Duan, *Nano Lett.* **2015**, *15*, 4605.
- [10] H. Zhang, W. Liu, Z. Zhang, M. Li, B. Xu, J. Guo, *Phys. Chem. Chem. Phys.* **2018**, *20*, 26814.
- [11] X. Liao, B. Zhang, T. Furutani, Y. Chen, H. Xiao, Y. Ni, A. Yonezu, X. Chen, *Small* **2019**, *15*, e1903213.
- [12] T. Palaniselvam, H. B. Aiyappa, S. Kurungot, *J. Mater. Chem.* **2012**, *22*, 23799.
- [13] D. Zhou, Y. Cui, P. W. Xiao, M. Y. Jiang, B. H. Han, *Nat. Commun.* **2014**, *5*, 4716.
- [14] Z. Wang, Q. Yao, C. Neumann, F. Börrnert, J. Renner, U. Kaiser, A. Turchanin, H. J. W. Zandvliet, S. Eigler, *Angew. Chem. Int. Ed.* **2020**, *59*, 13657.
- [15] J. E. Lee, G. Ahn, J. Shim, Y. S. Lee, S. Ryu, *Nat. Commun.* **2012**, *3*, 1024.

6.3 Interlayer Electron Modulation in van der Waals Heterostructures Assembled by Stacking Monolayer MoS₂ onto Monolayer Graphene with Different Electron Transfer Ability

Authors	Z. Wang, Q. Cao, K. Sotthewes, Y. Hu, H. S. Shin, S. Eigler
Journal	<i>Nanoscale</i> 2021 , 13, 15464-15470
DOI	10.1039/D1NR03708K
Links	http://dx.doi.org/10.1039/D1NR03708K https://pubs.rsc.org/en/content/articlelanding/2021/nr/d1nr03708k
	The concept of this manuscript was elaborated by Z. Wang and Prof. Dr. S. Eigler.
Detailed scientific contribution	Some heterostructures were prepared by Y. Hu, and some photoluminescence and Raman measurements were done by Y. Hu. The revision of the manuscript was assisted by Y. Hu.
Estimated own contribution	~15 %

List of Abbreviations

1-PrOH	1-propanol
Abs	absorption
ACN	acetonitrile
AFM	atomic force microscopy
<i>a.u.</i>	arbitrary units
CNTs	carbon nanotubes
CT	charge transfer
CVD	chemical vapour deposition
DCM	dichloromethane
D_{eff}	effective diameter
DIW	double distilled water
DMF	N,N-Dimethylformamide
DMSO	dimethyl sulfoxide
EA	elemental analysis
EDX	energy-dispersive X-ray spectroscopy
E_{m}	emission
EtOH	ethanol
Ex	excitation
eV	electron volt
FL	fluorescence
FL_{em}	fluorescence emission
FL_{ex}	fluorescence excitation
FT-IR	fourier-transformed infrared spectroscopy
FWHM	full width at half maximum

Γ	full width at half maximum
GO	graphene oxide
GQDs	graphene quantum dots
HAADF-STEM	high-angle annular dark-field scanning electron microscopy
HB-ICT	hydrogen bonding stabilized intramolecular charge transfer
HR-TEM	high-resolution transmission electron microscopy
ICT	intramolecular charge transfer
I_D/I_G	intensity ratio of the D and G mode
IR	infrared spectroscopy
k_f	radiative rate constant
k_{nr}	non-radiative rate constant
LB	Langmuir-Blodgett
LE	locally excited
MAS	magic angle spinning
MeOH	methanol
MWCO	molecular weight cutoff
NMR	nuclear magnetic resonance
ns	nanosecond
oxo-G	oxo-functionalized graphene
PhMe	toluene
pK_a	acid dissociation constant
p-oxo-G	porous oxo-functionalized graphene
ps	picosecond

QY	fluorescence quantum yield
r-oxo-G	reduced oxo-functionalized graphene
R _{RMS}	root mean square roughness
SALVE	sub-angstrom low-voltage electron microscope
SRS	statistical Raman spectroscopy
ssNMR	solid-state nuclear magnetic resonance
TCM	chloroform
TEM	transmission electron microscopy
THF	tetrahydrofuran
UV	ultraviolet
UV/Vis	ultraviolet-visible
XPS	X-ray photoelectron spectroscopy
Δf	orientation polarizability
Δ_{St}	Stokes shifts
τ	fluorescence lifetime

List of Publications

1. **Y. Hu**, Q. Cao, C. Neumann, T. Lehnert, F. Börrnert, Y. Wang, U. Kaiser, A. Turchanin, S. Eigler;
Wet-chemical synthesis of solution-processible porous graphene *via* defect-driven etching.
Carbon **2021**, *185*, 568-577.
2. **Y. Hu**, C. Neumann, L. Scholtz, A. Turchanin, U. Kaiser, A. Resch-Genger, S. Eigler;
Polarity, intramolecular charge transfer, and hydrogen bond co-mediated solvent effects on the optical properties of graphene quantum dots.
Nano Res. **2022**, accepted.
3. Z. Wang, Q. Yao, **Y. Hu**, C. Li, M. Hußmann, B. Weintrub, J. N. Kirchhof, K. Bolotin, T. Taniguchi, K. Watanabe, S. Eigler;
Influence of SiO₂ or h-BN substrate on the roomtemperature electronic transport in chemically derived single layer graphene.
RSC Adv. **2019**, *9*, 38011-38016.
4. Y. Wang, C. Neumann, M. Hußmann, Q. Cao, **Y. Hu**, O. Garrity, P. Kusch, A. Turchanin, S. Eigler;
Synthesis of Wet-Chemically Prepared Porous-Graphene Single Layers on Si/SiO₂ Substrate Increasing the Photoluminescence of MoS₂ in Heterostructures.
Adv. Mater. Interfaces **2021**, *8*, 2100783.
5. Z. Wang, Q. Cao, K. Sotthewes, **Y. Hu**, H. S. Shin, S. Eigler;
Interlayer electron modulation in van der Waals heterostructures assembled by stacking monolayer MoS₂ onto monolayer graphene with different electron transfer ability.
Nanoscale **2021**, *13*, 15464-15470.

References

- [1] V. Georgakilas, J. A. Perman, J. Tucek, R. Zboril, *Chem. Rev.* **2015**, *115*, 4744-4822.
- [2] E. Fitzer, K.-H. Kochling, H. Boehm, H. Marsh, *Pure Appl. Chem.* **1995**, *67*, 473-506.
- [3] D. R. Lenski, M. S. Fuhrer, *J. Appl. Phys.* **2011**, *110*, 013720.
- [4] S. Tkachev, E. Y. Buslaeva, A. Naumkin, S. Kotova, I. Laure, S. Gubin, *Inorg. Mater.* **2012**, *48*, 796-802.
- [5] P. Feicht, S. Eigler, *ChemNanoMat* **2018**, *4*, 244-252.
- [6] a) K. S. Novoselov, A. K. Geim, S. V. Morozov, D. Jiang, Y. Zhang, S. V. Dubonos, I. V. Grigorieva, A. A. Firsov, *Science* **2004**, *306*, 666-669; b) C. N. R. Rao, K. Biswas, K. S. Subrahmanyam, A. Govindaraj, *J. Mater. Chem.* **2009**, *19*, 2457-2469; c) X. Li, J. Yu, S. Wageh, A. A. Al-Ghamdi, J. Xie, *Small* **2016**, *12*, 6640-6696; d) V. Chabot, D. Higgins, A. Yu, X. Xiao, Z. Chen, J. Zhang, *Energy Environ. Sci.* **2014**, *7*, 1564-1596.
- [7] a) K. Khan, A. K. Tareen, M. Aslam, R. Wang, Y. Zhang, A. Mahmood, Z. Ouyang, H. Zhang, Z. Guo, *J. Mater. Chem. C* **2020**, *8*, 387-440; b) N. Rohaizad, C. C. Mayorga-Martinez, M. Fojtů, N. M. Latiff, M. Pumera, *Chem. Soc. Rev.* **2021**, *50*, 619-657.
- [8] C. Schafhaeutl, *J. Prakt. Chem.* **1840**, *21*, 129-157.
- [9] C. Schafhaeutl, *Lond. Edinb. Dubl. Phil. Mag.* **1840**, *16*, 570-590.
- [10] a) B. Brodie, *Ann. Chim. Phys* **1855**, *45*, 351-353; b) B. C. Brodie, *Phil. Trans. R. Soc. London* **1859**, *149*, 249-259.
- [11] F. Gottschalk, *J. Prakt. Chem.* **1865**, *95*, 321-350.
- [12] L. Staudenmaier, *Chem. Ber.* **1898**, *31*, 1481-1487.
- [13] a) U. Hofmann, *Ber. Dtsch. Chem. Ges.* **1928**, *61*, 435-441; b) U. Hofmann, A. Frenzel, *Ber. Dtsch. Chem. Ges.* **1930**, *63*, 1248-1262.
- [14] W. S. Hummers, R. E. Offeman, *J. Am. Chem. Soc.* **1958**, *80*, 1339-1339.
- [15] H. P. Boehm., A. Clauss, G. O. Fischer, U. Hofmann, *Z. Naturforsch. B* **1962**, *17*, 150-153.
- [16] H. P. Boehm, R. Setton, E. Stumpp, *Carbon* **1986**, *24*, 241-245.
- [17] M. D. Fischbein, M. Drndić, *Appl. Phys. Lett.* **2008**, *93*, 113107.
- [18] L. A. Ponomarenko, F. Schedin, M. I. Katsnelson, R. Yang, E. W. Hill, K. S. Novoselov, A. K. Geim, *Science* **2008**, *320*, 356-358.
- [19] S. Eigler, M. Enzelberger-Heim, S. Grimm, P. Hofmann, W. Kroener, A. Geworski, C. Dotzer, M. Röckert, J. Xiao, C. Papp, O. Lytken, H.-P. Steinrück, P. Müller, A. Hirsch, *Adv. Mater.* **2013**, *25*, 3583-3587.

- [20] a) P. Xu, J. Yang, K. Wang, Z. Zhou, P. Shen, *Sci. Bull.* **2012**, *57*, 2948-2955; b) L. Jiang, Z. Fan, *Nanoscale* **2014**, *6*, 1922-1945; c) A. C. Lokhande, I. A. Qattan, C. D. Lokhande, S. P. Patole, *J. Mater. Chem. A* **2020**, *8*, 918-977.
- [21] S. Han, D. Wu, S. Li, F. Zhang, X. Feng, *Adv. Mater.* **2014**, *26*, 849-864.
- [22] Z. Han, Z. Tang, P. Li, G. Yang, Q. Zheng, J. Yang, *Nanoscale* **2013**, *5*, 5462-5467.
- [23] L. Lu, J. T. M. De Hosson, Y. Pei, *Carbon* **2019**, *144*, 713-723.
- [24] R. He, S. Cong, J. Wang, J. Liu, Y. Zhang, *ACS Appl. Mater. Interfaces* **2019**, *11*, 4338-4344.
- [25] D.-e. Jiang, V. R. Cooper, S. Dai, *Nano Lett.* **2009**, *9*, 4019-4024.
- [26] D. Zhou, Y. Cui, P.-W. Xiao, M.-Y. Jiang, B.-H. Han, *Nat. Commun.* **2014**, *5*, 4716.
- [27] X. Wang, L. Jiao, K. Sheng, C. Li, L. Dai, G. Shi, *Sci. Rep.* **2013**, *3*, 1996.
- [28] Y. Lin, K. A. Watson, J.-W. Kim, D. W. Baggett, D. C. Working, J. W. Connell, *Nanoscale* **2013**, *5*, 7814-7824.
- [29] a) S. Licht, *J. Phys. Chem. B* **2001**, *105*, 6281-6294; b) Y. Cao, J. W. Pomeroy, M. J. Uren, F. Yang, M. Kuball, *Nat. Electron.* **2021**, *4*, 478-485.
- [30] S. P. Singh, Y. Li, J. Zhang, J. M. Tour, C. J. Arnusch, *ACS Nano* **2018**, *12*, 289-297.
- [31] A. Du, Z. Zhu, S. C. Smith, *J. Am. Chem. Soc.* **2010**, *132*, 2876-2877.
- [32] M. De La Pierre, P. Karamanis, J. Baima, R. Orlando, C. Pouchan, R. Dovesi, *J. Phys. Chem. C* **2013**, *117*, 2222-2229.
- [33] J. Zhang, H. Song, D. Zeng, H. Wang, Z. Qin, K. Xu, A. Pang, C. Xie, *Sci. Rep.* **2016**, *6*, 32310.
- [34] Y. Ito, Y. Tanabe, K. Sugawara, M. Koshino, T. Takahashi, K. Tanigaki, H. Aoki, M. Chen, *Phys. Chem. Chem. Phys.* **2018**, *20*, 6024-6033.
- [35] M. Huth, F. Porrati, O. V. Dobrovolskiy, *Microelectron. Eng.* **2018**, *185-186*, 9-28.
- [36] F. Grote, C. Gruber, F. Börrnert, U. Kaiser, S. Eigler, *Angew. Chem. Int. Ed.* **2017**, *56*, 9222-9225.
- [37] C. H. Yang, P. L. Huang, X. F. Luo, C. H. Wang, C. Li, Y. H. Wu, J. K. Chang, *ChemSusChem* **2015**, *8*, 1779-1786.
- [38] D. Xu, S. Yang, P. Chen, Q. Yu, X. Xiong, J. Wang, *Carbon* **2019**, *146*, 301-312.
- [39] C. Neumann, D. Kaiser, M. J. Mohn, M. Fuser, N.-E. Weber, O. Reimer, A. Götzhäuser, T. Weimann, A. Terfort, U. Kaiser, A. Turchanin, *ACS Nano* **2019**, *13*, 7310-7322.
- [40] T. Hirano, K. Nakade, S. Li, K. Kawai, K. Arima, *Carbon* **2018**, *127*, 681-687.
- [41] Z. Fan, Z. Cheng, J. Feng, Z. Xie, Y. Liu, Y. Wang, *J. Mater. Chem. A* **2017**, *5*, 16689-16701.
- [42] a) J. Shen, Y. Zhu, X. Yang, C. Li, *Chem. Commun.* **2012**, *48*, 3686-3699; b) P. Tian, L. Tang, K. S. Teng, S. P. Lau, *Mater. Today Chem.* **2018**, *10*, 221-258; c) Y. Yan, J.

- Gong, J. Chen, Z. Zeng, W. Huang, K. Pu, J. Liu, P. Chen, *Adv. Mater.* **2019**, *31*, 1808283; d) S. Chung, R. A. Revia, M. Zhang, *Adv. Mater.* **2021**, *33*, 1904362.
- [43] a) J. Zhao, L. Tang, J. Xiang, R. Ji, J. Yuan, J. Zhao, R. Yu, Y. Tai, L. Song, *Appl. Phys. Lett.* **2014**, *105*, 111116; b) M. T. Hasan, R. Gonzalez-Rodriguez, C. Ryan, K. Pota, K. Green, J. L. Coffey, A. V. Naumov, *Nano Res.* **2019**, *12*, 1041-1047.
- [44] L. Li, G. Wu, G. Yang, J. Peng, J. Zhao, J.-J. Zhu, *Nanoscale* **2013**, *5*, 4015-4039.
- [45] a) S. Zhu, J. Zhang, S. Tang, C. Qiao, L. Wang, H. Wang, X. Liu, B. Li, Y. Li, W. Yu, X. Wang, H. Sun, B. Yang, *Adv. Func. Mater.* **2012**, *22*, 4732-4740; b) Y. Zhu, G. Wang, H. Jiang, L. Chen, X. Zhang, *Chem. Commun.* **2015**, *51*, 948-951; c) Q. Xin, X. Jia, A. Nawaz, W. Xie, L. Li, J. R. Gong, *Nano Res.* **2020**, *13*, 1427-1433; d) D. Kurniawan, B. A. Anjali, O. Setiawan, K. K. Ostrikov, Y. G. Chung, W.-H. Chiang, *ACS Appl. Mater. Interfaces* **2022**, *14*, 1670-1683.
- [46] X. T. Zheng, A. Ananthanarayanan, K. Q. Luo, P. Chen, *Small* **2015**, *11*, 1620-1636.
- [47] a) I. Hagymási, P. Vancsó, A. Pálinkás, Z. Osváth, *Phys. Rev. B* **2017**, *95*, 075123; b) A. V. Vorontsov, E. V. Tretyakov, *Phys. Chem. Chem. Phys.* **2018**, *20*, 14740-14752.
- [48] J. Deng, Q. Lu, H. Li, Y. Zhang, S. Yao, *RSC Adv.* **2015**, *5*, 29704-29707.
- [49] Z. Zhang, J. Zhang, N. Chen, L. Qu, *Energy Environ. Sci.* **2012**, *5*, 8869-8890.
- [50] R. Sekiya, Y. Uemura, H. Murakami, T. Haino, *Angew. Chem. Int. Ed.* **2014**, *53*, 5619-5623.
- [51] a) S. Zhu, L. Wang, B. Li, Y. Song, X. Zhao, G. Zhang, S. Zhang, S. Lu, J. Zhang, H. Wang, H. Sun, B. Yang, *Carbon* **2014**, *77*, 462-472; b) P. Yang, L. Zhou, S. Zhang, N. Wan, W. Pan, W. Shen, *J. Appl. Phys.* **2014**, *116*, 244306; c) S. Zhu, Y. Song, J. Wang, H. Wan, Y. Zhang, Y. Ning, B. Yang, *Nano Today* **2017**, *13*, 10-14.
- [52] Y. Niko, S. Kawauchi, G.-i. Konishi, *Chem. Eur. J.* **2013**, *19*, 9760-9765.
- [53] E. Buncel, S. Rajagopal, *Acc. Chem. Res.* **1990**, *23*, 226-231.
- [54] A. S. Klymchenko, *Acc. Chem. Res.* **2017**, *50*, 366-375.
- [55] S. Zhu, J. Zhang, C. Qiao, S. Tang, Y. Li, W. Yuan, B. Li, L. Tian, F. Liu, R. Hu, H. Gao, H. Wei, H. Zhang, H. Sun, B. Yang, *Chem. Commun.* **2011**, *47*, 6858-6860.
- [56] X. Niu, Y. Li, H. Shu, J. Wang, *Nanoscale* **2016**, *8*, 19376-19382.
- [57] A. Guirguis, J. W. Maina, X. Zhang, L. C. Henderson, L. Kong, H. Shon, L. F. Dumée, *Mater. Horiz.* **2020**, *7*, 1218-1245.
- [58] a) X. Zhang, H. Zhang, C. Li, K. Wang, X. Sun, Y. Ma, *RSC Adv.* **2014**, *4*, 45862-45884; b) W. Hooch Antink, Y. Choi, K.-d. Seong, J. M. Kim, Y. Piao, *Adv. Mater. Interfaces* **2018**, *5*, 1701212.
- [59] a) D. Pan, J. Zhang, Z. Li, M. Wu, *Adv. Mater.* **2010**, *22*, 734-738; b) Y. Li, Y. Zhao, H. Cheng, Y. Hu, G. Shi, L. Dai, L. Qu, *J. Am. Chem. Soc.* **2012**, *134*, 15-18.

- [60] P.-C. Lin, S. Lin, P. C. Wang, R. Sridhar, *Biotechnol. Adv.* **2014**, *32*, 711-726.
- [61] M. M. Modena, B. Rühle, T. P. Burg, S. Wuttke, *Adv. Mater.* **2019**, *31*, 1901556.
- [62] S. Watcharotone, D. A. Dikin, S. Stankovich, R. Piner, I. Jung, G. H. B. Dommett, G. Evmenenko, S.-E. Wu, S.-F. Chen, C.-P. Liu, S. T. Nguyen, R. S. Ruoff, *Nano Lett.* **2007**, *7*, 1888-1892.
- [63] O. Guillaume-Gentil, E. Potthoff, D. Ossola, C. M. Franz, T. Zambelli, J. A. Vorholt, *Trends Biotechnol.* **2014**, *32*, 381-388.
- [64] F. Lu, M. A. Belkin, *Opt. Express* **2011**, *19*, 19942-19947.
- [65] N. Jalili, K. Laxminarayana, *Mechatronics* **2004**, *14*, 907-945.
- [66] A. Rizvi, J. T. Mulvey, B. P. Carpenter, R. Talosig, J. P. Patterson, *Chem. Rev.* **2021**, *121*, 14232-14280.
- [67] C. J. Edgcombe, *Ultramicroscopy* **2017**, *182*, 124-130.
- [68] W. Q. Chen, A. Veksha, G. Lisak, *Carbon* **2020**, *159*, 378-389.
- [69] L. M. Ng, R. Simmons, *Anal. Chem.* **1999**, *71*, 343-350.
- [70] M. L. McKelvy, T. R. Britt, B. L. Davis, J. K. Gillie, L. A. Lentz, A. Leugers, R. A. Nyquist, C. L. Putzig, *Anal. Chem.* **1996**, *68*, 93-160.
- [71] E. Mendes, N. Duarte, *Foods* **2021**, *10*, 477.
- [72] F. R. van de Voort, *Food Res. Int.* **1992**, *25*, 397-403.
- [73] a) S. Eigler, C. Dotzer, A. Hirsch, M. Enzelberger, P. Müller, *Chem. Mater.* **2012**, *24*, 1276-1282; b) S. Eigler, S. Grimm, F. Hof, A. Hirsch, *J. Mater. Chem. A* **2013**, *1*, 11559-11562.
- [74] a) S. Bae, H. Kim, Y. Lee, X. Xu, J.-S. Park, Y. Zheng, J. Balakrishnan, T. Lei, H. Ri Kim, Y. I. Song, Y.-J. Kim, K. S. Kim, B. Özyilmaz, J.-H. Ahn, B. H. Hong, S. Iijima, *Nat. Nanotechnol.* **2010**, *5*, 574-578; b) L. M. Malard, M. A. Pimenta, G. Dresselhaus, M. S. Dresselhaus, *Phys. Rep.* **2009**, *473*, 51-87.
- [75] C. Casiraghi, A. Hartschuh, E. Lidorikis, H. Qian, H. Harutyunyan, T. Gokus, K. S. Novoselov, A. C. Ferrari, *Nano Lett.* **2007**, *7*, 2711-2717.
- [76] C. V. Raman, K. S. Krishnan, *Nature* **1928**, *121*, 501-502.
- [77] Y. C. Cho, S. I. Ahn, *Sci. Rep.* **2020**, *10*, 11692.
- [78] A. C. Ferrari, D. M. Basko, *Nat. Nanotechnol.* **2013**, *8*, 235-246.
- [79] a) M. M. Lucchese, F. Stavale, E. H. M. Ferreira, C. Vilani, M. V. O. Moutinho, R. B. Capaz, C. A. Achete, A. Jorio, *Carbon* **2010**, *48*, 1592-1597; b) L. G. Cançado, A. Jorio, E. H. M. Ferreira, F. Stavale, C. A. Achete, R. B. Capaz, M. V. O. Moutinho, A. Lombardo, T. S. Kulmala, A. C. Ferrari, *Nano Lett.* **2011**, *11*, 3190-3196.
- [80] J. M. Hollander, W. L. Jolly, *Acc. Chem. Res.* **1970**, *3*, 193-200.
- [81] C. S. Fadley, *J. Electron Spectrosc. Relat. Phenom.* **2010**, *178-179*, 2-32.
- [82] F. T. Johra, J.-W. Lee, W.-G. Jung, *J. Ind. Eng. Chem.* **2014**, *20*, 2883-2887.

- [83] J. H. F. Bothwell, J. L. Griffin, *Biol. Rev.* **2011**, *86*, 493-510.
- [84] M. Renault, A. Cukkemane, M. Baldus, *Angew. Chem. Int. Ed.* **2010**, *49*, 8346-8357.
- [85] S. Parthasarathy, Y. Nishiyama, Y. Ishii, *Acc. Chem. Res.* **2013**, *46*, 2127-2135.
- [86] W. Gao, L. B. Alemany, L. Ci, P. M. Ajayan, *Nature Chem.* **2009**, *1*, 403-408.
- [87] V. P. Fadeeva, V. D. Tikhova, O. N. Nikulicheva, *J. Anal. Chem.* **2008**, *63*, 1094-1106.
- [88] Q. Lai, S. Zhu, X. Luo, M. Zou, S. Huang, *AIP Adv.* **2012**, *2*, 032146.
- [89] W. Măntele, E. Deniz, *Spectrochim. Acta A* **2017**, *173*, 965-968.
- [90] S. Saxena, T. A. Tyson, S. Shukla, E. Negusse, H. Chen, J. Bai, *Appl. Phys. Lett.* **2011**, *99*, 013104.
- [91] N. Siraj, B. El-Zahab, S. Hamdan, T. E. Karam, L. H. Haber, M. Li, S. O. Fakayode, S. Das, B. Valle, R. M. Strongin, G. Patonay, H. O. Sintim, G. A. Baker, A. Powe, M. Lowry, J. O. Karolin, C. D. Geddes, I. M. Warner, *Anal. Chem.* **2016**, *88*, 170-202.
- [92] M. Y. Berezin, S. Achilefu, *Chem. Rev.* **2010**, *110*, 2641-2684.
- [93] X.-F. Zhang, J. Zhang, L. Liu, *J. Fluoresc.* **2014**, *24*, 819-826.
- [94] O. N. Oliveira, L. Caseli, K. Ariga, *Chem. Rev.* **2022**, *122*, 6459-6513.
- [95] J. A. Zasadzinski, R. Viswanathan, L. Madsen, J. Garnaes, D. K. Schwartz, *Science* **1994**, *263*, 1726-1733.

Acknowledgements

Here, I would like to thank my supervisor, Prof. Dr. Siegfried Eigler, for allowing me to study as a Ph.D. student in his group. Throughout my Ph.D., he provided an open and free platform for me to conduct my research happily. Whenever I encountered problems with my experiments, he was always available to provide constructive suggestions. In addition, he helped me a lot in writing, revising, and publishing my manuscripts.

Thanks to all my colleagues in AG Eigler for their help in my studies and life, especially Qing, Christian, Chenbo, Zhenping, Zhuting, Yiqing, Lucia, and Fabian. They taught me a lot of life and experimental knowledge and enriched my entire doctoral career.

I want to thank Dr. Ute Resch-Genger from the Federal Institute for Materials Research and Testing, Prof. Dr. Andrey Turchanin from Friedrich Schiller University Jena, and Prof. Dr. Ute Kaiser from Ulm University for their help in the characterization and analysis of graphene-related materials. I learned a lot from their groups.

I want to thank the China Scholarship Council (CSC) for providing me with financial support to cover my whole Ph.D. period.

Finally, I would like to thank my family and girlfriend for their understanding, support, and love during my Ph.D. study abroad.

Statement of the author

I declare on the affidavit that I have written the dissertation independently and have used no sources other than those I have indicated and that there are no facts which make me unworthy of the conduct of a doctoral degree under the provisions of the law governing academic degrees. Further I declare my consent that the electronic version of my dissertation, while maintaining my copyrights and data protection, may be subjected to a separate review regarding the independent preparation of the dissertation. I have not submitted the dissertation anywhere else to obtain an academic degree and have not already passed this or a similar doctoral exam without success.

Berlin, 01.08.2022

Yalei Hu